

YEAR END TECHNICAL REPORT

August 29, 2015 to August 28, 2016

Chemical Process Alternatives for Radioactive Waste

Date submitted:

October 21, 2016

Principal Investigator:

Leonel E. Lagos, Ph.D., PMP®

Florida International University Collaborators:

Dwayne McDaniel, Ph.D., P.E. (Project Manager)

Amer Awwad, M.S., P.E.

Seckin Gokaltun, Ph.D.

David Roelant, Ph.D.

Anthony Abrahao, M.S.

Hadi Ferkmanidi, Ph.D.

Aparna Aravelli

DOE Fellows

Prepared for:

U.S. Department of Energy

Office of Environmental Management

Under Cooperative Agreement DE-EM00000598



Applied Research Center

FLORIDA INTERNATIONAL UNIVERSITY

This document represents one (1) of four (4) reports that comprise the Year End Reports for the period of August 29, 2015 to August 28, 2016 prepared by the Applied Research Center at Florida International University for the U.S. Department of Energy Office of Environmental Management (DOE-EM) under Cooperative Agreement No. DE-EM0000598.

The complete set of FIU's Year End Reports for this reporting period includes the following documents:

Project 1: Chemical Process Alternatives for Radioactive Waste
Document number: FIU-ARC-2016-800006470-04b-249

Project 2: Environmental Remediation Science and Technology
Document number: FIU-ARC-2016-800006471-04b-250

Project 3: Waste and D&D Engineering and Technology Development
Document number: FIU-ARC-2016-800006472-04b-238

Project 4: DOE-FIU Science & Technology Workforce Development Initiative
Document number: FIU-ARC-2016-800006473-04b-251

Each document will be submitted to OSTI separately under the respective project title and document number as shown above.

DISCLAIMER

This report was prepared as an account of work sponsored by an agency of the United States government. Neither the United States government nor any agency thereof, nor any of their employees, nor any of its contractors, subcontractors, nor their employees makes any warranty, express or implied, or assumes any legal liability or responsibility for the accuracy, completeness, or usefulness of any information, apparatus, product, or process disclosed, or represents that its use would not infringe upon privately owned rights. Reference herein to any specific commercial product, process, or service by trade name, trademark, manufacturer, or otherwise does not necessarily constitute or imply its endorsement, recommendation, or favoring by the United States government or any other agency thereof. The views and opinions of authors expressed herein do not necessarily state or reflect those of the United States government or any agency thereof.

TABLE OF CONTENTS

TABLE OF CONTENTS.....	i
LIST OF FIGURES	iii
LIST OF TABLES	ix
PROJECT 1 OVERVIEW	11
TASK 17.1.1 CFD MODELING OF NON-NEWTONIAN FLUIDS (FIU YEAR 6) 13	
EXECUTIVE SUMMARY	13
INTRODUCTION	14
NUMERICAL APPROACH	15
RESULTS & DISCUSSION.....	18
CONCLUSIONS.....	34
REFERENCES	36
APPENDIX A: Grid-Independence Test for Various RANS Simulations.....	37
APPENDIX B: Computation of Turbulent Quantities.....	39
APPENDIX C: Grid-Independence Test for Mean Velocity and TKE-Shear Rate Analysis	40
APPENDIX D: Matlab Code for Power Spectra Energy (PSD)	41
TASK 17.1.2 CFD VALIDATION OF JET IMPINGEMENT CORRELATIONS TANKS (FIU YEAR 6)	42
EXECUTIVE SUMMARY	42
INTRODUCTION	43
NUMERICAL DETAILS	45
RESULTS AND DISCUSSIONS.....	50
CONCLUSIONS.....	64
REFERENCES	66
TASK 18.1 EVALUATION OF FIU’S SOLID-LIQUID INTERFACE MONITOR FOR ESTIMATING THE ONSET OF DEEP SLUDGE GAS RELEASE EVENTS (FIU YEAR 6).....	67
EXECUTIVE SUMMARY	67
INTRODUCTION	68
EXPERIMENTAL TESTING	70
RESULTS	72
CONCLUSIONS AND FUTURE WORK	86
REFERENCES	87
TASK 18.2 DEVELOPMENT OF INSPECTION TOOLS FOR DST PRIMARY TANKS (FIU YEAR 6)	88
EXECUTIVE SUMMARY	88
INTRODUCTION	89

MAGNETIC MINIATURE ROVER	90
PNEUMATIC PIPE CRAWLER	99
CONCLUSIONS AND FUTURE WORK	115
TASK 18.3 INVESTIGATION USING AN INFRARED TEMPERATURE SENSOR TO DETERMINE THE INSIDE WALL TEMPERATURE OF DSTs (FIU Year 6).....	116
EXECUTIVE SUMMARY	116
INTRODUCTION	117
SENSOR AND BENCH SCALE TESTS.....	118
RESULTS AND DISCUSSION	121
CONCLUSIONS AND FUTURE WORK	124
REFERENCES	125
TASK 19.1 PIPELINE CORROSION AND EROSION EVALUATION (FIU YEAR 6)	126
EXECUTIVE SUMMARY	126
INTRODUCTION	127
CONCLUSIONS.....	138
REFERENCES	139
TASK 19.2 EVALUATION OF NONMETALLIC COMPONENTS IN THE WASTE TRANSFER SYSTEM (FIU YEAR 6).....	140
EXECUTIVE SUMMARY	140
INTRODUCTION	141
EXPERIMENTAL TESTING	142
CONCLUSIONS AND FUTURE WORK	150
REFERENCES	151

LIST OF FIGURES

Figure 1. Characteristics of visco-plastic fluids: (a) typical rheogram and (b) variation of alpha with shear rate.	16
Figure 2. Two-dimensional computational domain containing 2117 cells.	16
Figure 3. Comparison between velocity profiles obtained for the laminar case by laminar and turbulent solvers at $Re = 550$: (a) HB and SRC methods (b) direct α -methods, and (c) inverse and direct- α methods.	19
Figure 4. Velocity profile for the transient case ($Re = 3400$).	20
Figure 5. Velocity profiles for the turbulent case.	21
Figure 6. Comparison of velocity profiles obtained for the flow in various regimes.	22
Figure 7. Variation of viscosity in radial direction at $X=0.98L$ in different flow regimes.	24
Figure 8. Computational grid containing 8.6m grid cells.	25
Figure 9. Axial velocity (on left) and shear rate (on right) for RANS and QDNS simulations. ..	25
Figure 10. Comparison between the results of RANS and QDNS simulations.	26
Figure 11. Turbulent profiles obtained from the RANS modeling with 7328 cells	27
Figure 12. Variation of turbulent quantities at various Reynolds numbers. On the left: TKE-shear rate (in accord with Peltier et al. (2015). On the right: shear dependency in dissipative scales.	27
Figure 13. Comparison of shear dependency in QDSN-HB and RANS-alpha.	28
Figure 14. 3-D inlet velocity B.C., On left: profile constructed in Matlab. On right: Profile after SEM application in Star-CCM+.	29
Figure 15. Inlet velocity B.C., On let: No SEM applied, On right: SEM applied.	29
Figure 16. Measurement locations at the outlet of the computational domain.	30
Figure 17. Time history of velocity at 28 points (on left) and volume averaged viscosity (on right).	30
Figure 18. Axial velocity non-dimensional velocity against non-dimensional wall distance.	30
Figure 19. Turbulent velocity and shear dependency for Q-DNS as compared to the RANS.	31
Figure 20. PSD of axial velocity (u) obtained using Matlab for QDNS simulation.	32
Figure 21. PSD of axial velocity (u) obtained in Star-CCM+ for QDNS simulations.	33
Figure 22. Schematic description of impinging and radial wall jets.	43
Figure 23. Schematic diagram of PJM vessel describing mechanism of flow structures that show formation of radial wall jets by normal impingement of single jets at small aspect ratio. ...	44
Figure 24. Computational domain of (a) large jet to impingement distance ratio of $b(d=12)$ and (b) small jet to impingement distance ratio of $b(d=1.5)$	46

- Figure 25. Schematic of PJM geometry and computational domain showing the geometrical dimensions with associated boundary conditions and the probe locations of radial velocity data extraction (a) 3D-quarter scaled down PJM vessel geometry and (b) 2D plane of symmetry on which data was sampled..... 47
- Figure 26. Computational mesh showing polyhedral mesh properties (a) flat surface geometry with $bd = 12$ and (b) flat surface geometry with $bd = 1.5$ and (c) PJM curved geometry with $bd = 1.5$ 49
- Figure 27. Grid sensitivity test on mean velocity profiles (a) Circular Jet region (b) Radial wall jet region at $r/b = 1$ and (c) Radial wall jet region at $r/b = 2$ 52
- Figure 28. Contours of velocity magnitude illustrating various regimes of circular jet, impingement region and formation of radial wall jet for flat surface geometry at jet to impingement distance of $bd = 12$ 53
- Figure 29. Comparison of wall-normal distribution of radial wall jet velocity profiles at radial locations; (absolute scale) (a) $rb = 1$ (b) $rb = 1.5$ (c) $rb = 2$ (d) $rb = 2.5$ 54
- Figure 30. Comparison of wall-normal distribution of radial wall jet velocity profiles at radial locations; (normalized scale) (a) $rb = 1$ (b) $rb = 1.5$ (c) $rb = 2$ (d) $rb = 2.5$ 55
- Figure 31. Comparison of wall-normal distribution of radial wall jet velocity profiles at radial location at $rb = 1$; (normalized scale)..... 56
- Figure 32. Comparison of radial variation(rb) of maximum radial wall jet velocity for $12 \leq rd \leq 30 \sim 1 \leq rb \leq 2.5$; (a) maximum radial wall jet velocity (U_m) (b) non-dimensional maximum radial wall jet velocity U_{mbK} 57
- Figure 33. Comparison of radial variation (rb) of radial wall jet thickness for $12 \leq rd \leq 30 \sim 1 \leq rb \leq 2.5$; (a) radial wall jet thickness δ (b) non-dimensional radial wall jet thickness δ_b 58
- Figure 34. Contours of velocity magnitude illustrating various regimes of circular jet, impingement region and formation of radial wall jet for flat surface geometry at jet to impingement distance of $bd = 1.5$ 59
- Figure 35. Comparison of radial variation (rd) of maximum radial wall jet velocity for $12 \leq rd \leq 30 \sim 8 \leq rb \leq 20$; (a) maximum radial wall jet velocity (U_m) (b) non-dimensional maximum radial wall jet velocity U_{mbK} 60
- Figure 36. Comparison of radial variation (rd) of radial wall jet thickness for $12 \leq rd \leq 30 \sim 8 \leq rb \leq 20$; (a) radial wall jet thickness δ (b) non-dimensional radial wall jet thickness δ_b 60
- Figure 37. Contours of velocity magnitude at 2D-symmetric plane illustrating various regimes of circular jet, impingement region and formation of radial wall jet for 3D quarter scale PJM vessel with curved impinging surface at a jet to impingement distance of $bd = 1.5$ 62
- Figure 38. Comparison of radial variation (rb) of maximum radial wall jet velocity for $1.5 \leq rd \leq 7.5 \sim 1 \leq rb \leq 5$; (a) maximum radial wall jet velocity (U_m) (b) non-dimensional maximum radial wall jet velocity U_{mbK} 62

Figure 39. Comparison of radial variation (rb) of radial wall jet thickness for $1.5 \leq r_d \leq 7.5 \sim 1 \leq r_b \leq 5$; (a) radial wall jet thickness δ (b) non-dimensional radial wall jet thickness δb 63

Figure 40. Commercial 3D Profiling Sonar and electronic control box (right) and the gooseneck reel deployment platform (left) which together comprise SLIM. 69

Figure 41. Plate of pebbles for sonar imaging and bubble wrap (left) and bubble wrap inserted under pebbles (right). 73

Figure 42. 3D Sonar in test tank directly above plate with pebbles. 73

Figure 43. Sonar image of large metal plate with small dish of pebbles in the center. 74

Figure 44. Sonar image of dish with pebbles on a large metal plate (left) and bubble wrap added to dish (right)..... 74

Figure 45. Photograph of plastic lid filled with sand on an aluminum plate on the tank bottom. The 3D sonar can be seen in the center top of the photograph. 75

Figure 46. Baseline 3D sonar image of the lid filled with sand on the aluminum plate with 4 wires to raise the plate and the solids uniformly 1 mm at a time..... 75

Figure 47. 3D sonar image of the lid filled with sand on the aluminum plate with 4 wires used to raise the plate and the solids uniformly 1 cm from the baseline position..... 76

Figure 48. Air bladder with metal weights underneath taped to a plastic lid (left) and same object with paver sand on top (right). 77

Figure 49. Three 3D sonar images are shown with: no air in bladder (left); with 1st increment of air to the bladder; and after 2nd increment of air to the bladder..... 77

Figure 50. Photograph of sonar in the test tank and the target circular disc of sand. 78

Figure 51. 2D, top view and 3D views of sonar imaging circular disc of sand at a distance of 45.92 cm..... 79

Figure 52. Images of same mound of sand with mounded sand atop but from 2 different sonar heights. 80

Figure 53. Images from same sonar height but with differing volumes in air bladder. 80

Figure 54. Test object with circles of sand of varying heights and diameters measured to mm resolution..... 81

Figure 55. Sonar image of the circles of sand..... 81

Figure 56. Plaster object used to test and correct volume calculation. 83

Figure 57. Sonar image of the plaster object used to help correct volume measurement..... 83

Figure 58. Sonar image of a brick in a test tank at FIU. 84

Figure 59. Sonar image of sand inside 3 concentric metal rings. 84

Figure 62. Filtered and post-processed sonar data of brick on a tank floor..... 85

Figure 63. Sonar image of tank floor with a brick in 3D mapper. 85

Figure 64. Inspection entry points of the AY-102 double-shell tank.	89
Figure 65. Side view of primary tank and refractory air slot.	90
Figure 66. Refractory air slot layout and description for AY-102.	90
Figure 67. Debris seen in refractory air slots.	91
Figure 68. Exploded view of previous design iteration.	92
Figure 69. Assembled model of the inspection tool.	92
Figure 70. Exploded view of the current design of the inspection tool.	93
Figure 71. 3D printed components (left), assembled inspection tool (right).	93
Figure 72. Cable management system for inspection tool.	94
Figure 73. Magnetic force testing and results.	95
Figure 74. Inspection tool tested inside a (a) 3” and (b) 4” pipe bench scale.	95
Figure 75. Magnet to surface spacing in various sized pipes.	96
Figure 76. Inspection tool testing in pipes.	96
Figure 77. The corroded pipes used for navigation test b) debris build up on the magnets after 100 feet of navigation.	97
Figure 78. Test set up for navigation over a gap.	97
Figure 79. Laboratory scale test bed created for determining the pull force created by tether. ...	98
Figure 80. Comparison of the tether pull-force inside the test bed.	98
Figure 81. AY-102 air supply lines.	99
Figure 82. FIU’s pneumatic pipe crawler.	100
Figure 83. Peristaltic locomotion.	100
Figure 84. Pneumatic pipe crawler.	101
Figure 85. Overall schematic of pneumatic pipe crawler.	101
Figure 86. Expansion module.	102
Figure 87. Gripper module.	102
Figure 88. Design evolution of the gripper modules.	102
Figure 89. Gripper claws with hinged pads.	103
Figure 90. Electric gripper preliminary design.	103
Figure 91. Camera module.	104
Figure 92. Original front camera case and redesign.	104
Figure 93. Piping misalignment and front camera overcoming misalignment.	104
Figure 94. Module flexible connection (left), guide mechanism (right).	105
Figure 95. Guide mechanism illustration.	105

Figure 96. Schematic of crawler’s recent design.	105
Figure 97. Strengthened suspension guides.	106
Figure 98. Control box schematic.	106
Figure 99. Control box cover.	107
Figure 100. Control box.	107
Figure 101. Tether line.	107
Figure 102. Instrumentation module.	108
Figure 103. Micro USB hub.	109
Figure 104. Force sensitive resistor.	109
Figure 105. MCP9808 precision I2C temperature sensor.	110
Figure 106. Bench scale pull tests.	110
Figure 107. Modular bench scale testbed.	111
Figure 108. Crawler navigating through a 3” elbow.	111
Figure 109. AY-102 ventilation riser.	112
Figure 110. Ventilation riser mockup.	112
Figure 111. Layout of the ventilation riser mockup.	113
Figure 112. Ventilation riser mockup.	113
Figure 113. Preliminary tether pull and drag testing.	113
Figure 114. Full scale testing.	114
Figure 115. (a) Raytek Sensor [4] and (b) Sensor Head [4]	118
Figure 116. (a) IR sensor through the annulus and (b) Test set up (block diagram).	119
Figure 117. Experimental set up including sensors.	119
Figure 118. (a) Temperature contours (Test 1) and (b) Temperature contours (Test 2).	122
Figure 119. Temperature contours using thermal camera.	123
Figure 120. (a) Heat transfer through the plate/wall and (b) temperature profile (plate cross section).	123
Figure 121. Cross section of a typical contact transducer 2.	129
Figure 122. Typical layout of the Pipe Wrap system [1].	130
Figure 123. Installed Pipe Wrap™ system on a 2” diameter pipe [1].	131
Figure 124. UT sensor system conceptual design [1].	131
Figure 125. (a) Measurements using the Olympus UT system and (b) Vacuum tests.	131
Figure 126. Acellent Smart sensor UT system 3.	132
Figure 127. Smart Layer attached to a pipe 3.	133

Figure 128. (a) Smart sensor placed on a pipe and (b) Oscilloscope tests using the smart sensor. 133

Figure 129. EMAT Temate band [4]. 134

Figure 130. (a) Ultrasonic couplant free contact sensors [5] and (b) Experimental set up. 135

Figure 131. (a) Sensors in contact and (b) oscillogram. 135

Figure 132. (a) Adjacent sensors and (b) oscillogram. 136

Figure 133. (a) UT sensors, (b) Wireless network, and (c) Mounting system [8]. 136

Figure 134. (a) Permasense corrosion monitoring system 9 and (b) Permasense WT 210 series UT sensor [8]. 137

Figure 135. Coupon dumbbells..... 142

Figure 136. EPDM coupon testing..... 143

Figure 137. Load vs extension for EPDM. 144

Figure 138. Garlock coupon testing..... 144

Figure 139. Load vs extension for Garlock®. 145

Figure 140. Ruptured HIHTL test specimen..... 146

Figure 141. O-ring pressure test rig. 147

Figure 142. Gasket baseline pressure test rig..... 147

Figure 143. In-service component aging loop. 148

Figure 144. Thermostatically controlled tank heater. 149

Figure 145. Coupon Aging Vessel..... 149

LIST OF TABLES

Table 1. Boundary Conditions, Geometry and Fluid Properties in RANS Simulations.....	17
Table 2. Error Analysis Study for Different Methods and Flow Regimes	22
Table 3. Improvement of Percentage Error for Different Methods and Flow Regimes	23
Table 4. Error Values Calculated for the Best Results of the Alpha Method and Peltier et al. (2015)'s Results	23
Table 5. Mesh-dependent Turbulent Quantities of the Flow	25
Table 6. Test Matrix.....	79
Table 7. Test Matrix (Temperature in °F).....	120
Table 8. Temperature(°F) Results Test 1 (IR Sensor and Thermocouple).....	121
Table 9. Temperature(°F) Results Test 2 (IR Sensor and Thermocouple).....	122
Table 10. Baseline Coupon Hardness Test Results - Garlock® Data.....	143
Table 11. Average Test Results from EPDM	144
Table 12. Average Test Results from Garlok® Coupons	145
Table 13. Baseline HIHTL Pressure Test Results.....	146
Table 14. Baseline O-ring Pressure Test Results.....	147
Table 15. Baseline Gasket Pressure Test Results	148
Table 16. Coupon Aging Matrix.....	149

PROJECT 1 OVERVIEW

The Department of Energy's (DOE's) Office of Environmental Management (EM) has a mission to clean up the contaminated soils, groundwater, buildings and wastes generated over the past 60 years by the R&D and production of nuclear weapons. The nation's nuclear weapons complex generated complex radioactive and chemical wastes. This project is focused on tasks to support the safe and effective storage, retrieval and treatment of high-level waste (HLW) from tanks at Hanford and Savannah River sites. The objective of this project is to provide the sites with modeling, pilot-scale studies on simulated wastes, technology assessment and testing, and technology development to support critical issues related to HLW retrieval and processing. Florida International University (FIU) engineers work directly with site engineers to plan, execute and analyze results of applied research and development.

Although a number of tasks have been initiated and completed over the course of the cooperative agreement, at the end of this past year, there were 6 active tasks. These tasks are listed below and this report contains a detailed summary of the work accomplished for FIU's Performance Year 6.

Task 17.1 – CFD Modeling of HLW Processes in Waste Tanks: The objective of this task is to provide the sites with mathematical modeling, validation, and testing of computer programs to support critical issues related to HLW retrieval and processing. Specifically, FIU is developing a CFD models based on the Star-CCM+ framework to simulate mixing and retrieval processes for HLW at Hanford. This has led to two subtasks. One is focused on improving the modeling of non-Newtonian fluids by modifying approaches to characterize the viscosity and the second is related to the validation of the jet impingement correlations for the modeling of pulse jet mixers.

Task 18.1- Evaluation of FIU's Solid-Liquid Interface Monitor (SLIM) for Estimating the Onset of Deep Sludge Gas Release Events: The objective of this subtask is to evaluate SLIM for its ability to image sludge surfaces and determine whether a DSGRE is about to occur. Pilot-scale testing will be conducted to evaluate SLIM's resolution and its ability to identify topographical changes in a sludge surface due to the formation of a gas bubble.

Task 18.2 – Development of Inspection Tools for DST Primary Tanks: The objective of this task is to develop inspection tools that will assist engineers in evaluating the structural integrity of the primary tank floors in the double shell tanks (DSTs) double-shell tank at the Hanford DOE site. This effort has led to the development of two inspection tools (two subtasks within Task 18.2), both able to provide live visual feedback; a magnetic wheeled miniature motorized rover that can travel through the refractory cooling channels under the primary tank, and a pneumatic pipe crawler that can inspect the tank ventilation header pipes and tank central plenum.

Task 18.3 - Investigation Using Infrared Temperature Sensors to Determine Inside Wall Temperatures of DSTs: Engineers at Hanford are interested in understanding the temperatures inside the primary tanks to safeguard against exceeding specified limits. The objective of this task is to evaluate the ability of IR sensors to detect inner tank wall temperatures from the annulus of the DST's via bench scale testing.

Task 19.1 – Pipeline Erosion and Corrosion Evaluation: The objective of this task is to provide the sites with a means to evaluate the structural integrity of waste transfer pipeline components. This has involved the evaluation of potential sensors and the viability of utilizing them to provide real time data for long durations of time. The sensors can be installed and provide

thickness measurements of pipeline components and fittings found in jumper pits, evaporators, and valve boxes.

Task 19.2 – Evaluation of Non-metallic Components in the Waste Transfer System: The objective of this task is to provide the Hanford Site with data obtained from experimental testing of the hose-in-hose transfer lines, Teflon® gaskets, EPDM O-rings, and other nonmetallic components used in their tank farm waste transfer system under simultaneous stressor exposures. The stressor exposure experiments will be limited to various combinations of simultaneous stressor exposure of caustic solutions, high temperatures and high pressure stressors. Evaluation of baseline materials will be conducted and compared with materials that have been conditioned with the various stressors.

TASK 17.1.1

CFD MODELING OF NON-NEWTONIAN FLUIDS (FIU YEAR 6)

EXECUTIVE SUMMARY

The Waste Treatment and Immobilization Plant (WTP) will house pulsed jet mixers (PJMs) in waste processing tanks that require improved computer models for the prediction of slurry mixing behavior. The nature of the high level-waste (HLW) in these tanks can be represented using non-Newtonian fluids that can be described by the Herschel-Bulkley (HB) model for viscosity. The computational modeling of HLW processes such as the operation of PJMs, utilize this viscosity definition in a Reynolds-averaged Navier-Stokes equations (RANS) model. RANS models employ scale averaging of flow features and therefore are computationally more desirable due to their higher speed and relatively lower memory requirements compared to the direct numerical simulation (DNS) methods that fully resolve all structures of the turbulent flow. However, the RANS models suffer from lack of accuracy due to inadequate representation of the shear rate.

Improvements can be obtained by using a modified definition of viscosity based on the shear rate which can be derived from the dissipation rate of turbulent kinetic energy (TKE), or directly imposed on the shear rate, which is considered to be an indirect method. One may extract data directly from an experiment or from a DNS simulation to construct a modified approach. Experimental investigation requires measurements conducted at extremely high resolution of time and space scales in order to capture the variation of shear and viscosity in the smallest eddies. A DNS-based modification is more practical since it is obtained from resolving the entire or large portion of the turbulent scales.

During the past year, FIU's goal was to improve the predictions of the k - ϵ turbulence model by developing both RANS and DNS-based modification models which were applied through the entire computational domain (as opposed to models in the literature which apply to local regions of the flow, Soto and Shah, 1976). The modifications aimed to improve the results for laminar, transitional, and turbulent regimes with Reynolds numbers of 550, 3,400 to 25,300. Recently, FIU developed an approach to quantify the non-linearity of the stress-strain profile of the non-Newtonian slurry and iteratively converge to modified values of the viscosity that could significantly improve the simulation results for flow of non-Newtonian flows of Bingham-type fluids.

INTRODUCTION

There have been valuable efforts published in the literature to improve accuracy of numerical algorithms in the prediction of flow characteristics of non-Newtonian fluids. Wilson and Thomas (1986) improved the theory of the Power-law and Bingham plastic fluids for the log-law region of the velocity profile towards better prediction of the wall friction coefficient. Their analysis was based on drag reduction associated with non-Newtonian fluids and colloidal suspensions, as was first reported by Toms (1948), according to Andrade et al. (2007). This modification reflected enhanced viscosity effects for dissipative micro-eddies that possess small time and length scales. Soto and Shah (1976) developed an algorithm for simulation of an entrance flow of a yield-power-law fluid, which produced results in good agreement with analytical solutions for different yield stress and power-law exponents. Bartosik (2010) applied the theory of Wilson and Thomas (1985), which described a change of boundary layer thickness and suppression of turbulence in the boundary layer for slurry flow with very fine solid particles. Bartosik employed a k - ϵ turbulence model with modified damping functions and compared the performance of the power-law and Herschel and Bulkley models in the simulation of a Kaolin slurry. He found that the Herschel and Bulkley model (Herschel and Bulkley, 1926) better describes shear stress at a low shear deformation rate.

Despite these significant contributions, there is still a need to find a universal model to define viscosity properly in an entire computational domain for different regimes of flow in a wide range of Reynolds numbers so that its applicability is not specific to a flow with certain material, geometry, and boundary conditions. One possible approach is to dynamically modify viscosity during the simulation. In this study, two different ways of achieving this goal were implemented. In the first approach, the parameters that affect the viscosity were modified. This approach was pursued in some studies mentioned in the review of the literature earlier, such as the method by Gavrilov and Rudyak (2014) which was designed to alter viscosity by correcting the definition of shear rate. In a second approach, viscosity was directly altered following a specific algorithm, which was based on the energy dissipation rate in non-linear fluids. FIU pursued the second approach in this effort and developed an algorithm based on the Herschel and Bulkley (HB) model of viscosity. The goal was to improve predictions of the k - ϵ turbulence model when the modifications were applied through the entire computational domain. Improved results for laminar, transitional and turbulent regimes, indicated by Reynolds number of 550, 3,400 to 25,300, respectively, were obtained.

NUMERICAL APPROACH

Proposed Modification Model: “alpha Model”

For this study, the modification model acted only on dissipative eddies of the flow. This is possible by using the dissipation rate scalar (ϵ) obtained from closure equations of Reynolds-averaged Navier-Stokes (RANS) equations for turbulent kinetic energy and its dissipation rate. FIU proposed a modification model last year and continued to investigate the model’s performance. With little alterations, the proposed model (alpha model) now has the following formulation:

$$\mu_{\text{subs.}} = \begin{cases} \mu_{\text{HB}} = \frac{|\tau|}{\gamma} = \frac{\tau_y}{\gamma} + k \gamma^{(n-1)} & \epsilon \leq \epsilon_{\text{THS}} \\ \alpha^m \cdot \mu_{\text{ps_Nwt}} & \epsilon > \epsilon_{\text{THS}} \end{cases} \quad (1)$$

where μ_{sub} is the viscosity that is used in every iteration after calculation of the HB viscosity and τ , τ_y , k , γ , and n are shear stress, yield shear stress (4.42 Pa), consistency (0.242 Pa.sⁿ), shear rate (obtained from the Navier-Stokes equations), and power exponent (0.534), respectively. Alpha (α) is the non-linearity parameter of this model and measures the deviation of energy dissipation rate in a non-Newtonian fluid flow from that of a Newtonian fluid flow. For this purpose, a pseudo-Newtonian case is constructed in each iteration from shear-strain, or a rheogram, using a straight shear-strain line emanating from the origin. Slope of this line is called the pseudo-Newtonian viscosity and is represented by $\mu_{\text{ps_Nwt}}$ in Eq.(1). If a point of this line lies on the global maximum of the rheogram curve, then the global quantities (i.e. α_{glo} and $\mu_{\text{ps_Nwt.glo}}$) are used. For any other points on the rheogram curve, local quantities are used (i.e. α_{loc} and $\mu_{\text{ps_Nwt.loc}}$). All these parameters along with variation of non-linearity parameter (α) are shown in Figure 1. The condition parameter of the model is ϵ_{THS} , threshold value of dissipation rate, which is used to identify cells that qualify for modifications. This parameter was set to zero in this work in order to maximize sensitivity of the alpha method. Another parameter of the model is “m” which is the exponent of alpha and is set to 1 for the direct alpha method and -1 for inverse alpha method. Local and global versions of alpha and pseudo-Newtonian viscosity variables are defined as:

$$\alpha_{\text{loc}} = 2 \times \frac{\tau_y + \frac{K(\gamma)^n}{n+1}}{\tau_y + K(\gamma)^n}, \quad \alpha_{\text{glo}} = 2 \times \frac{\tau_y + \frac{K(\gamma_{\text{max}})^n}{n+1}}{\tau_y + K(\gamma_{\text{max}})^n} \quad (2)$$

$$\mu_{\text{ps_Nwt.loc}} = \frac{\tau_{\text{HB}}}{\gamma} = \frac{\tau_y}{\gamma} + k \gamma^{(n-1)}, \quad \mu_{\text{ps_Nwt.glo}} = \frac{\tau_{\text{HB_max}}}{\gamma_{\text{max}}} = \frac{\tau_y}{\gamma_{\text{max}}} + k \gamma_{\text{max}}^{(n-1)} \quad (3)$$

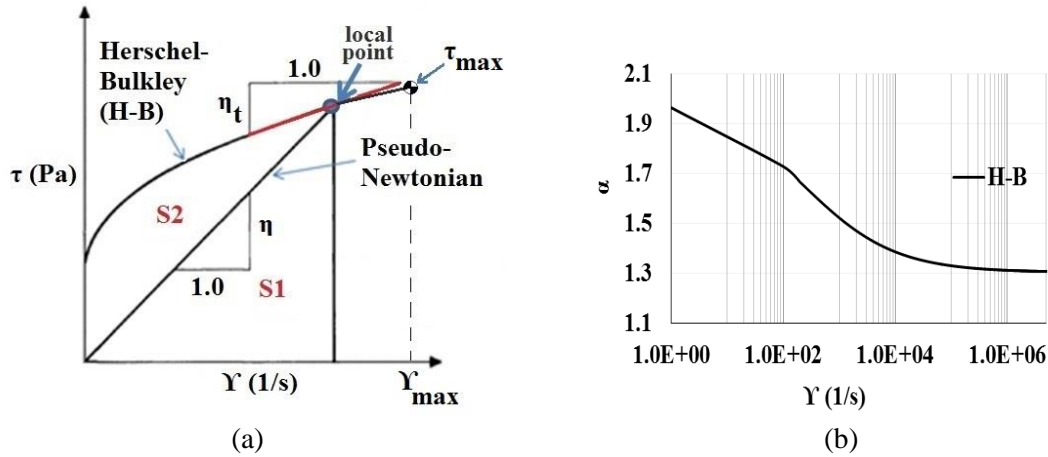


Figure 1. Characteristics of visco-plastic fluids: (a) typical rheogram and (b) variation of alpha with shear rate.

FIU also implemented the method of Gavrilov and Rudyak (2014), namely the SRC method, in Star-CCM+ simulations for verification purposes. The SRC method is an indirect method of viscosity correction in simulation of pipe flow of Bingham fluids and is defined as:

$$|\dot{\gamma}|_{SRC}^2 = 2 S_{ij}S_{ij} + \langle 2 \acute{S}_{ij}\acute{S}_{ij} \rangle = 2 S_{ij}S_{ij} + \frac{\epsilon\rho}{\mu_{HBSRC}}. \tag{4}$$

Simulation Verification Using RANS-alpha Model

RANS modeling of non-Newtonian Bingham fluid flow in a pipe was performed using the software Star-CCM+. Figure 2 shows the periodic axisymmetric computational domain which contains 2,117 cells along with a line probe that was used for measurements. This grid is very similar to a grid used by Peltier et al. (2015) in their simulations. FIU used finer grids containing 7328 (~198×37), 20447 (~393×52), and 28615 (~432×66) cells for grid-independence tests in occasions where convergence to an unchanging solution was needed. Boundary conditions, as well as dimensions of computational domain, and properties of Bingham fluid, are presented in Table 1.

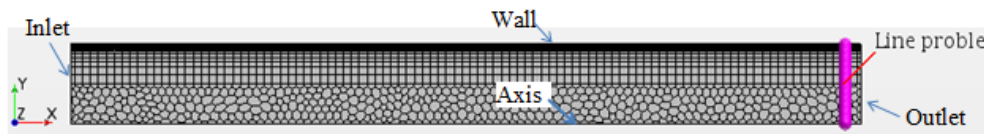


Figure 2. Two-dimensional computational domain containing 2117 cells.

Table 1. Boundary Conditions, Geometry and Fluid Properties in RANS Simulations

Boundary conditions			
CASE	RE = 550	RE = 3400	RE = 25300
Inlet velocity, v_i (m/s)	0.52	1.09	2.03
Mass flow rate, \dot{m} (kg/s)	4.08	8.56	15.94
Pressure at outlet	1atm	1atm	1atm
wall	Non-slip wall	Non-slip wall	Non-slip wall
domain	Periodic	Periodic	Periodic
Fluid properties		Pipe dimensions	
Density, ρ (kg/m ³)	1000	Length (m)	0.5
Yield stress, τ_y (pa)	4.42	Diameter (m)	0.1
Consistency factor, k (Pa.s ⁿ)	0.242	Number of prism layer	20
Exponent, n	0.534	Mesh (Polyhedral + Hexahedral)	

Profiles of viscosity and axial velocity were obtained at a location close to the outlet of the domain, where less than 1% change in the profile was observed (fully developed profile was observed at $x = 0.98L$, where L is length of the periodic pipe). Small changes of mean quantities (i.e. axial velocity on line probe and domain-averaged viscosity) were criteria for reaching a steady state solution. Data associated with field variables, such as axial velocity, wall-averaged viscosity, and shear rate at the wall, were reported once the mean quantities of criteria didn't change with additional iterations.

RESULTS & DISCUSSION

Case 1: Re = 550 (Laminar Flow)

In laminar flow, viscosity plays a dominant role and it was predicted that simulation results were significantly sensitive to the viscosity models used. For the HB method, as Figure 3(a) shows, shear rate was over-predicted near the wall and under-predicted in the core flow region. The global percentage error for this method was 18.2%. Here, FIU used the turbulent k- ϵ solver for this laminar flow (Re = 550) and interestingly it was observed that results were not different from the laminar solver's results by more than 0.05 percent. Thus, FIU applied the alpha method with both laminar and turbulent solvers for this case. To enable application of the alpha method with the laminar solver, the condition of the alpha model ($\epsilon > \epsilon\text{-THS}$) was ignored and the modification term, $\alpha^m \times \mu_{ps_Newt}$, was used for the entire computational domain. Results of this implementation are shown in Figure 3(b) for both global and local alpha methods. Similar to the H-B method, no significant difference was observed when laminar and turbulent solvers were used. In addition, comparison between Figure 3(a) and Figure 3(b) reveals that the H-B and local alpha method behaved very similarly.

For the global alpha method, an excellent match with the experiment was obtained in the region that was closer to the wall ($0.6 < r/R < 1$). In contrast, significant deviations from the experimental data occurred for the core flow region ($0 < r/R < 0.6$). These deviations were significantly lessened by using the inverse global alpha method in combination with the k- ϵ turbulent solver, as shown in Figure 3(c). Error analysis showed that, on average, application of the inverse global alpha method resulted in a 42.2% improvement of predictions as compared to the H-B method. In the case of the SRC method, since the dissipation rate was used directly in the SRC model, ignoring relevant terms would make the SRC model equivalent to the original HB model. The analysis showed that implementation of the SRC model in combination with the k- ϵ turbulence solver resulted in 8.6% higher error in comparison to the HB method.

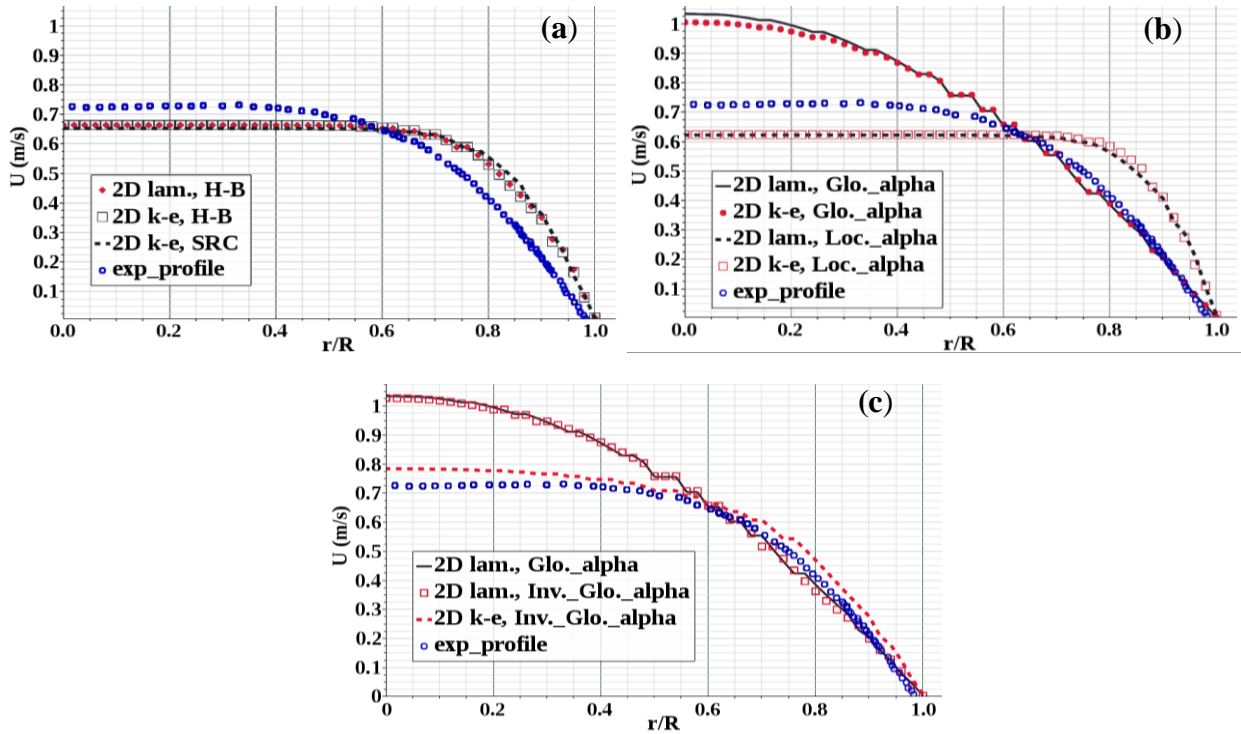


Figure 3. Comparison between velocity profiles obtained for the laminar case by laminar and turbulent solvers at $Re = 550$: (a) HB and SRC methods (b) direct α -methods, and (c) inverse and direct- α methods.

Case 2: $Re = 3400$ (Transitional Flow)

For the transitional flow case ($Re = 3400$), Figure 4, predictions obtained by the global- α method were significantly better than those of the original HB method. Improvements were observed over almost the entire length of the probe, where error was reduced by 48% in comparison to the HB method. These improvements were more pronounced in the core flow region, i.e., $r/R = [0$ to $0.55]$, where a 73% reduction of error was seen. Unlike this non-flat profile, the HB and shear correction (SRC) methods predicted similar flat profiles with only a 1.3% difference in the same region. Error with these flat profiles was almost 8% and the flatness of profiles was an indication of zero shear stress in this region. On the lower half length of probe, i.e., $r/R = [0.55$ to $1]$, deviation from experimental values was almost 51% for HB and SRC methods versus 29% for the global- α method. Unlike the global- α method, the local- α method produced similar results to the HB method and the maximum difference between these models was only 4.2%.

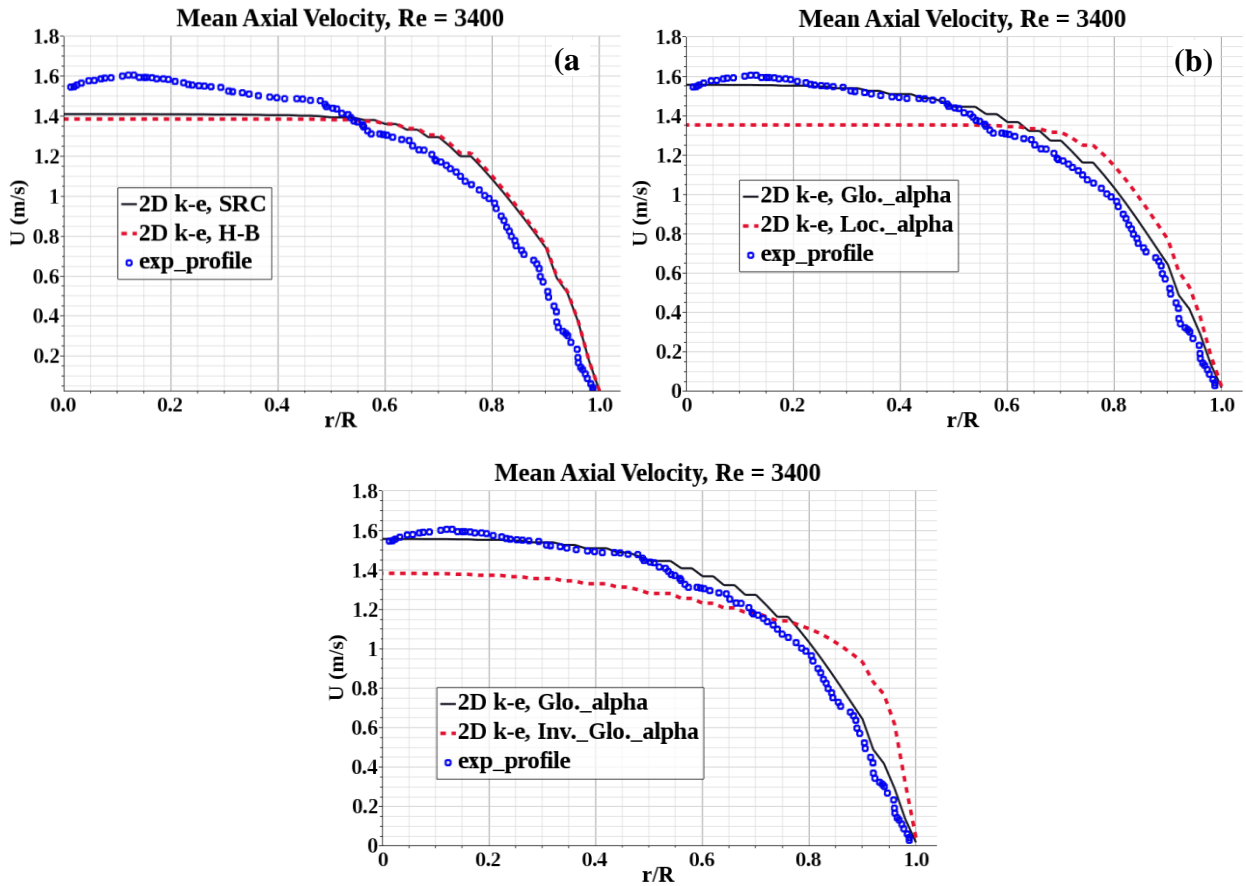


Figure 4. Velocity profile for the transient case ($Re = 3400$).

Case 3: $Re = 25300$ (Turbulent Flow)

For turbulent flow ($Re = 25300$), Figure 5, all models predicted the velocity profile accurately in the near wall region, i.e., in $r/R = [0.9 \text{ to } 1]$. In this region, implementation of the global- α resulted in a 2% increase of accuracy. In the median region, i.e., in $r/R = [0.45 \text{ to } 0.9]$, a maximum of 3% error was observed between the results of HB, SRC, and local- α methods. However, implementation of the global- α method resulted in lower velocity magnitudes, which better agreed with experimental data. This implementation results in a 45% reduction of error, in comparison to the HB method. In the core flow region, i.e., in $r/R = [0 \text{ to } 0.45]$, all methods over-predicted velocity and implementation of the global- α resulted in a 5% increase of accuracy. However, flat velocity profiles were obtained using HB and SRC methods in the core flow region $r/R = [0 \text{ to } 0.4]$, whereas the global- α method predicted a continuous trend of increase of axial velocity which was more consistent with experimental data. This analysis confirmed that the shear rate predicted by the global- α method was in better agreement with that of the experiment. In addition, implementation of the global- α method resulted in a 0.7% increase of accuracy in comparison to HB method.

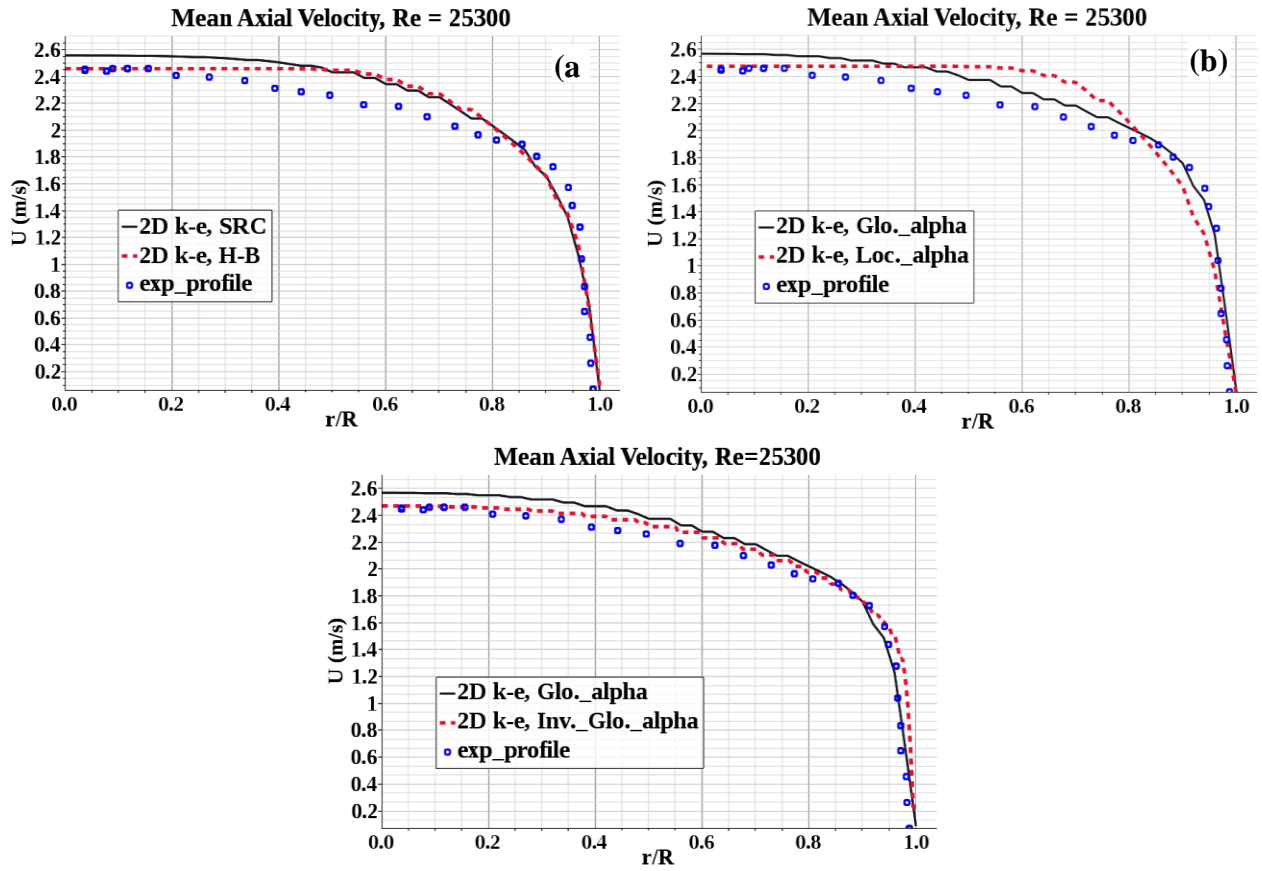


Figure 5. Velocity profiles for the turbulent case.

Further, FIU compared the best results obtained from the alpha method against the SRC and HB methods in three regimes of flow, as shown in Figure 6. Considering all plots in this figure, it is observed that results obtained by the alpha method are much closer to experimental values for almost all values of r/R . It is important to emphasize that results here are independent of grid resolution. This validation was obtained through a series of simulation studies using different grid sizes. In other words, the results displayed in Figure 3-6 were reported when no more variations in the velocity profile was observed with refinement of the grid spacing. Readers can refer to Appendix A of this report for a review of the results for the grid independency studies.

Quantification of error in prediction of the velocity profile was performed for all models and Reynolds numbers used in this work. Results of this analysis are shown in Table 2, where the lowest error values are shown in red for different cases. A comparison shows that the best results belong to the global and inverse global versions of the alpha method. Effectiveness of the alpha method became clearer when the HB method was used as a reference for calculation of percent improvement of the error for all other models. Table 3 shows 42%, 48%, and 61% improvements of error when the alpha method was used.

Table 4 shows a comparison of the best results obtained by FIU's proposed model and other models used in the literature. In addition, results reported by the Peltier et al. (2015) with a similar investigation and using their proposed improvement method are included. These results are labeled as Inkson (2015) in Table 4. The comparison shows the competitiveness of the alpha method for laminar flow and superiority of this method for turbulent flow. For transitional flow,

it is possible that a hybrid alpha method could be more competitive in regards to the method used by Peltier et al. (2015). In addition, a comparison between the error values of the RANS HB and RANS alpha methods reveals significant improvements obtained for all the Reynolds numbers used in flow simulations included in this report.

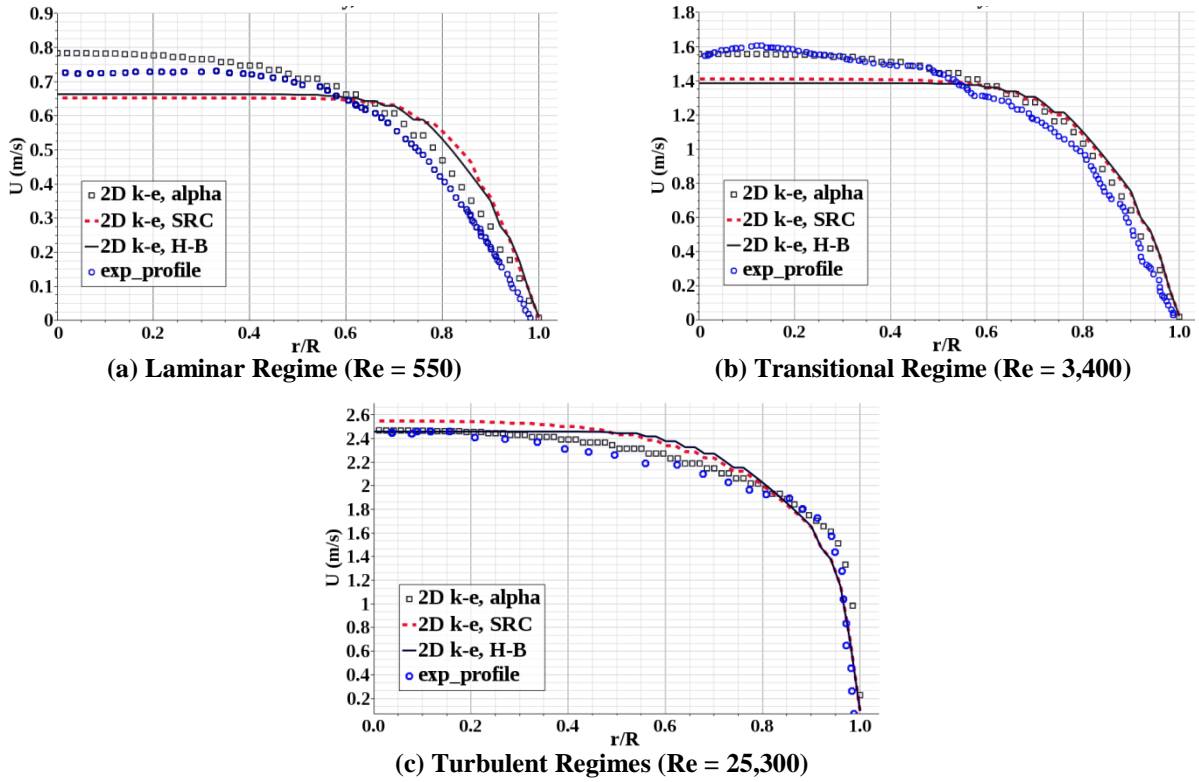


Figure 6. Comparison of velocity profiles obtained for the flow in various regimes.

Table 2. Error Analysis Study for Different Methods and Flow Regimes

Flow regime ➔	Percentage relative error Err. (%)*			
	Re = 550 ^a	Re = 550 ^b	Re = 3400	Re = 25300
HB	18.2	17.4	28.2	4.5
SRC	-	19.8	26.8	6.2
local_alpha	25.6	25.8	30.5	6.3
global_alpha	20.3	19.1	14.7	4.7
Inv._local_alpha	14.9	14.5	35.7	3.3
Inv._global_alpha	20.4	10.5	52.5	1.7

a: Solved by the laminar solver in Star-CCM+

b: Solved by the k-ε solver in Star-CCM+

Table 3. Improvement of Percentage Error for Different Methods and Flow Regimes

Modification to percentage relative error Err. (%)*				
Flow regime →	Re = 550 ^a	Re = 550 ^b	Re = 3400	Re = 25300
HB	N/A	N/A	N/A	N/A
SRC	-	-8.6	4.7	-37.1
local_alpha	-40.7	-41.7	-8.1	-40.8
global_alpha	-11.8	-5.1	48.1	26.2
Inv._local_alpha	18.4	20.2	-26.7	-5.4
Inv._global_alpha	-11.9	42.2	-86.2	61.4

Negative values indicate increase of the error
a: Solved by the laminar solver in Star-CCM+
b: Solved by the k-ε solver in Star-CCM+

Table 4. Error Values Calculated for the Best Results of the Alpha Method and Peltier et al. (2015)'s Results

Percentage relative error Err. (%)*			
Flow regime →	Re = 550	Re = 3400	Re = 25300
H-B	17.4	28.2	4.5
SRC ^a	19.8	26.8	6.2
alpha (this work)	10.5	14.7	1.7
Inkson N. (2015)	8.1	5.1	9.2
Error improvement Err. _{imp} (%)**			
alpha (this work)	42.2	48.1	61.4

a The shear rate correction method of Gavrilov and Rudyak (2014)

$$* \text{Err}_{\text{avg.}} (\%) = \frac{100}{N} \times \sum_{\lambda=1}^N (|f_{\text{exp}}(\lambda) - f_{\text{sim}}(\lambda)|) / f_{\text{exp}}(\lambda)$$

$$** \text{Err}_{\text{imp.}} (\%) = 100 \times \frac{|(\text{Err}_{\text{avg.}})_{\text{models}} - (\text{Err}_{\text{avg.}})_{\text{HB}}|}{(\text{Err}_{\text{avg.}})_{\text{HB}}}$$

In addition, FIU extended the investigation to the analysis of viscosity in the span-wise direction at a location close to the outlet of the domain. Figure 7 shows the variation of viscosity for three flow regimes under investigation in this study. For each regime, the viscosity obtained from the direct- α method, referred to as α -viscosity, is shown in red dots and attains a constant value. For brevity, only the global-alpha method is considered for comparison here. A decrease of the α -viscosity is observed with an increase of Reynolds number (0.267 for Re = 550 and 0.028 for Re = 25300). In addition, all plots display a sudden increase of viscosity for the HB and SRC methods with an increase of distance from the solid boundary. In fact, these models are subject to singularities in the core flow region, where the shear rate approaches zero. This sudden increase of viscosity is delayed for the SRC method in the higher Reynold numbers, i.e, Re = 25,300. In addition, all plots in Figure 7 show an increase of the HB viscosity to α -viscosity in the wall region indicated by “region of increased viscosity”. This region is significantly wider in the laminar regime and reduces with an increase of the Reynolds number. On average, the increase of viscosity is approximately 112%, 58%, and 48% for laminar, transient, and turbulent flows,

respectively. This increase of viscosity resulted in approximately 72%, 43%, and 2% improved prediction of the velocity profile in comparison to the HB method.

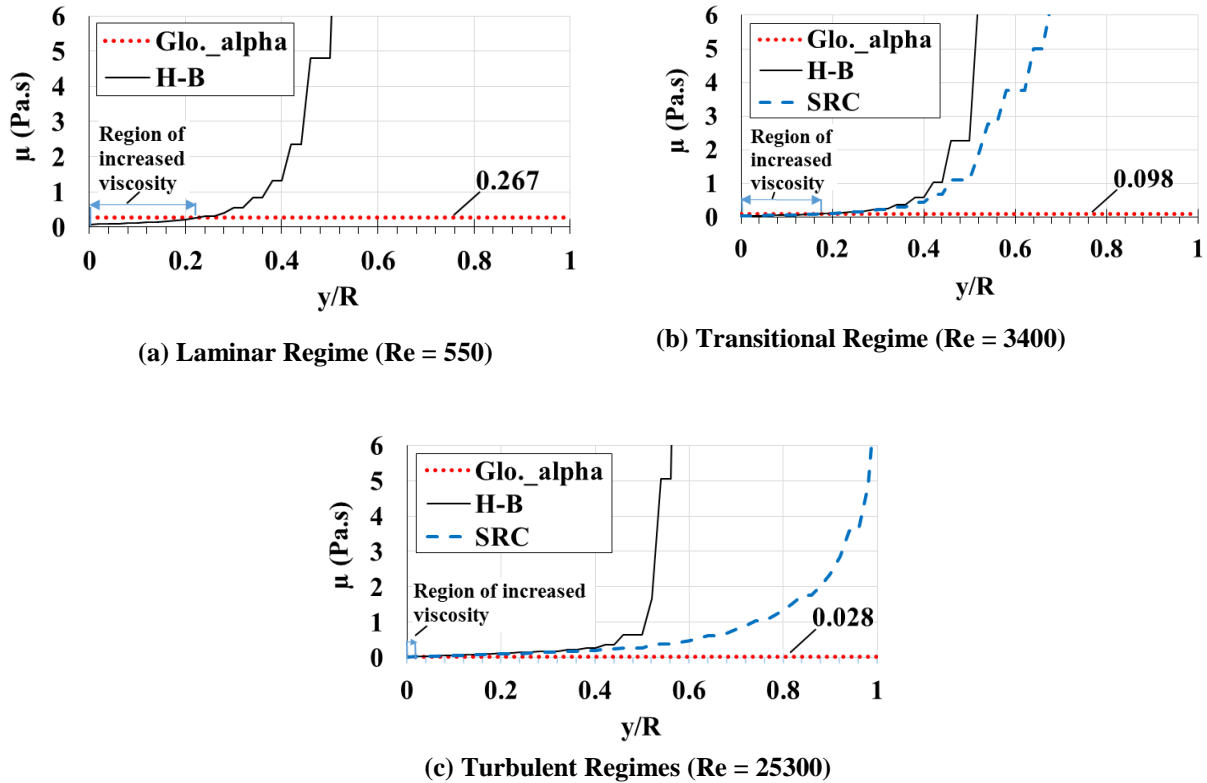


Figure 7. Variation of viscosity in radial direction at $X=0.98L$ in different flow regimes.

Q-DNS Simulation of Pipe Flow

Direct numerical simulation (DNS) is considered to be the most accurate approach in simulation of fluid flows. In DNS, equations are discretized with at least 4th order discretization schemes. In this approach, unlike RANS modeling, all length and velocity scales are resolved and no modeling is permitted. This accurate approach can be used to obtain a relationship between shear rate and length and velocity scales of dissipative eddies. In the investigation of viscosity, dissipative eddies (or scales) are of special importance since the viscosity effect (viscous dissipation) is dominant in these eddies. In DNS, these eddies can be separated from inertia and energy containing eddies using an energy spectra curve.

In Star-CCM+, a similar solver with up to second order discretization schemes is available and is called quasi-DNS or QDNS (term quasi is given due to the smaller order of accuracy). Another important and stringent limitation in QDNS simulations is the prohibition of simultaneous specification of the turbulence quantities at the inlet boundary and periodicity of domain. In QDNS simulations, Star-CCM+ only allows for turbulence specification using the Synthetic Eddy Model (SEM) and application of this model simultaneously with periodicity conditions results in a crash of the solver. Unfortunately, this restriction still exists in the latest version of Star-CCM+.

To avoid this issue, one solution was to use an adequately long pipe ($L \geq 10D$) to allow the velocity profile to fully develop. This set up requires at least 64 million elements, which was a

serious limitation of the QDNS analysis. However, it was possible to assign a fully developed interface between the inlet and outlet of the domain along with the SEM assigned at the inlet. Figure 8 shows the computational domain consisting of approximately 8 million points, which was finer than the computational domain used in analysis of Shams et al. (2011) for a similar simulation. A comparison was made to ensure that mesh-dependent quantities in the simulation were within acceptable bounds, as shown in Table 5.



Figure 8. Computational grid containing 8.6m grid cells.

Table 5. Mesh-dependent Turbulent Quantities of the Flow

Turbulent quantity	Shams et al., 2011	This work
Δr^+_{max}	11	7.3
$\Delta \theta^+_{max}$	5	2.2
Δz^+_{max}	8	15.5
Y^+	-	0.1
CFI	-	0.2

FIU compared results of the QDNS simulation with results from the RANS-HB and RANS-alpha simulations, as well as the experimental data for $Re = 25300$, as shown in Figure 9(a). Here, despite the fact that this QDNS result is significantly more accurate compared to previously reported QDNS results, predictions of the HB and RANS models are still more accurate. FIU compared the shear rate (SR) between four methods, as shown in Figure 9(b). It was observed that the QDNS reported the maximum shear rate in most of the core flow. Conversely, the RANS-alpha method reported the minimum shear rate in most of the core flow, except on the axis ($r/R = 0$).

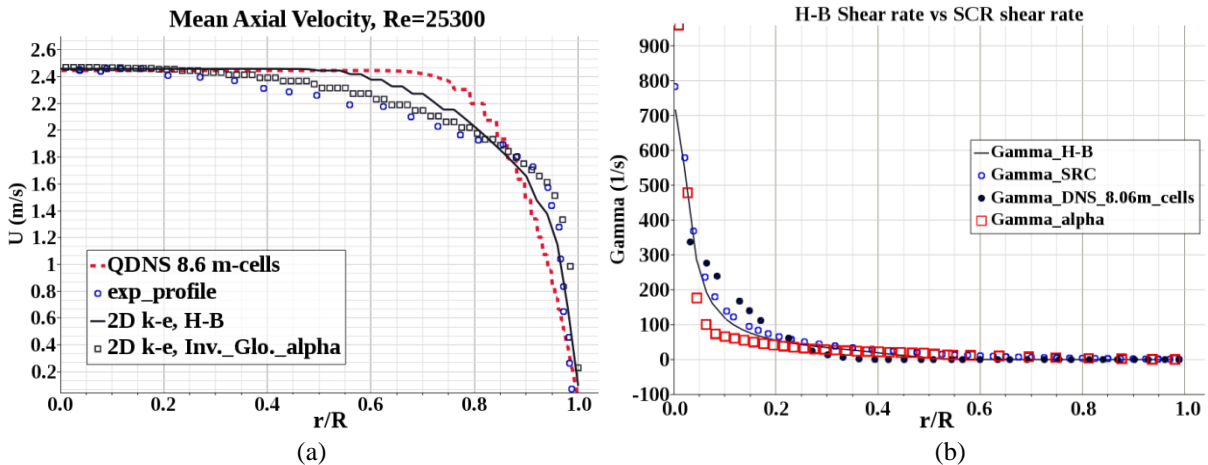


Figure 9. Axial velocity (on left) and shear rate (on right) for RANS and QDNS simulations.

Another complication in using QDNS modeling in Star-CCM+ was the absence of the direct computation of the turbulence kinetic energy (TKE) and turbulent dissipation rate (TDR) parameters. These parameters were needed for the purpose of verification of results, spectral

analysis, and separation of the dissipative eddies. A combination of user-field-functions was developed in Star-CCM+ to obtain fluctuating components of velocity field and calculate the TKE and TDR using gradients of fluctuations. TKE and TDR are defined using Eq. (5) and Eq. (6).

$$\text{TDR} = \varepsilon = \mu \left(2 \frac{\overline{\partial u^2}}{\partial x} + 2 \frac{\overline{\partial v^2}}{\partial x} + 2 \frac{\overline{\partial w^2}}{\partial x} + \overline{\left(\frac{\partial u}{\partial x} + \frac{\partial v}{\partial x} \right)^2} + \overline{\left(\frac{\partial u}{\partial x} + \frac{\partial w}{\partial x} \right)^2} + \overline{\left(\frac{\partial v}{\partial x} + \frac{\partial w}{\partial x} \right)^2} \right) \quad (5)$$

$$\text{TKE} = K = \frac{1}{2} (\overline{u^2} + \overline{v^2} + \overline{w^2}) = \frac{1}{2} (u_{\text{rms}}^2 + v_{\text{rms}}^2 + w_{\text{rms}}^2) \quad (6)$$

Calculation of the TDR term using Eq. (5) was made possible through a series of field functions developed by FIU in Star-CCM+. Readers can refer to details of this implementation in Appendix B of this report. FIU compared the TDR obtained from QDNS simulation against TDRs from the RANS alpha and RANS HB methods. Figure 10 shows that, unlike the RANS-alpha method that predicts maximum of TDR at the wall, the QDNS-HB modeling predicted a maximum dissipation rate in core regions of flow. These inaccuracies associated with the QDNS modeling can be related to the absence of periodicity and inaccurate turbulent quantities set at the inlet and outlet boundaries of the domain during modeling.

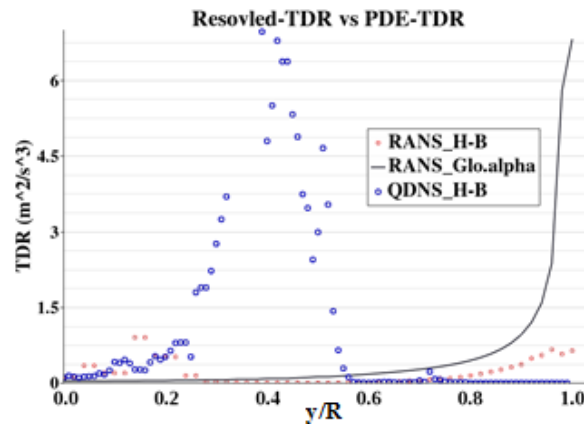


Figure 10. Comparison between the results of RANS and QDNS simulations.

Shear Modification in Small scales of Turbulent Flow

FIU investigated the possibility of obtaining a correction algorithm for shear rate in RANS simulations. The approach was to extract data related to shear rates in dissipative cells from high fidelity RANS simulation (RANS-alpha) and a QDNS simulation in Star-CCM+. FIU was interested in the similarity between RANS-based and QDNS-based extracted data. Later, the extracted data was analyzed in order to find an expression that could be implemented in RANS simulations in order to improve accuracy of the RANS modeling using the original HB method.

It was previously shown that the RANS-alpha method was capable of accurately predicting axial velocity profile for all flow regimes. Further, FIU extended its evaluation to turbulent quantities, such as normalized rms and mean of axial velocity. FIU measured u_{rms}^+ -versus-wall distance, and U^+ -versus- Y^+ to ensure acceptability of the results. Figure 11 shows that qualitative similarities exist between reported results and turbulent profiles of a turbulent pipe flow in the literature. Additionally, Figure 11 shows similarities between profiles of TKE versus r/R and U^+ versus Y^+ respectively, as generated by FIU and Eggeles, 1994.

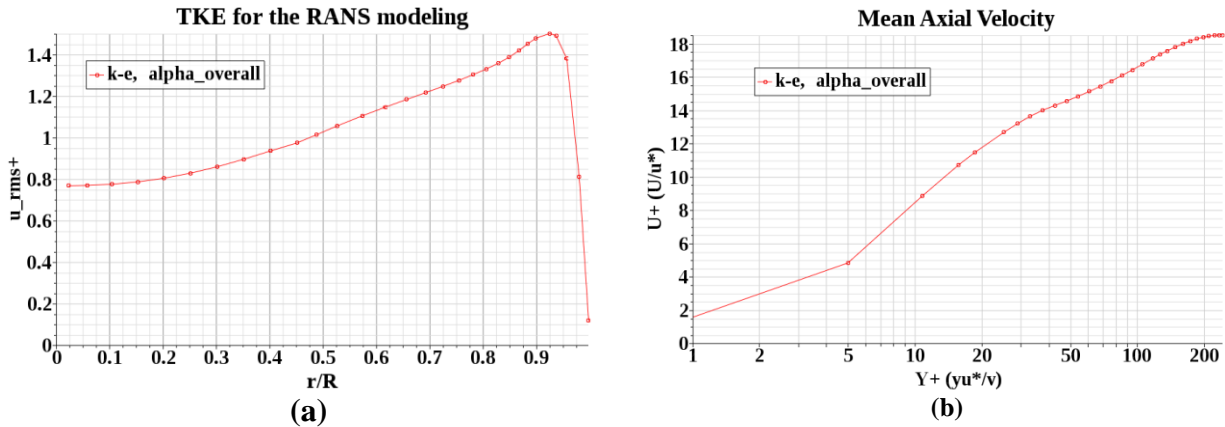


Figure 11. Turbulent profiles obtained from the RANS modeling with 7328 cells

With validations obtained for RANS-alpha modeling for $Re = 25,300$, it was possible to investigate the variation of shear rate with length and velocity scales. First, the variation of turbulent kinetic energy versus shear rate was plotted for $Re = 25,300$. This variation, as shown in Figure 12(a), agreed with variations reported by Peltier et al. (2015). This verification was also obtained for flows with lower Reynolds numbers, $Re = 20,000$, $15,000$, and $10,000$, as can be seen in Figure 12(a). These results are insensitive to grid resolution and are for domains consisting of 7328 cells. Results of the grid independency tests are available in Appendix C of this report. Later, FIU focused on expressions reported by Peltier et al. (2015) and similarly by Tennekes (1968), which links the velocity scale (u') and length scale (η) to shear rate in the dissipative scales, i.e., shear rate $\propto u'^2/\eta$. In this expression, η is the Kolmogorov length and $\eta = (\nu^3/\epsilon)^{1/4}$, where ν and ϵ are the kinematic viscosity and the turbulent dissipation rate, respectively. Results of this analysis are shown in Figure 12(b). An important fact is that results in both Figure 12(a) and Figure 12(b) indicate similarities in profiles for different Reynolds numbers. In addition, it is observed that the maximum of shear rate and maximum of u_{rms}/η are very close in each profile (for $Re = 10,000$, maximum of the shear rate and maximum of u_{rms}/η are 725.6 1/s and 734.5 1/s, respectively).

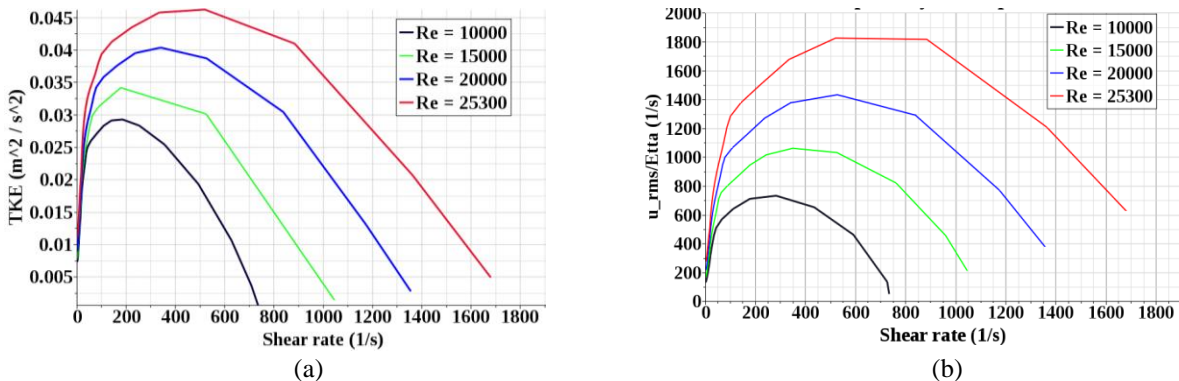


Figure 12. Variation of turbulent quantities at various Reynolds numbers. On the left: TKE-shear rate (in accord with Peltier et al. (2015)). On the right: shear dependency in dissipative scales.

A similar shear dependency analysis was performed for a QDNS simulation with $Re = 25,300$. Figure 14 shows that the profile of the QDNS is more flat as compared to the RANS simulation and the maximums on the vertical and axial axis are not close (maximum of the u_{rms}/η is 384 1/s,

while maximum of shear rate is 1575 1/s). In addition, both the maximum of shear rate and u_{rms}/η are smaller in the QDNS simulation compared to the RANS modeling. These discrepancies are likely related to the incompatibility of the SEM with the periodicity condition. As a second remedy, a shorter domain and a significantly courser computational grid was considered. For this purpose, the smallest grid cell size was magnified to four times the size of the Kolmogorov length scale ($4*\eta$), as recommended by Moin et al. (1998).

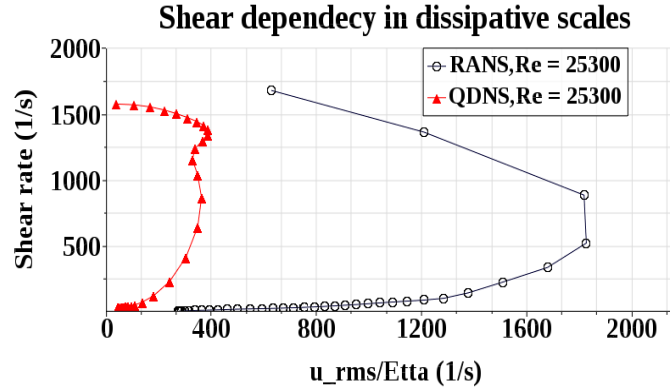


Figure 13. Comparison of shear dependency in QDNS-HB and RANS-alpha.

Q-DNS Simulations Using 3-D inlet Velocity Constructed from 2-D Experimental Data

The grid size for the Q-DNS simulation was revised based on guidelines from the selection of the smallest grid spacing by Moin et al. (1996). A value between three and four times the Kolmogorov length scale, i.e., $4*\eta < \text{maximum}(\Delta x, \Delta y, \Delta z) < 3*\eta$ was selected for mesh creation. This resulted in a total number of cell elements between $(1/64)*Re^{9/4}$ and $(1/27)*Re^{9/4}$, where $Re = \rho u^* D / \mu_w = 1160$ based on $\mu_w = 0.00802$ and $u^* = 0.1$. The resulting grid consisted of 454,000 cells. Size reduction was very important since full capture of the entire length scales of turbulence in a cube of size D^3 (m^3) required $Re^{9/4}$ (= approximately 7.85 million) cells in a very small computational domain. After grid resizing, modification to the inlet velocity profile was a crucial. The rotation matrix displayed by Eq.(7) was used to create a 3-D inlet profile based on the 2-D experimental profile obtained by Escudier et al. (1996). Figure 14 and Figure 15 show the inlet boundary condition before and after imposing the SEM on left and right, respectively. For the SEM, the turbulent intensity and length scales were set to 6 % and 0.038d.

$$R_z(\theta) = \begin{bmatrix} \cos \theta & -\sin \theta & 0 \\ \sin \theta & \cos \theta & 0 \\ 0 & 0 & 1 \end{bmatrix} \quad (7)$$

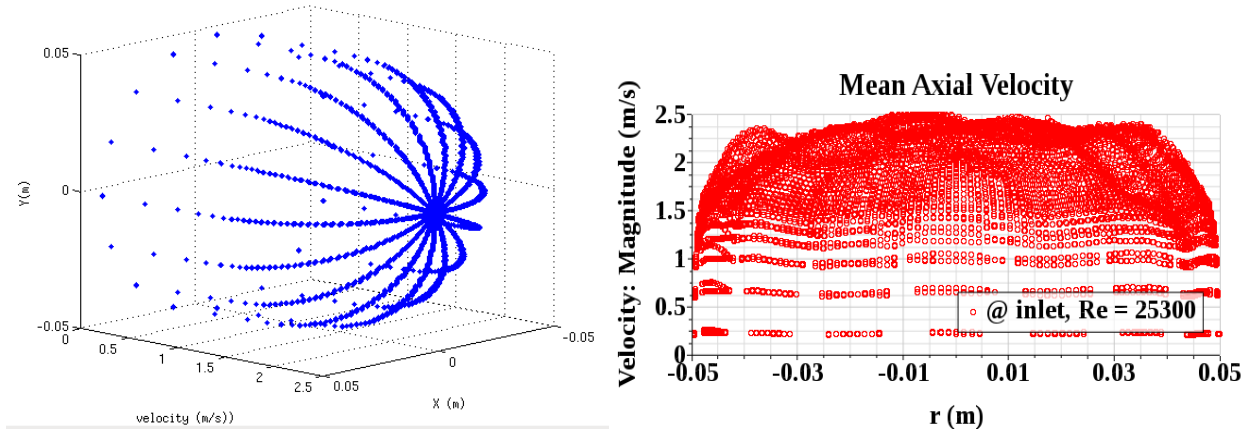


Figure 14. 3-D inlet velocity B.C., On left: profile constructed in Matlab. On right: Profile after SEM application in Star-CCM+.

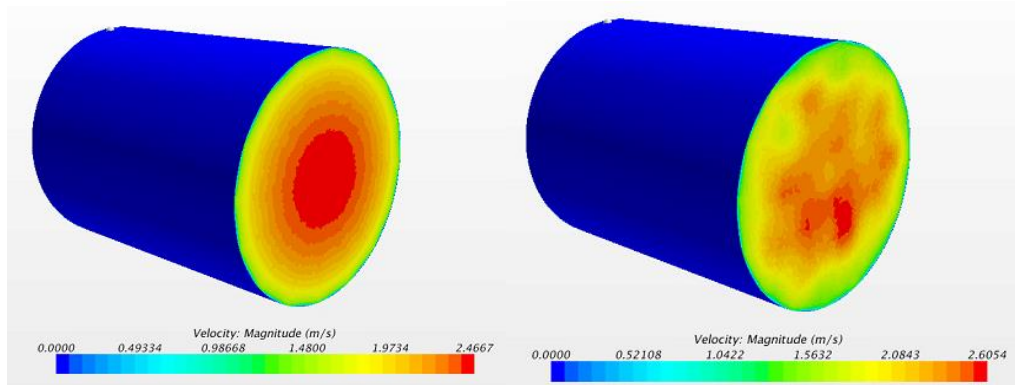


Figure 15. Inlet velocity B.C., On left: No SEM applied, On right: SEM applied.

Q-DNS simulation of flow using the modified inlet profile was performed and velocity was collected at 28 stations as shown in Figure 16. The reason for creating this many points was that Star-CCM+ does not allow for recording of time history over a line probe. Additionally, the time history of velocity at enough points was needed for statistical analysis and investigating the power spectral density of turbulent kinetic energy.

The time history and volume averaged values of viscosity ($\mu_{avg} = \sum \mu_i / N_{cells}$) was recorded during the simulation for approximately three physical seconds. Figure 17 shows the steady mean values for axial velocity at 28 stations and averaged viscosity for the entire domain. The steady mean values assured that the time period for averaging was correctly selected. Mean values of velocity at 28 points was plotted verses position for the purpose of comparison with the experimental data, as shown in Figure 18. Deviation from the experimental data is about 1.5% with a correct representation of a periodic domain. Figure 18(b) also shows the mean normalized velocity profiles obtained from the two approaches. Initially, the local viscosity values were used in creating the non-dimensional wall distance ($Y^+ = \rho u^* d / \mu_{loc}$) leading to a variation shown by the triangular symbols. This variation did not agree with typical turbulent velocity profiles. Later, the method of Wilson and Thomas (1987) was used to construct the non-dimensional wall distance ($Y^+ = \rho u^* d / \mu_{wall}$) based on the viscosity value at the wall. Effect of this modification is shown with the red line in Figure 18(b), which provides a correct profile for a turbulent flow.

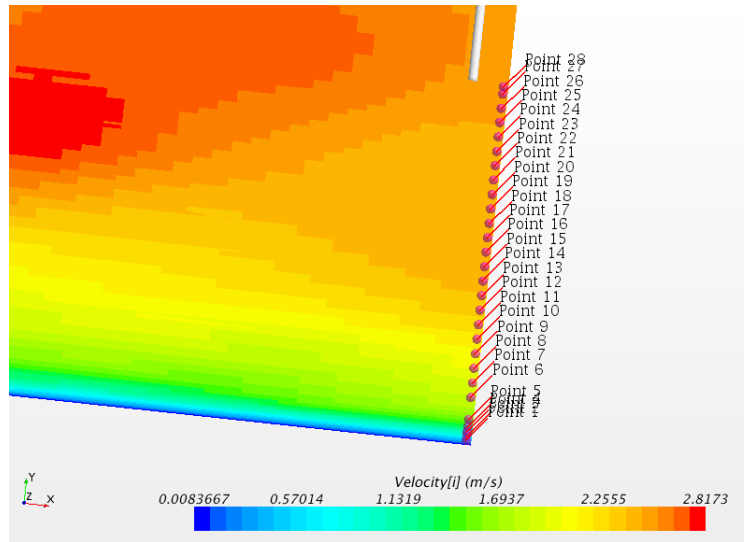


Figure 16. Measurement locations at the outlet of the computational domain.

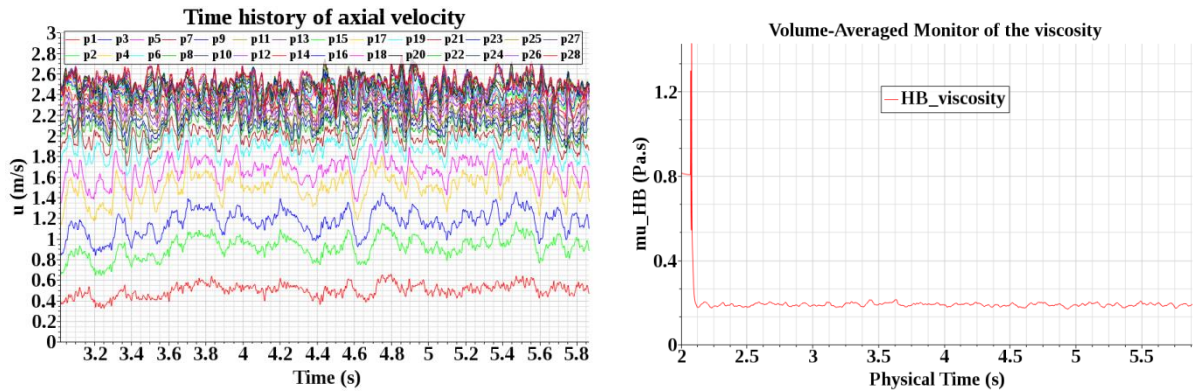


Figure 17. Time history of velocity at 28 points (on left) and volume averaged viscosity (on right).

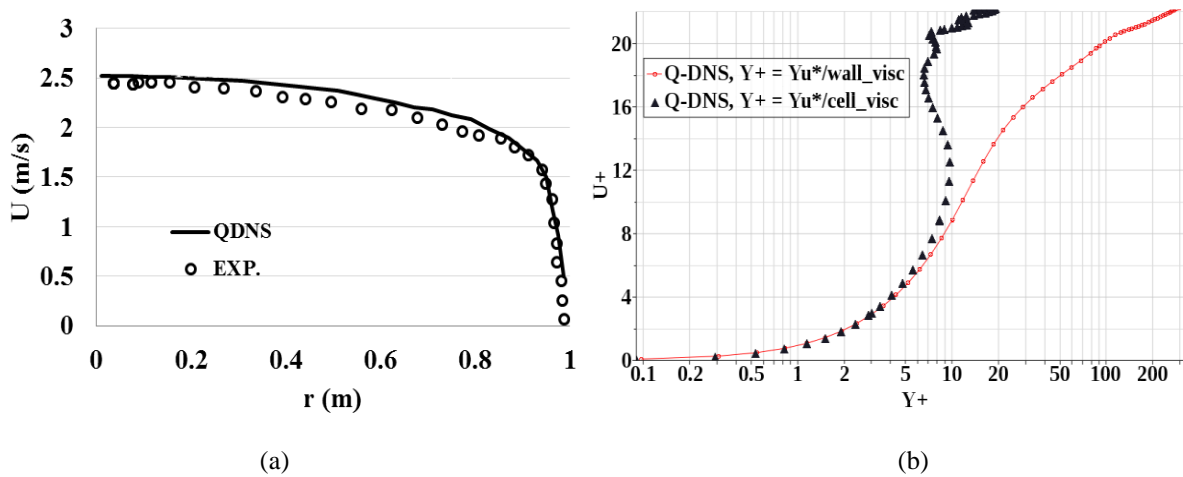


Figure 18. Axial velocity non-dimensional velocity against non-dimensional wall distance.

Further, FIU obtained rms values of the axial velocity for Q-DNS simulations (Figure 11(a)). Results are shown with the red curve for QDNS in Figure 19(a). This result agrees with typical profiles of rms velocity for turbulent flows and the variation is similar to RANS, shown by the dotted line. However, the profile of QDNS is more flat compared to that of RANS and significant deviation is observed between profiles in regions away from the wall and in the core flow region. The lower level of energy close to the wall, as shown by the lower peak, and away from the wall, indicates a higher dissipation rate of turbulent kinetic energy.

Shear dependency analysis was performed on the most recent QDNS results and comparison was conducted between the QDNS and the RANS-alpha method, as shown in Figure 19(b). Results indicate a better similarity to the RANS's results compared to results shown in Figure 13. In fact, using a more realistic profile, instead of a uniform plug profile at the inlet, resulted in attaining the maximum of u_{rms}/η . However, discrepancies still exist which can be related to use of first order gradients for calculation of the Kolmogorov length scale. Here, the lower shear stress for the QDNS profile is in accordance with the lower energy level that was discussed above for Figure 19(a).

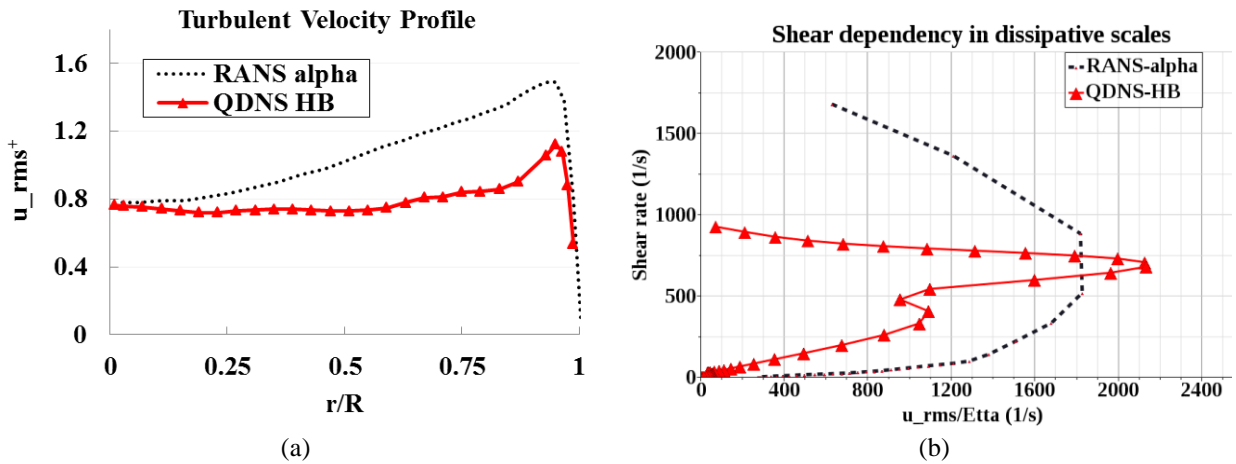


Figure 19. Turbulent velocity and shear dependency for Q-DNS as compared to the RANS.

Calculation of Energy Spectra

The capability of Star-CCM+ in generating a power spectrum of TKE was assessed in QDNS simulations. Power spectral density (PSD) was intended for separation of dissipative eddies from inertia and energy containing eddies. The expressions for PSD of the velocity fluctuations are shown in Eq. (8).

$$\text{PSD}(\omega) = \frac{1}{2\pi} \int_{-\infty}^{\infty} e^{-i\omega\tau} R_{ii}(\tau) d\tau \quad (8)$$

where, R_{ii} is the autocorrelation function, defined as: $R_{ii} = u(t).u(t+\tau) + v(t).v(t+\tau) + w(t).w(t+\tau)$, and u , v , and w are fluctuating components of the velocity field. In order to access FFT of the results in both frequency and space domains, FIU installed the latest version of Star-CCM+ on FIU-HPC. FFT analysis of results shown in Figure 17 was performed using time FFT modules available in Star-CCM+. In addition, similar analysis was performed using a Matlab script that was developed based on Davidson's code¹ (developed code is available in Appendix D of this

¹ http://www.tfd.chalmers.se/~lada/comp_turb_model/assignment_2/task2_MTF270_intro.pdf

report). This program was tested for DNS results in the literature and results of the implementation of this code agreed with typical profile of spectra for turbulent flows, according to Sakai et al. (2011) and Verstappen et al. (2014).

Power spectra calculated in Star-CCM+ at four points at the outlet of the domain (see Figure 16) are shown in Figure 20. The results show the spectra are more powerful in very low frequencies for locations at the boundary and are more powerful in higher frequencies as points depart from the solid boundary. However, the results do not show all three ranges of scales, which are energy containing, inertia, and dissipative ranges. For this reason, the results of the calculation in Star-CCM+ did not agree with typical spectra for turbulent flows.

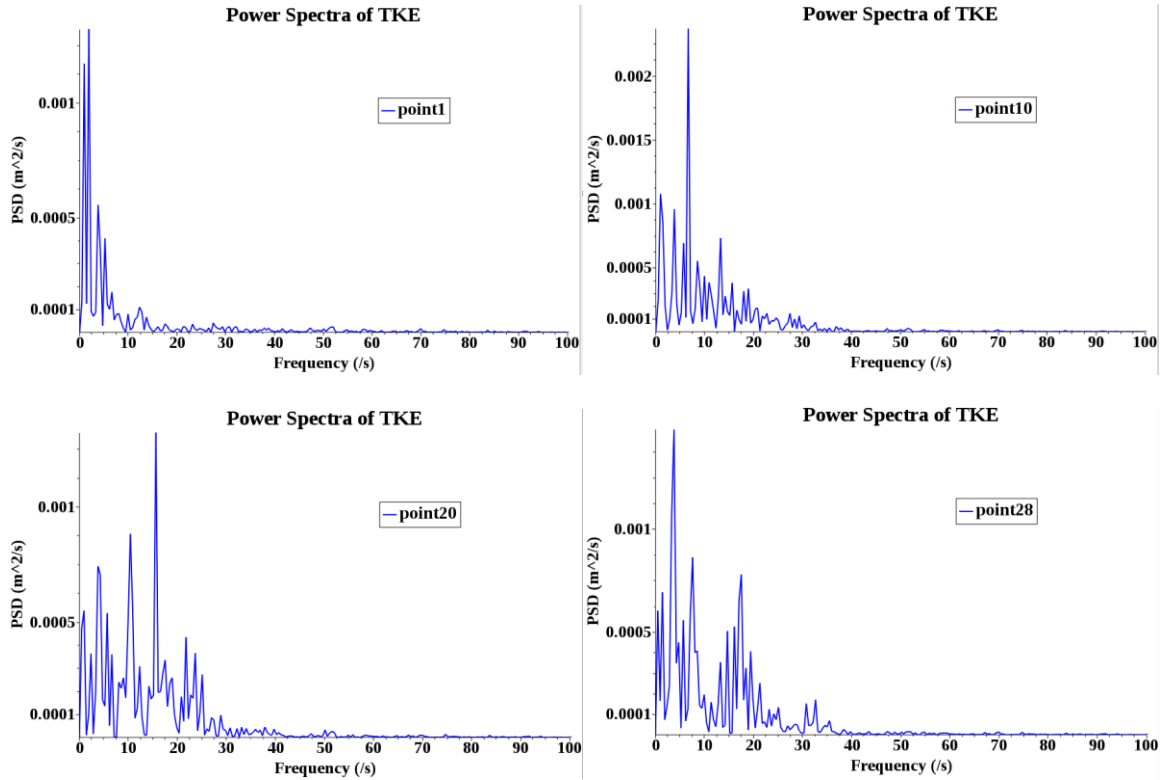


Figure 20. PSD of axial velocity (u) obtained using Matlab for QDNS simulation.

A second set of results obtained from implementing a Matlab script is shown in Figure 21. For this analysis, FIU obtained PSD at more points of the outlet (see Figure 16) to observe similarities at various locations. Results for this analysis are shown in Figure 21. All spectra in Figure 21 agrees with typical spectra for turbulent flows. In each diagram, the red line shows decay of energy with a power of $-5/3$, which is related to the inertial eddies. For all locations, the spectrum in the inertia range agrees well with the $-3/5$ slope, which indicates enough sampling points and capture of fluctuations. However, the spectra show oscillations in the fast decaying ranges where dissipation of the energy occurs. Additional investigations on other key parameters, such as turbulent specification at the inlet at this point is necessary (Arnett et al., 2011).

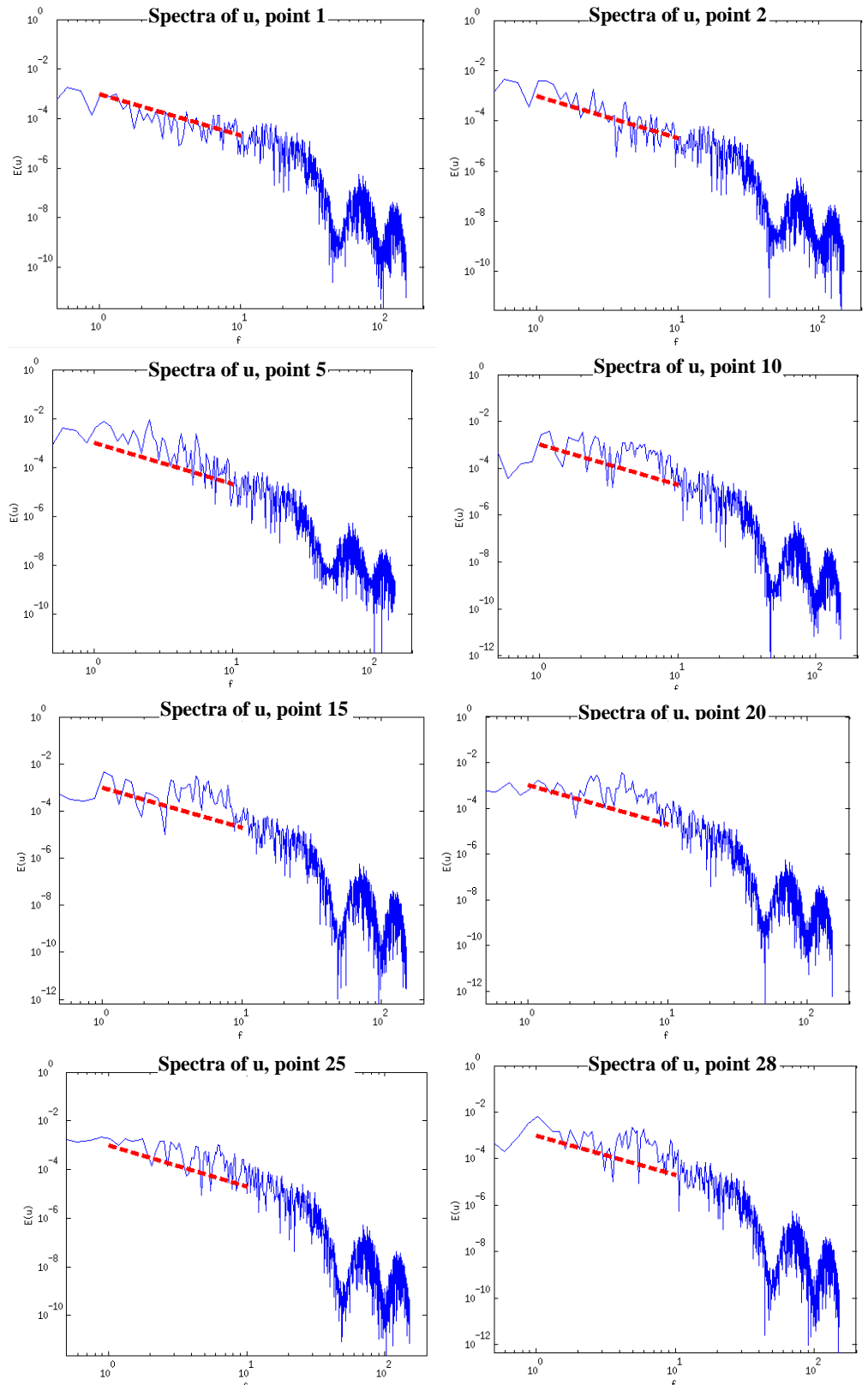


Figure 21. PSD of axial velocity (u) obtained in Star-CCM+ for QDNS simulations.

CONCLUSIONS

CFD simulations of the pipe flow of Bingham fluid were conducted using Star-CCM+. The velocity profiles were compared between the simulation results and experimental data. A proposed viscosity modification model, namely the alpha model, proved to significantly improve accuracy of the Herschel-Bulkley model for flow in laminar, transitional, and turbulent regimes. The alpha model was more accurate than another modification model proposed in the literature (SRC) for all three regimes of flow considered. The alpha model also competed well with the model used by Peltier et al. (2015). All turbulence profiles of the alpha model agree well with typical profiles for turbulent flows. In best cases, improvement of error through use of the alpha method was 42 %, 48%, 61.4% for laminar, transient, and turbulent cases, respectively.

QDNS simulations of the flow in the fully turbulent regime were performed using uniform and modified velocity profiles. It was shown that utilization of the uniform velocity profile, or bulk velocity at inlet, could not yield accurate results, since the domain could not be set to periodic due to a conflict between periodicity and turbulence specification at the inlet. Using a 3-D inlet profile constructed from a 2-D experimental profile along with SEM as the turbulence specification model at the inlet provided accurate results at the outlet of the computational domain. Profiles of turbulent quantities, U^+ and u_{rms}^+ , showed good agreement with typical profiles of these quantities for turbulent flows. Spectra of energy for QDNS simulations was also obtained at different points at the outlet of the computational domain. Analysis showed that built-in modules in Star-CCM+ could not provide correct spectra, although modified codes for spectra calculations can produce spectra that agree well with typical spectra profiles for turbulent flows. This indicated the necessity for using user defined functions in Star-CCM+ for the calculation of spectra and separation of dissipative scales.

After accurate results were obtained with the RANS simulations, dependency of the shear rate to length and velocity scales of turbulence was investigated over a range of Reynolds numbers. Similar dependencies were observed for different Reynolds numbers where the maximum of the shear rate and u_{rms}/η quantities converged to one value for each Reynolds number. This dependency was obtained in the QDNS simulation of flow with $Re = 25300$. Dependency in QDNS was qualitatively similar to the RANS dependency profile but quantitative similarity was not obtained. Quantitative comparison was improved using the modified 3-D inlet velocity. Lower shear stress that was observed for QDNS the dependency profile was linked to lower levels of kinetic energy in QDNS. This fact was obtained by comparing rms values of the axial velocity between the RANS alpha and QDNS HB simulations, which indicated higher dissipation occurring in the QDNS simulation. Additional investigations on boundary conditions and different Reynolds numbers is necessary to understand the differences between the RANS alpha and QDNS HB models and to obtain a modification for the shear rate that can be implemented in the RANS HB model.

In future efforts, QDNS simulations of the pipe flow using the 3D profiles will be conducted for various Reynolds numbers. More precise calculation of the turbulent quantities (TKE and TDR) will be performed using higher order gradients using fluctuation components of the velocity field. The spectral analysis of the turbulence energy and dissipation rate will be calculated to perform scales separation during simulation of flow. Similar shear dependency will be

investigated and results will be compared to the analysis that was performed using the RANS alpha method.

REFERENCES

1. Andrade L.C.F., Petronílio J.A., de A. Maneschy C.E., de A. Cruz D.O., 2007, The Carreau-Yasuda Fluids: a Skin Friction Equation for Turbulent Flow in Pipes and Kolmogorov Dissipative Scales, *Journal of the Brazilian Society of Mechanical Science and Engineering*, Vol. 29, Issue 2, p163
2. Bartosik A., 2010, Application of Rheological Models in Prediction of Turbulent Slurry Flow, *Flow Turbulence, and Combustion*, Volume 84, pp 277–293
3. Escudier M.P., Presti F., 1996, Pipe Flow of a Thixotropic Liquid, *J. Non-Newtonian Fluid Mech.*, volume 62, PP. 291-306
4. Herschel W.H., Bulkley R., 1926, *Kolloid-Zeitschrift*, Volume 39, Issue 4, pp 291–300, doi:10.1007/BF01432034
5. Gavrilov A.A., Rudyak V.Y., 2014, A Model of Averaged Molecular Viscosity for Turbulent Flow of Non-Newtonian Fluids, *Journal of Siberian Federal University, Journal of Mathematics & Physics*, Voulem 7, Issue 1, pp 46–57
6. Moin P., Mahesh K., *Direct Numerical Simulation: A Tool In Turbulence Research*, 1998, *Annual Review Fluid Mechanics* 1998. 30:539–78
7. Peltier J, Andri R, Rosendall, Inkson N., Lo S., 2015, Evaluation of RANS Modeling of Non-Newtonian Bingham Fluids in the Turbulence Regime Using STAR-CCM+®, *Advanced Simulation & Analysis*, BechtelNuclear, Security & Environmental, Cd-adapco, Conference: STAR Global Conference 2015
8. Sakai Y., Nagata Kouji, Suzuki H., Relationships between Large-Scale Coherent Motions and Bursting Events in a Turbulent Boundary Layer, "Wind Tunnels and Experimental Fluid Dynamics Research", chapter 24, ISBN 978-953-307-623-2, Published: July 27, 2011 under CC BY-NC-SA 3.0 license. DOI: 10.5772/17578
9. Shams A., Roelofs F., Komen E.M.J., Baglietto E., 2012, Optimization of a pebble bed configuration for quasi-direct numerical simulation, *Nuclear Engineering and Design*, Volume 242, Page 331– 340
10. Soto R.J., Shah V.L., 1976, Entrance Flow of a Yield-Power Law Fluid, *Journal of Applied Science Research*, Volume 32
11. Tennekes H., 1968, "Simple Model for the Small-Scale Structure of Turbulence, *Phys. Fluids*, 11 (33), 669-671'
12. Toms B.A., 1948, Some Observations on the Flow of Linear Polymer Solution through Straight Tubes at Large Reynolds Number, *Proceedings of 1st Conference on Rheology*, Vol.2, North Holland, Amsterdam, p135.
13. Verstappen R.W.C.P. Rozema W., Bae H.J., Numerical scale separation in large-eddy imulation, Center for Turbulence Research, *Proceedings of the Summer Program 2014*
14. Wilson, K.C., Thomas A.D., 1985, A New Analysis of the Turbulent Flow of Non-Newtonian Fluids, *The Canadian Journal of Chemical Engineering*, Volume 63

APPENDIX A: GRID-INDEPENDENCE TEST FOR VARIOUS RANS SIMULATIONS

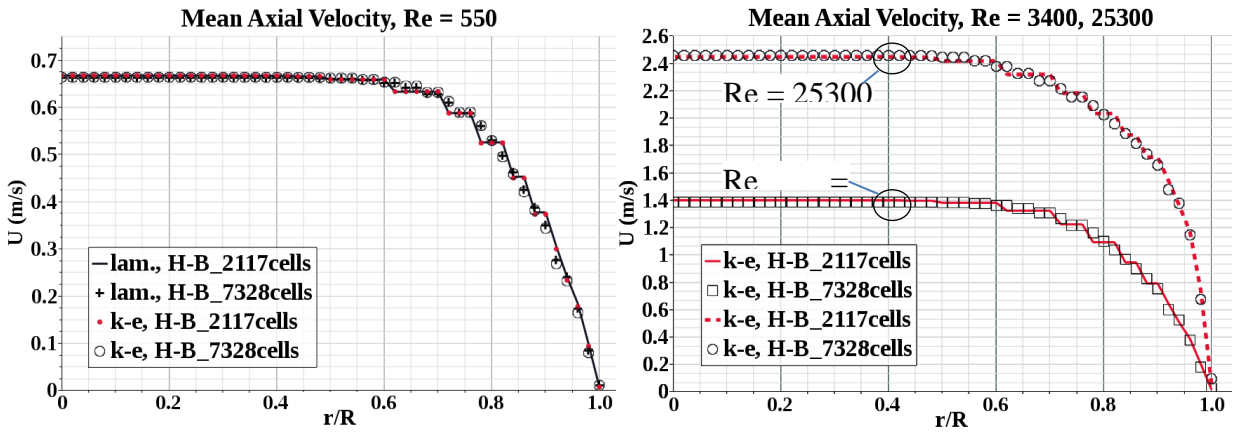


Figure A-1. Test of grid independency of simulation results for HB method.

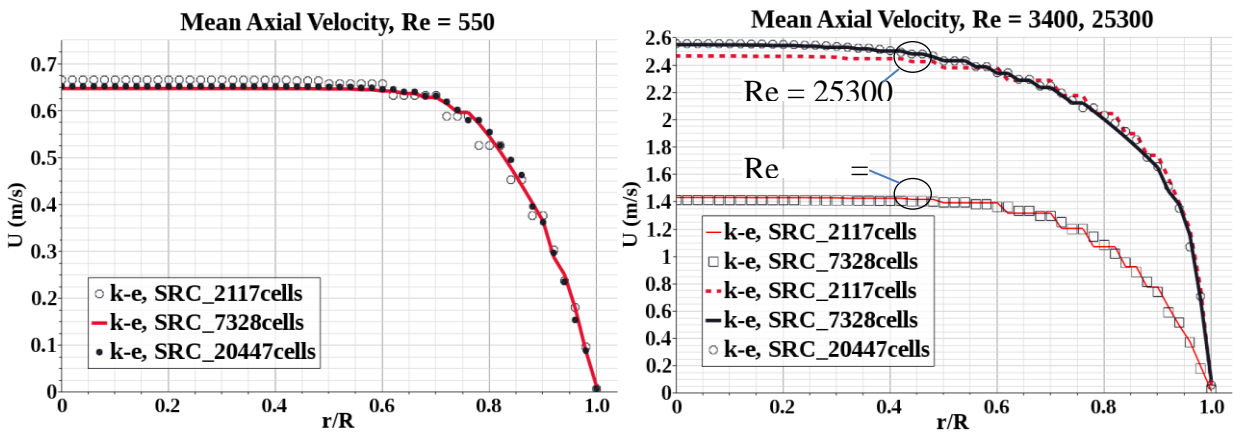


Figure A-2. Test of grid independency of simulation results for SRC method

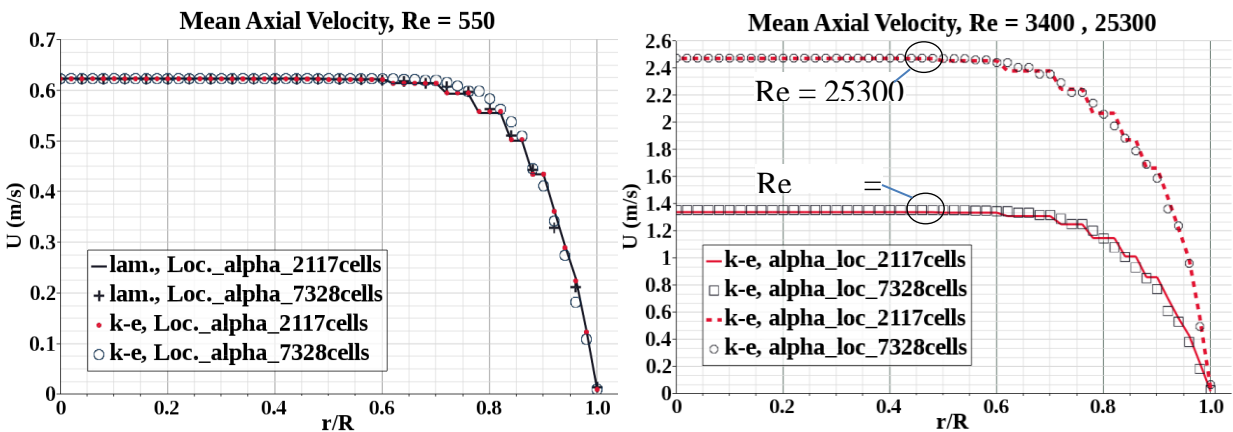


Figure A-3. Test of grid independency of simulation results for local-alpha method.

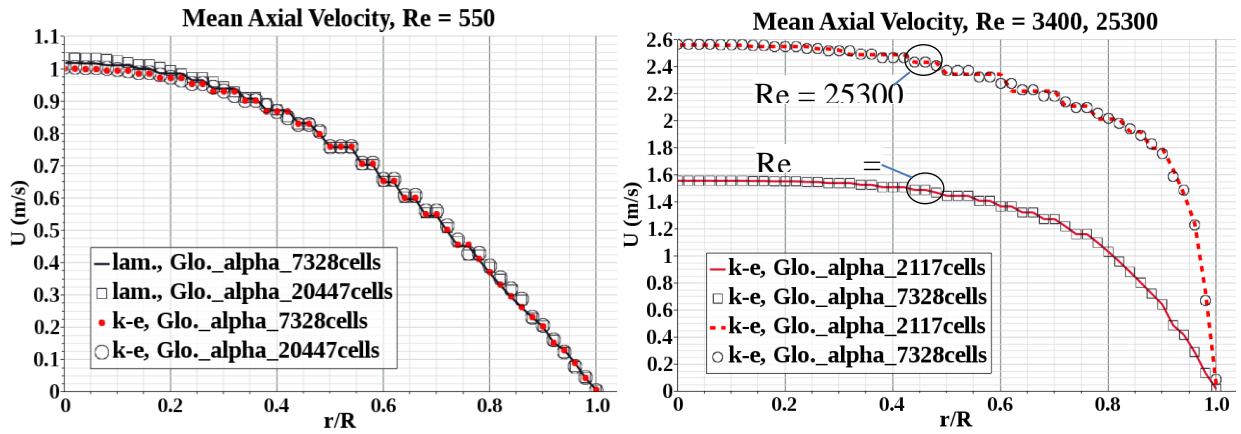


Figure A-4. Test of grid independency of simulation results for global-alpha method.

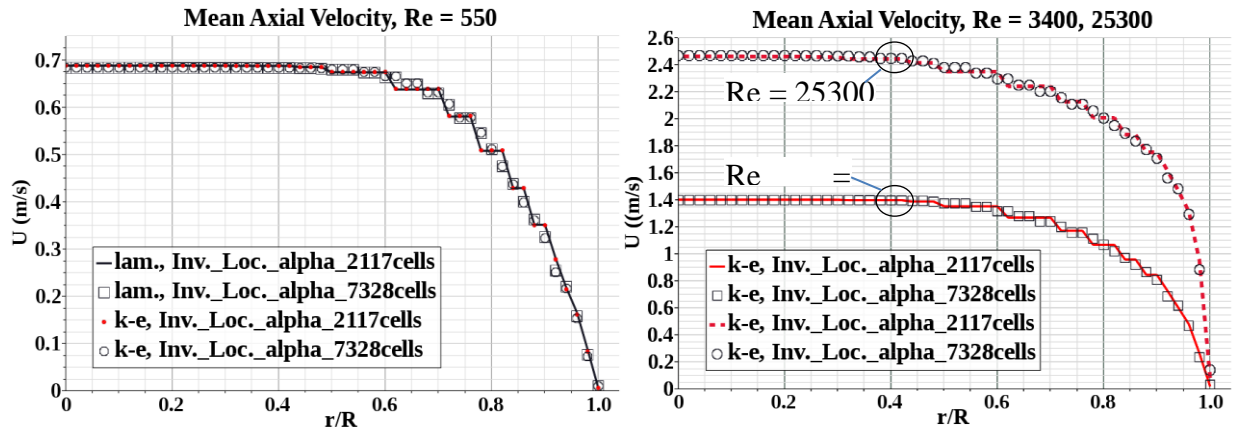


Figure A-5. Test of grid independency of simulation results for local-alpha method.

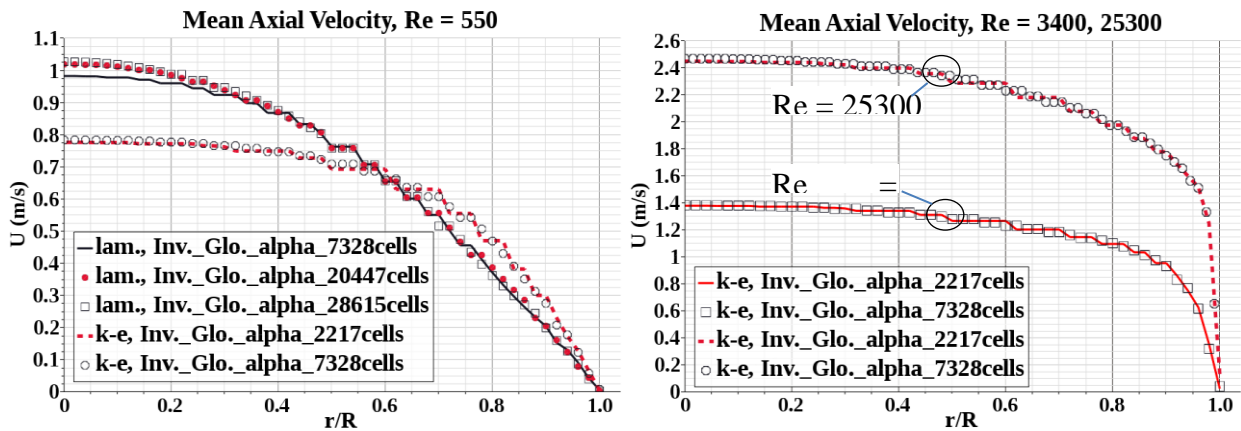


Figure A-6. Test of grid independency of simulation results for Inverse global-alpha method.

APPENDIX B: COMPUTATION OF TURBULENT QUANTITIES

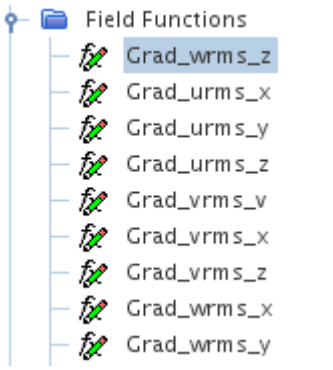
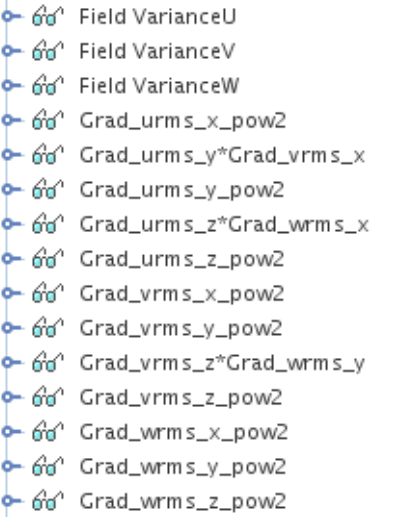
Turbulent kinetic energy (TKE)

Formulation:	Code:
$TKE = K = \frac{1}{2} (\overline{u^2} + \overline{v^2} + \overline{w^2}) = \frac{1}{2} (u_{rms}^2 + v_{rms}^2 + w_{rms}^2)$	$TKE = 0.5 * (pow(\{user_rms_u\}, 2) + pow(\{user_rms_v\}, 2) + pow(\{user_rms_w\}, 2))$

Turbulent dissipation energy (TDR)

Formulation:	Code:
$TDR = \nu \left\{ 2 \left[\left(\frac{\partial u_i}{\partial x_i} \right)^2 + \left(\frac{\partial u_j}{\partial x_j} \right)^2 + \left(\frac{\partial u_k}{\partial x_k} \right)^2 \right] + \left(\frac{\partial u_i}{\partial x_j} \right)^2 + \left(\frac{\partial u_j}{\partial x_i} \right)^2 + \left(\frac{\partial u_i}{\partial x_k} \right)^2 + \left(\frac{\partial u_k}{\partial x_i} \right)^2 + \left(\frac{\partial u_j}{\partial x_k} \right)^2 + \left(\frac{\partial u_k}{\partial x_j} \right)^2 + 2 \left(\frac{\partial u_i}{\partial x_j} \cdot \frac{\partial u_j}{\partial x_i} + \frac{\partial u_i}{\partial x_k} \cdot \frac{\partial u_k}{\partial x_i} + \frac{\partial u_j}{\partial x_k} \cdot \frac{\partial u_k}{\partial x_j} \right) \right\}$	$TDR = \{DynamicViscosity\} * (2 * (\{Grad_urms_x_pow2Monitor\} + \{Grad_vrms_y_pow2Monitor\} + \{Grad_vrms_z_pow2Monitor\}) + (\{Grad_urms_y_pow2Monitor\} + \{Grad_urms_z_pow2Monitor\} + \{Grad_vrms_x_pow2Monitor\} + \{Grad_vrms_z_pow2Monitor\} + \{Grad_vrms_x_pow2Monitor\} + \{Grad_vrms_y_pow2Monitor\}) + 2 * (\{Grad_urms_y * Grad_vrms_xMonitor\} + \{Grad_urms_z * Grad_vrms_xMonitor\} + \{Grad_vrms_z * Grad_vrms_yMonitor\}))$

Tools Used to Obtain Different Variables Used in Calculation of TKE and TDR

<i>The rms values of velocity filed components</i>	<i>The filed functions and monitors for variance of the parameters</i>	
<pre>user_rms_u = sqrt(abs(\{FieldVarianceUMonitor\})) user_rms_v = sqrt(abs(\{FieldVarianceVMonitor\})) user_rms_w = sqrt(abs(\{FieldVarianceWMonitor\}))</pre>		

APPENDIX C: GRID-INDEPENDENCE TEST FOR MEAN VELOCITY AND TKE-SHEAR RATE ANALYSIS

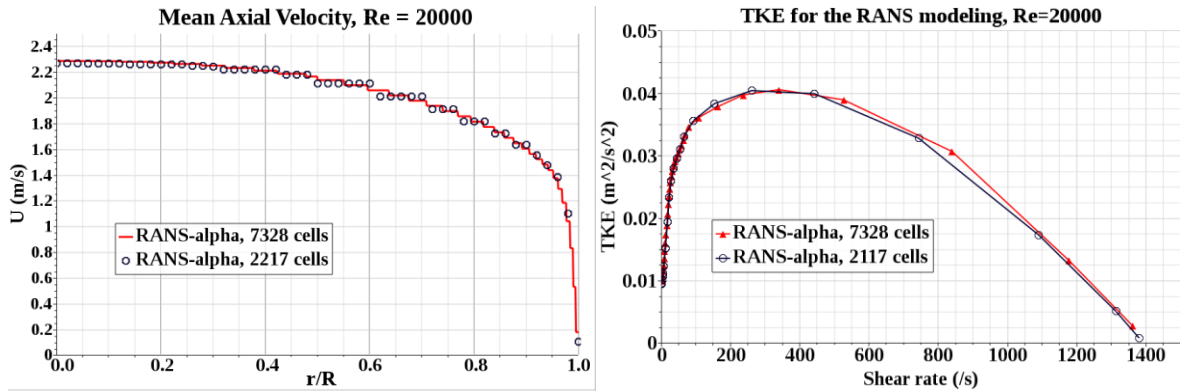


Figure C-1. Test of grid independency for alpha-RANS simulations, Re = 20000.

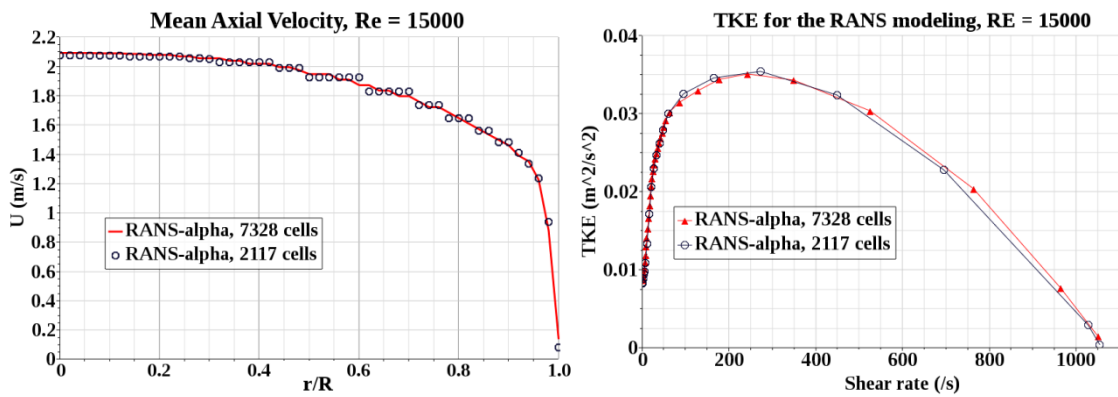


Figure C-2. Test of grid independency for alpha-RANS simulations, Re 15000.

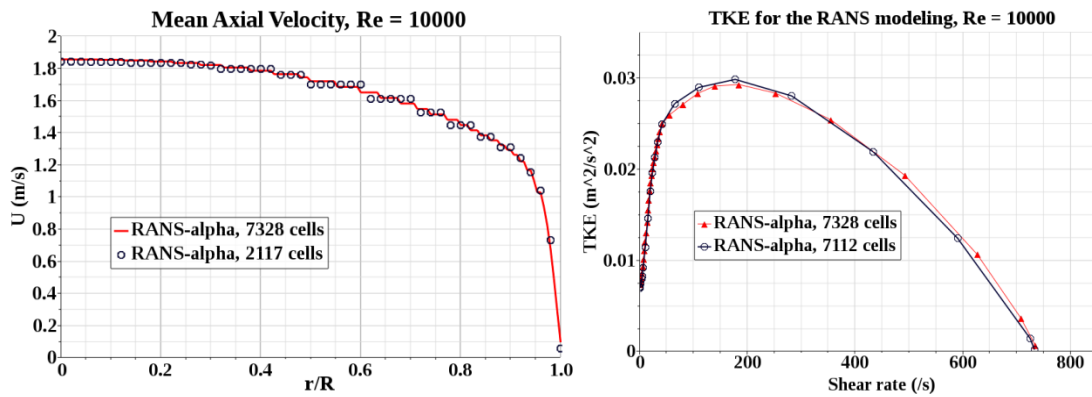


Figure C-3. Test of grid independency for alpha-RANS simulations, Re 10000.

APPENDIX D: MATLAB CODE FOR POWER SPECTRA ENERGY (PSD)

<pre> close all % clear all % ***** read u % time step=0.0033 dt=0.0033; n=length(u1); % compute time array t=dt:dt:n*dt; indicator = 4; u_vect = eval(sprintf('u%d',indicator)); % % u_vect =current_array_acc_CFB_rpm_630(1:5000,5); u_vect_mean = mean(u_vect); u_vect_fluc = u_vect-u_vect_mean; %umean=mean(u3); % subtract the mean % u3=u3-umean; u_vect_fluc = u_vect-u_vect_mean; % number of points in the fft nmax=1024; % compute RMS n=length(u_vect); u_vect_rms=0; for i=1:n u_vect_rms=u_vect_rms+u_vect(i)^2/n; end u_vect_rms=u_vect_rms^0.5; </pre>	<pre> % time step (gives the right freq. on the x-axis) dt=0.0033; [px,f]=pwelch(u_vect_fluc,nmax,[],[],1/dt); plot(f,px) hold % add line with -5/3 slope x=[1 10]; ynoll=1; y(1)=ynoll; y(2)=y(1)*(x(2)/x(1))^(5/3); plot(x,y,'r--','linewidth',4) axis([0.5 200 1e-7 1]) title('spectrum of u','fontsize',20) xlabel('f','fontsize',20) ylabel('E(u)','fontsize',20) handle=gca; set(handle,'yscale','log','xscale','log') % set(h,'xscale','log') set(handle,'fontsi',[20]) print u_spectrum.ps -deps % </pre>
--	--

TASK 17.1.2

CFD VALIDATION OF JET IMPINGEMENT CORRELATIONS TANKS (FIU YEAR 6)

EXECUTIVE SUMMARY

Many engineering processes at various U.S. Department of Energy sites include the flow of nuclear waste in a liquid form that is characterized as a Bingham plastic material, a form of non-Newtonian fluid. Solid particles of varying range are suspended in the radioactive waste during mixing operations using pulse-jet mixers (PJMs). The existence of such particles makes it difficult to predict and evaluate the PJM performance.

One of the critical characteristics to be understood in the PJM process in order to predict the non-Newtonian fluid behavior are the radial jets created by the PJMs. The analytical work currently used to describe the radial wall jets produced in the PJMs uses the paper, "Investigation of a turbulent radial wall jet," (Poreh et al., 1967) that studied the radial wall jets produced from impingement of turbulent round jets. Based on their detailed experiments, Poreh et al. proposed correlations for maximum jet velocity and radial wall jet thickness. The correlations are based on a non-dimensional number that takes into account the ratio of the initial jet diameter and the distance from the nozzle to the impingement surface. There has been skepticism on the use of these correlations due to the fact that the actual ratio in the PJMs is much smaller than the ratio used in the paper.

The current CFD study investigates empirical correlations developed by Poreh that establish radial variations of maximum radial jet velocity (U_m) and jet thickness (δ) of an impinging wall jet, both at "small" and "large" impingement height ratios (b/d) and at all radial locations. This study also focuses on curved impinging surface of an actual pulse-jet-mixers device, due to its practical application in mixing vessels at the Waste Treatment and Immobilization Plant. Poreh experiments investigated a ratio of $b/d = 12$ while the PJM geometry has a ratio of $b/d = 1.5$. Numerical simulations are therefore performed in 2D axisymmetric geometry with flat impinging surfaces at an impingement height ratio, $b/d = 12$ and 1.5 and also, in 3D cylindrical geometry with curved bottom surfaces at $b/d = 1.5$. In these studies, the Reynolds number which is based on jet velocity and nozzle diameter is set to 2×10^5 . At $b/d = 12$, present radial velocity profiles at all radial locations agrees with experimental data, except for a slight mismatch near wall peak velocity. In total, U_m and δ correlations demonstrate good agreement with the Poreh's correlation. Good agreement at $b/d = 1.5$, suggest applicability of Poreh's correlation for "small" impingement height ratio. In PJM geometry, radial variation of U_m and δ correlations closely follow Poreh's correlation, although numerical values slightly differ they are within the acceptable range.

Overall, current CFD data shows good agreement with experimental data and the slight discrepancies are attributed to the intrusive nature of the experimental probe or weakness of turbulence model. The current study improves the understanding on the range of the applicability of Poreh's correlations, recommending these correlations for use in practical PJM vessel design over a wider range of impingement height and Reynolds number.

INTRODUCTION

Pulse jet mixing (PJM) is one of the methods chosen by DOE to mix high-level waste (HLW) slurry prior to the vitrification process. This method involves sucking a portion of the waste in the tank into a pressurized vessel and then injecting it back into the tank in order to mix the waste using the pressurized jets. This process is repeated over a number of cycles. The primary reason for choosing PJMs for this task is that there are no mechanical moving parts and the process can be operated remotely with minimal interference required by workers (Guenther et al).

One of the critical characteristics to be understood in the PJM process in order to predict fluid behavior (non-Newtonian) are the radial jets created by the PJMs. The analytical work currently used to describe the radial wall jets produced in the PJMs utilizes information in the paper "Investigation of a turbulent radial wall jet" (Poreh et al, 1967). Poreh established an empirical relationship for local (time averaged) maximum of radial velocity, U_m , and the spreading rate wall jet or length scale, δ , referred to as jet half-width, measuring the vertical distance z at which radial velocity becomes $0.5U_m$. A schematic of the parameters are shown in Figure 22.

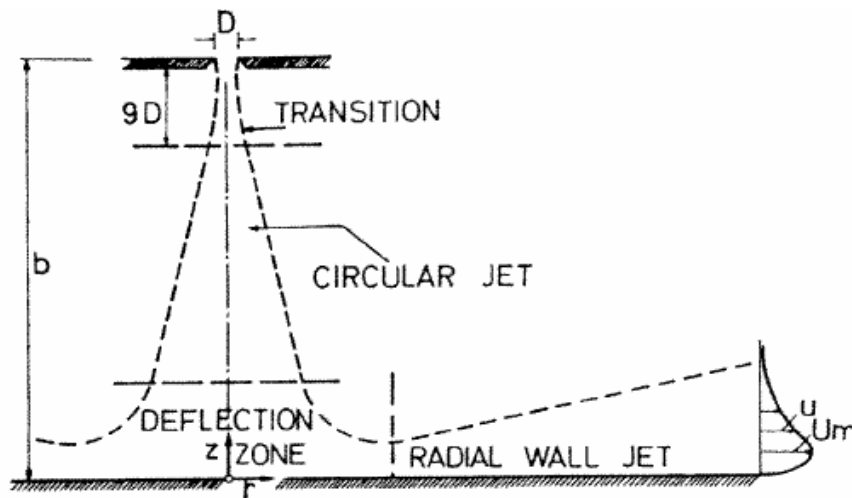


Figure 22. Schematic description of impinging and radial wall jets.

The correlations, which will be referred to as Poreh's correlations in the rest of the report, are defined as follows:

$$\text{Characteristic jet half-width, } \delta \qquad \delta/b = 0.098 * (r/b)^{0.9} \qquad (1)$$

$$\text{Maximum radial jet velocity, } U_m \qquad U_m b / \sqrt{K} = 1.32 \left(\frac{r}{b} \right)^{-1.1} \qquad (2)$$

where K is the kinematic momentum flux of the circular jet at the exit and r indicates radial locations along the wall. The measured data was gathered at a large radial distance from the impinging region over $0.75 \leq r/b \leq 2.75$ or $6 \leq r/d \leq 30$, keeping the gap ratio between the nozzle to target impinging plate, b/d , more than 8.

The controlling parameters in a PJM vessel design rely on Poreh's correlations (B. Rosendall, 2006). However, there has been skepticism on the applicability of these correlations due to the fact that the geometrical conditions in the PJM vessels were not considered in Poreh's experiment. The characteristic ratio in the PJMs is much smaller than the one tested in the paper. Poreh's experimental investigation also does not consider a curved impingement surface. The current study focuses on this issue and numerically investigates Poreh's correlations with both "small" and "high" impingement heights and at all radial locations. In particular, the current study investigates jet flows impinging on curved surface with operating conditions similar to an actual PJM device.

Florida International University in conjunction with the National Energy Technology Laboratory is carrying out CFD simulations to study the mixing performance of PJM devices. The mechanism of the mixing process is shown schematically in Figure 23, in which the mixing efficiency depends on the local radial wall jet velocity and spreading rate of the jet.

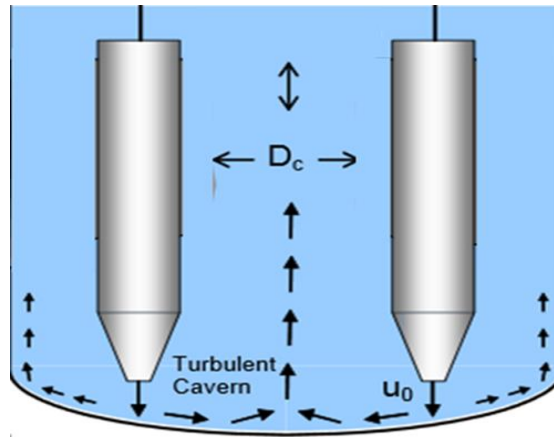


Figure 23. Schematic diagram of PJM vessel describing mechanism of flow structures that show formation of radial wall jets by normal impingement of single jets at small aspect ratio.

The major accomplishments in the present numerical work are listed below.

- A systematic validation of CFD data with those of Poreh's experimental data is performed, at a "large" b/d ratio of 12 to ensure the accuracy of the current CFD calculations (2D-axisymmetric study).
- In order to evaluate the validity of Poreh's correlations at smaller jet impingement ratios (b/d), a separate CFD study is performed in the same geometry of Poreh, but at a "small" b/d ratio of 1.5, which is of practical importance in PJM applications.
- A 3D-CFD study using a scaled down geometry of actual plant scale PJM vessel is carried out to determine the accuracy of Poreh's correlations on a curved impingement surface of a PJM vessel.

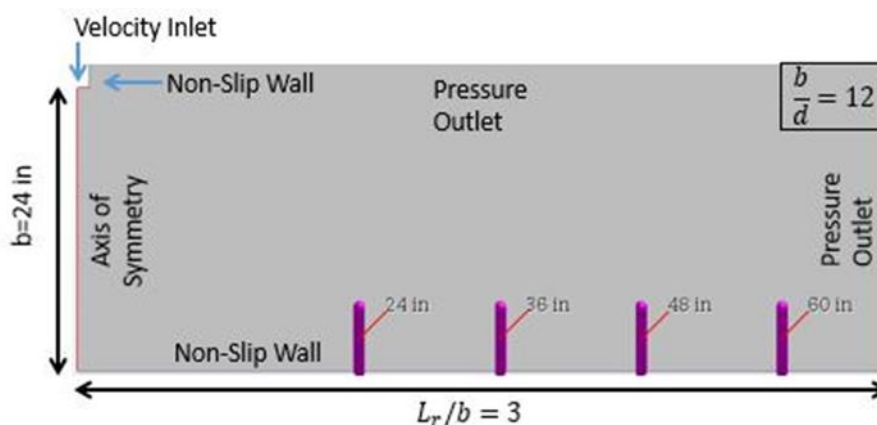
NUMERICAL DETAILS

The main focus of the current work is to study the radial wall jet that is created by impinging a circular jet on either flat or curved surfaces, and subsequently turns to form a radial wall jet away from the impingement region. Specifically, the effect of impinging gap ratio (b/d) on radial wall jet characteristics such as the self-similar radial velocity distribution (u/U_m), jet-half width and the maximum radial wall jet velocity are of primary importance. The present investigations consider two separate computational domains. First, an axisymmetric 2D geometry in which a circular jet from an orifice impinges on a flat surface to form radial wall jet in unconfined space. Second, a 3D cylindrical geometry with a curved bottom impingement surface is adopted to mimic the formation of a radial impinging jet in an actual PJM vessel device. The foregoing section will summarize detailed descriptions of geometrical configurations of computational domains, boundary conditions, CFD solver methodology, grid properties, numerical methods and turbulence modeling.

Computational details of radial wall jet on flat surface at $b/d = 12$ and 1.5

The geometrical configuration of the current test case set up of a radial wall jet on a flat surface follows the previous experimental impinging jet study conducted by Poreh (1967) and schematically shown in Figure 22. A detailed description of the experimental set up and flow parameters are documented in Poreh's paper (1967) and only the most relevant parameters are reported here. In the experimental study, an air jet was created at a velocity of $U_0 = 340 \text{ ft/s}$ from a circular orifice of diameter $d = 2 \text{ in}$ located at a fixed normal distance of $b = 2 \text{ ft}$ above a circular flat plate with a radius of 69 in. The isothermal air jet at room temperature from the orifice impinges normally on the bottom flat surface and subsequently spreads radially outward on the flat surface to form symmetrical radial jets around the impingement point. The Reynolds number based on kinematic momentum flux or the jet exit velocity was $Re = 1.96 \times 10^5$. The wall normal distribution of radial wall jet velocity profiles at various radial locations far away from the impingement region were measured and the maximum radial wall jet velocity and jet-half width were reported.

The schematic of the computational domain corresponding to the experimental radial impinging jet set up (Figure 22) is shown in Figure 24, which depicts both geometrical configurations of large and small jet to impingement plate gap ratio.



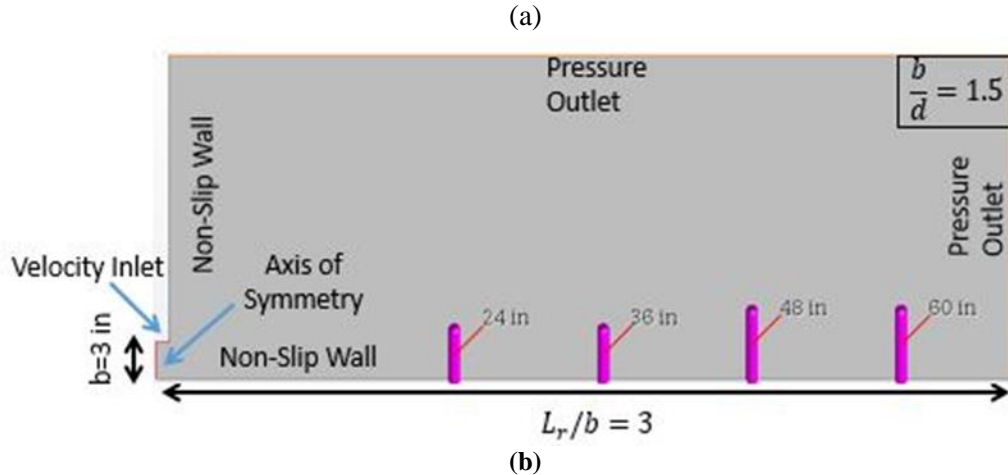
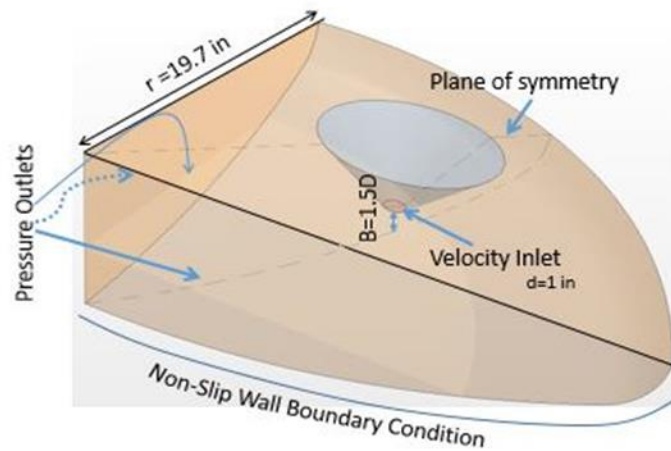


Figure 24. Computational domain of (a) large jet to impingement distance ratio of $b/d=12$ and (b) small jet to impingement distance ratio of $b/d=1.5$.

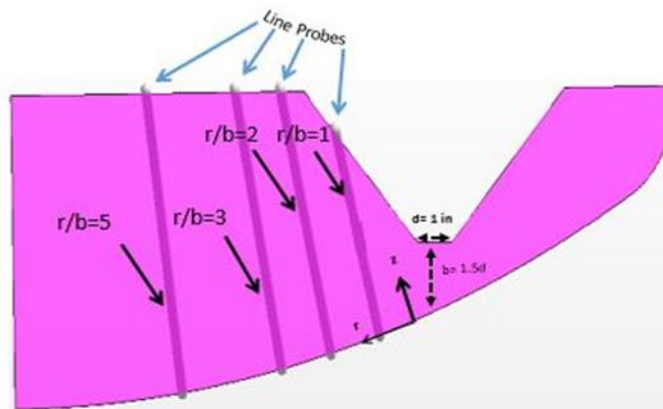
The schematic shows the key physical dimensions, coordinate axis, flow variable directions and associated boundary conditions. The computations assume a 2D axisymmetric flow conditions due to presence of symmetry, in which z is directed to the wall-normal jet impingement direction, while, r indicates the coordinate in radial wall parallel direction. The radial and wall normal velocities are described by u and w , respectively. The gap between the nozzle exit and the bottom plate is considered as $b/d = 12$ and 1.5 as schematically shown in Figure 24 (a) and (b) respectively, while, the horizontal distance is kept fixed at $L_r/b = 3$. To improve the stability of the solution a nozzle height of 2D is adopted for high $b/d = 12$, while, the outlet plane is placed at a large distance from the stagnation impinging point to avoid any error at outlet plane to affect the inside domain of interest. The Reynolds number based on jet velocity U_0 at nozzle exit, diameter of nozzle (d) and considering air as the working fluid, is kept fixed at $Re = 1.96 \times 10^5$ for both the calculations. An axisymmetric boundary condition is imposed at the left vertical surfaces having jets, while, pressure-outlet boundary condition is enforced at the right outer vertical surface and top horizontal surface in-order-to ensure realistic outflow of jet leaving the computation domain in unconfined space. In the actual experiment, the jet is created from the nozzle as plug uniform flow with negligible inflow turbulence; thus, uniform plug flow with 3% turbulence intensity is assigned to mimic the exact experimental conditions. The bottom flat surface is enforced with no-slip boundary conditions.

Computation details of radial wall jet on curved geometry of PJM vessel

The schematic in Figure 25(a) shows a 3D computational domain depicting one-quarter of an actual PJM vessel geometry possessing a single circular nozzle close to the bottom curved surface, while, Figure 25(b) illustrates the corresponding 2D symmetric plane along with probe locations at which the radial velocity profiles have been extracted.



(a)



(b)

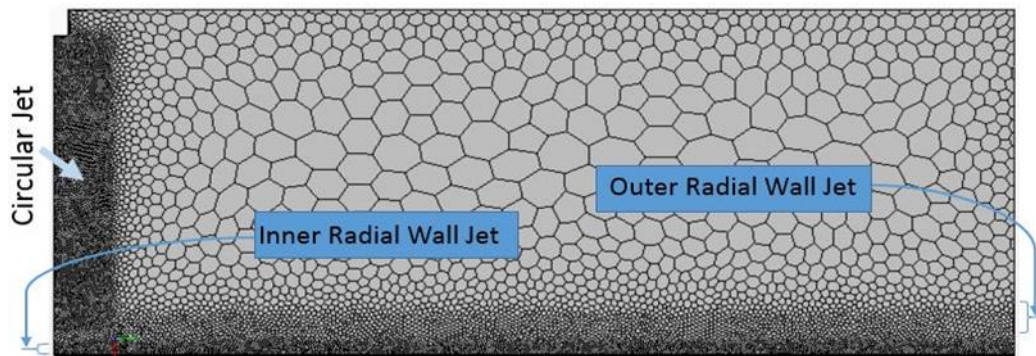
Figure 25. Schematic of PJM geometry and computational domain showing the geometrical dimensions with associated boundary conditions and the probe locations of radial velocity data extraction (a) 3D-quarter scaled down PJM vessel geometry and (b) 2D plane of symmetry on which data was sampled.

The geometrical dimensions and the flow properties follow the actual operating conditions of a PJM vessel at the WTP facility. In the current study, water jet at a velocity of $U_0 = 26 \text{ ft/s}$ is created from a circular nozzle of diameter $d = 1 \text{ in.}$, placed at a normal distance of $b = 1.5d$ from the bottom curved surface, while, the radius of the PJM vessel is $R = 19.7 \text{ in.}$ as shown in Figure 25. The corresponding Reynolds number which is based on jet velocity, diameter of nozzle (d) and considering water as working fluid, is kept fixed at $Re = 2.03 \times 10^5$. The jet from the nozzle strikes on the impinging surface and subsequently turns to form a radial wall jet away from the impingement region. The simulation is performed in a 3D computational domain and the data is visualized at a 2D symmetric plane in-which, z is directed opposite to the wall-normal jet impingement direction and r indicate coordinates in radial wall parallel direction. A pressure-outlet boundary condition is imposed at the two inner vertical surfaces with the top surface having the jet, in-order-to to ensure realistic outflow of jet leaving the computation

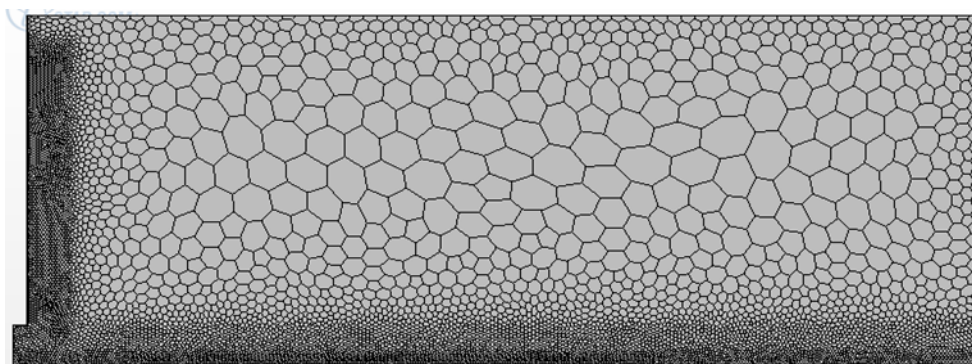
domain. At the nozzle exit uniform plug flow with 3% turbulence intensity is assigned. A no-slip boundary condition is imposed on all remaining solid surfaces.

Numerical grids

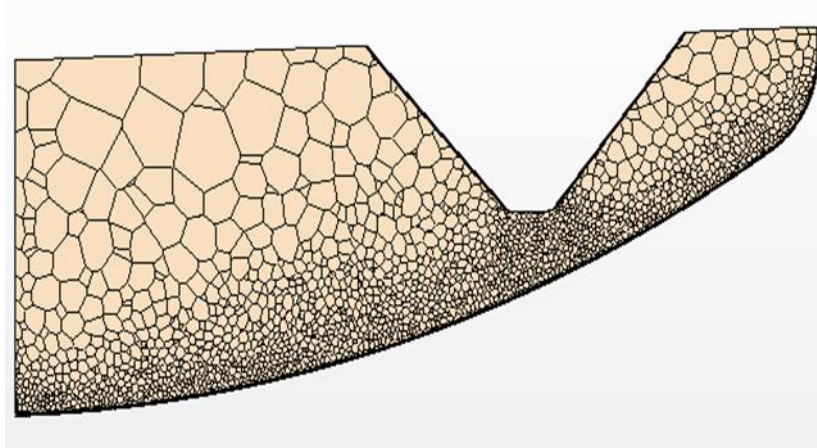
Spatial resolution and numerical accuracy are major issues in the calculation of complex flows. The current impinging jet flows have different important regions such as the initial free jet region, impinging zone and wall jet region, which need special grid refinement due to associated complex flow structures. A finer grid in-and-around the jet periphery in the free jet region accurately resolves the free shear layer to ensure correct generation of turbulence along the shear layer, while the finer grid resolution in the bottom impinging zone is required to capture the high velocity gradient and fine streamline curvature of deflected radial wall jet velocity profiles. However, the radial wall jet velocity profiles away from the impingement regions show sharper velocity gradients near the wall, which demands a very fine mesh to resolve the boundary layer and also, careful transition of mesh sizes in the wall normal direction is necessary to avoid oscillations in the numerical data. Bearing in mind the aforementioned requirement, the grid resolution and grid distribution in various regions have been judiciously selected as shown in Figure 26(a), in-which, special custom-controlled regions such as circular jet, inner radial wall jet and outer radial wall jet in impinging and radial jet zones are designed for grid refinement.



(a)



(b)



(c)

Figure 26. Computational mesh showing polyhedral mesh properties (a) flat surface geometry with $b/d = 12$ and (b) flat surface geometry with $b/d = 1.5$ and (c) PJM curved geometry with $b/d = 1.5$.

The computational mesh properties comprise polyhedral unstructured meshes combined with a near wall prism layer as shown in Figure 26. The grid distribution in and around the nozzle enveloping the locus of vertical jet indicates a very fine grid along jet periphery to resolve the shear layer. For the in-wall normal direction, the grids are clustered near the bottom impingement wall by employing very fine prism layers to resolve the boundary layer and capture high velocity gradients, while, a very fine grid is used in the radial wall jet region by adopting special custom controlled mesh techniques. Grid properties outside the jet regions and near the top wall are made relatively coarser due to smaller velocity gradients. The circular jet mesh region extends the total height in the vertical direction and the horizontal direction spans up to “2d” in size, where, the grid resolution is $0.05d$. The thickness of the inner-radial wall jet mesh and outer-radial wall jet mesh regions are $1d$ and $3d$, where, grid resolutions are $0.1d$ and $0.15d$. However, four prism layers with a total thickness of $0.05d$ is assigned on the bottom impingement wall, which places the first grid cell at $0.0025d$ from the bottom impingement wall to completely resolve the boundary layer. The grid sensitivity study and the grid resolution in the wall coordinate (z^+) on both the walls are reported in the result and discussion sections.

RESULTS AND DISCUSSIONS

Numerical simulations in radial impinging jet configurations were conducted in a 2D axisymmetric computational domain with the flat surface (Figure 24) and in a 3D cylindrical computational domain with the curved surface geometry (Figure 25). The main objective of the present work is to revisit the wall-normal variations of radial wall jet velocity profiles at various radial locations and subsequently determine the local maximum of radial jet velocity and corresponding jet-half width. It is to be noted that two length scales, such as the diameter of jet and the distance between the jet exit to impingement plate are relevant for the analysis of radial wall jet velocity profiles, thus alternatively used.

Specifically, the radial wall jet behavior depends on two important normalized length scales: jet exit to impingement plate gap ratio and the radial location (r/d) or (r/b), where, r measures distance along the wall in radial direction. The scaling (r/b) is particularly important since the velocity correlation in literature is provided as a function of these length scales. The Reynolds number of interest for flat surface geometry is, $Re = U_0 d / \nu = 1.96 \times 10^5$, with nozzle jet diameter, $d = 2$ in., jet velocity at nozzle exit of ($U_0 = 265$ ft/s) and considering air as jet fluid. In the flow configurations, the jet diameter corresponds to the experimental set up of Poreh (1967). In order to explore the effect of impinging jet height (b) on the wall jet velocity profiles, two (b/d) ratios of 12 and 1.5 are considered, in-which, the case with larger jet to impingement distance corresponds to the Poreh's experimental configuration. Further, to compare Poreh's experimental data, the wall-normal (z) profiles of time-averaged local radial jet velocity (U) are evaluated at the same radial locations as of Poreh at $r = 24, 36, 48, 60$ in as schematically shown by line diagrams in Figure 24, leading to a non-dimensional radial distance of $12 \leq r/d \leq 30$ for both the cases. But, when normalized by impinging jet height (b), the numerical value of non-dimensional length scale (r/b) becomes $1 \leq r/b \leq 2.5$ for $b/d = 12$, and $8 \leq r/b \leq 20$ for $b/d = 1.5$. However, in PJM curved geometry, the Reynolds number is set as $Re = U_0 d / \nu = 2.03 \times 10^5$, with a nozzle jet diameter, $d = 1$ in., jet velocity at nozzle exit of $U_0 = 26$ ft/s and water as working fluid, while, the nozzle exit is placed at a normal distance of $b = 1.5d$ from the bottom of the curved surface.

As mentioned earlier, the geometrical dimensions of the PJM computational domain follows the actual PJM vessel at the WTP (B. Rosendall, 2006). Here, the maximum outer radius of the confining vessel surface is $R = 19.7$ in., which is smaller compared to the maximum physical radial distance of Poreh's experimental data. Therefore, to examine the radial wall jet velocity profiles at the same non-dimensional length scale (r/b) as of Poreh, the radial location is selected as $1 \leq r/b \leq 5$, as shown in Figure 25 (b), which yields $1.5 \leq r/d \leq 7.5$. A standard $k - \epsilon$ turbulent closure based on the RANS eddy viscosity model was used and is coupled with a two-layer model (TLM) near wall treatment approach. The present numerical data have been compared with experimental hot-wire anemometer data of Poreh (1967). Additionally, the numerical data from the present computation have been assessed by comparing with Poreh's correlation where direct experimental data was not available. The discussions are restricted to velocity fields, in which comparison are made for wall-normal distributions of mean radial velocity profiles at different radial locations. The wall-normal profiles of time-averaged local radial jet velocities are evaluated at various radial locations as schematically shown by line diagrams in Figure 24 and Figure 25(b). Subsequently, the local maximum of radial jet

velocity (U_m) and the corresponding jet half-width are calculated at various radial locations from the local radial jet velocity profiles. These computed U_m and δ values are compared with the values obtained from Poreh's correlation. Further, the velocity contour plots are examined to illustrate the various regimes of jet development. In all representations and explanations, the velocity variables are normalized with maximum local radial jet velocities and the geometrical dimensions are by jet diameter or jet-to-impingement plate thickness.

The study mainly focuses on the variations of the major geometrical length scale parameter (b/d) and the type of impingement surfaces. Note that the wall jet velocity profiles depends on impinging height, even for a large $b/d \geq 8.3$ and at a large radial distance far away from the stagnation point (Poreh et al., 1967). The impinging jet is classified as "small" when, $b/d \leq 5.5$ and "large" for $b/d \geq 8.3$. (S. Beltaos & Rajaratnam, 1977). Therefore, the analysis and discussion is sub-divided into three sections as: flat surface geometry with $b/d = 12$ and 1.5 , and the curved surface geometry of PJM vessels with $b/d = 1.5$. The foregoing results especially attempt to reinvestigate Poreh's correlations of decay of maximum radial wall jet velocity and spread of radial wall jets along the radial directions to examine the dependence of b/d and geometry of the impingement surface. The analysis is done by systematically comparing the mean velocities at various radial locations with Poreh's experimental velocity data and subsequently comparing with the functional form of the correlated variables. The study focuses the data at radial locations far from the jet impingement region which is consistent with practical applications of PJM devices. The current work reveals interesting features of radial jet velocity scaling for curved impinging surface at low jet heights.

Grid sensitivity

A systematic grid sensitivity study was carried out to determine the influence of mesh density on the accuracy of numerical results and to finalize appropriate grid size and grid density that provide grid independent solutions. As mentioned earlier, the flow fields in circular free jet zones, impingement zones on bottom surfaces and wall jet zones, needs finer grid resolution. Areas outside the jet regions and near the top wall grid size requirements are less restrictive due to smaller velocities. A successful grid sensitivity study ensures quality for criteria such as variation of grid sizes, as well as grid distributions among various regions. Therefore, mesh sensitivity analysis was performed by changing the grid size and comparing the mean velocity fields on both the circular jet region and radial wall jet region as shown in Figure 26(a) to ensure the convergence of the velocity profiles. The grid density in the circular jet region was varied as $0.1d$, $0.05d$ and $0.025d$ and the resulting horizontal distribution (r) of vertical jet velocity profiles at a vertical height of $0.5b$ were compared as shown in Figure 27(a).

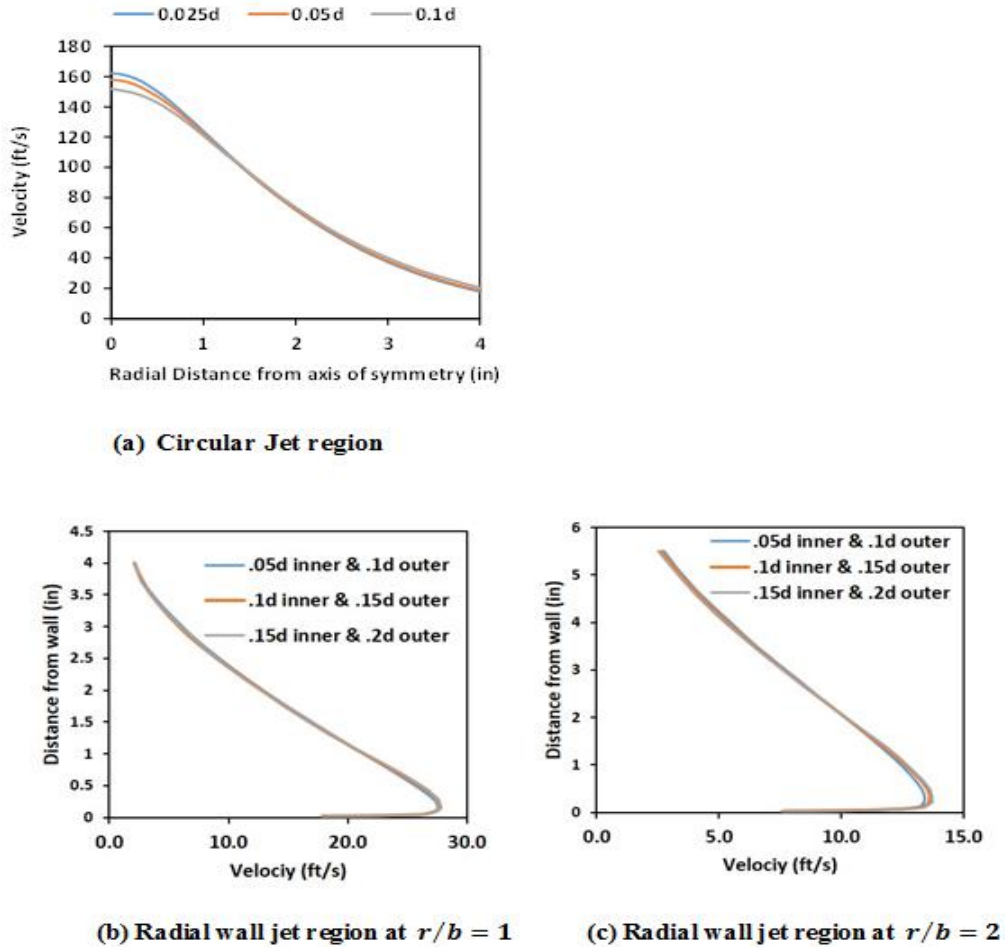


Figure 27. Grid sensitivity test on mean velocity profiles (a) Circular Jet region (b) Radial wall jet region at $r/b = 1$ and (c) Radial wall jet region at $r/b = 2$.

It is observed that velocity profiles within the jet thickness ($r \leq 1$ in.) do not change significantly and become asymptotic outside the jet region ($r \geq 1$ in.) with reducing mesh size below 10% of the nozzle diameter (d). The grid sizes in the inner-radial wall jet regions were again varied as $0.15d$, $0.1d$ and $0.05d$, while, grid sizes in the outer-radial wall jet regions were refined as $0.2d$, $0.15d$ and $0.1d$. This was done to examine the variation of the wall normal distribution (z) of the radial velocity profiles (U) at two different radial locations ($r/b = 1$ & 2) as illustrated in Figure 27(b) and (c). Comparisons of velocity profiles suggest that a grid size of $0.1d$ in the inner radial wall jet region and $0.2d$ in the outside radial wall jet region are sufficient to yield grid independent radial jet velocity profiles. Therefore, the final mesh uses a grid size of $0.05d$ in the circular jet region and $0.15d$ at the inner radial wall jet region with $0.15d$ mesh size in the outer radial wall jet region. Regions outside the jet, use a grid size between $0.25d$ to $0.4d$. However, four prism layers were specified near the bottom impingement wall within a total thickness of about 5% of the nozzle diameter (d), in all calculations, which placed the first grid at $0.0025d$ from the bottom wall yielding the first grid at $z^+ \leq 2$. This study leads to a final mesh count of about 20,000 and 17,000 for 2D flat surface geometry of $b/d = 12$ and 1.5 respectively, while, the total grids for 3D PJM vessel become 310,000.

Analysis of CFD data for flat surface geometry at jet to impingement distance $b/d = 12$

The next section presents the results corresponding to Poreh's experimental test case set up for a jet impingement aspect ratio of $b/d = 12$ and at radial locations far from the jet impingement region at $12 \leq r/d \leq 30$ or $1 \leq r/b \leq 2.50$. It should be noted that the wall jet region starts to develop at the end of the impingement region and the transition occurs at $r/b = 0.22$ (Spyridon Beltaos & Rajaratnam, 1974), indicating the current wall jet profiles are all in the developed wall jet regions.

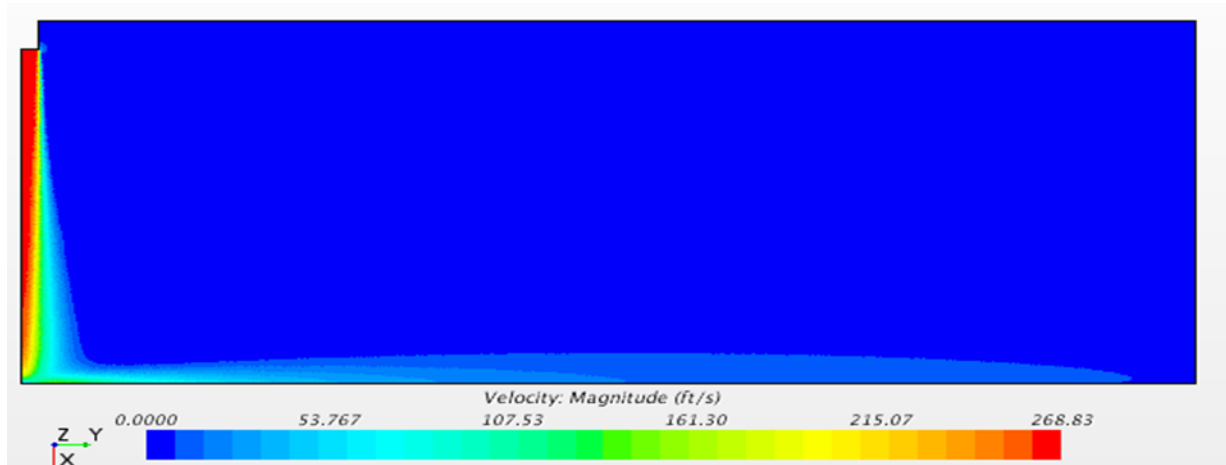


Figure 28. Contours of velocity magnitude illustrating various regimes of circular jet, impingement region and formation of radial wall jet for flat surface geometry at jet to impingement distance of $b/d = 12$.

The contours of velocity magnitude, shown in Figure 28, illustrates three distinct flow regions: the free-jet region, impingement region and the wall-jet region, confirming the general nature of the impinging jet reported in the literature. Since the current geometry possesses a “large” aspect ratio of $b/d = 12$, the potential core of the jet is clearly visible, while, the free-jet region becomes fully developed before entering to impingement region.

As shown in Figure 28, after impingement, the fluid flows along the wall that creates a boundary layer in-which the radial wall jet forms and the flows spread upward by increasing the jet thickness. Near the bottom surface, around $r/d = 0.5$, the contour of velocity shows a rapid increase in velocity magnitude due to flow acceleration away from stagnation line. In addition, away from the impingement region, the direction of flow completely changes from axial to radial direction as illustrated by the nearly wall parallel velocity contour maps. All these features are consistent with the general features of impinging jet flows reported in literature (Craft et al., 1993).

The wall-normal distribution of local mean radial wall jet velocity profiles at four radial locations far away from the stagnation point at $r/b = 1, 1.5, 2, 2.5$ are displayed in Figure 29. The experimental velocity data of Poreh (1967) are also overlaid for detailed comparisons.

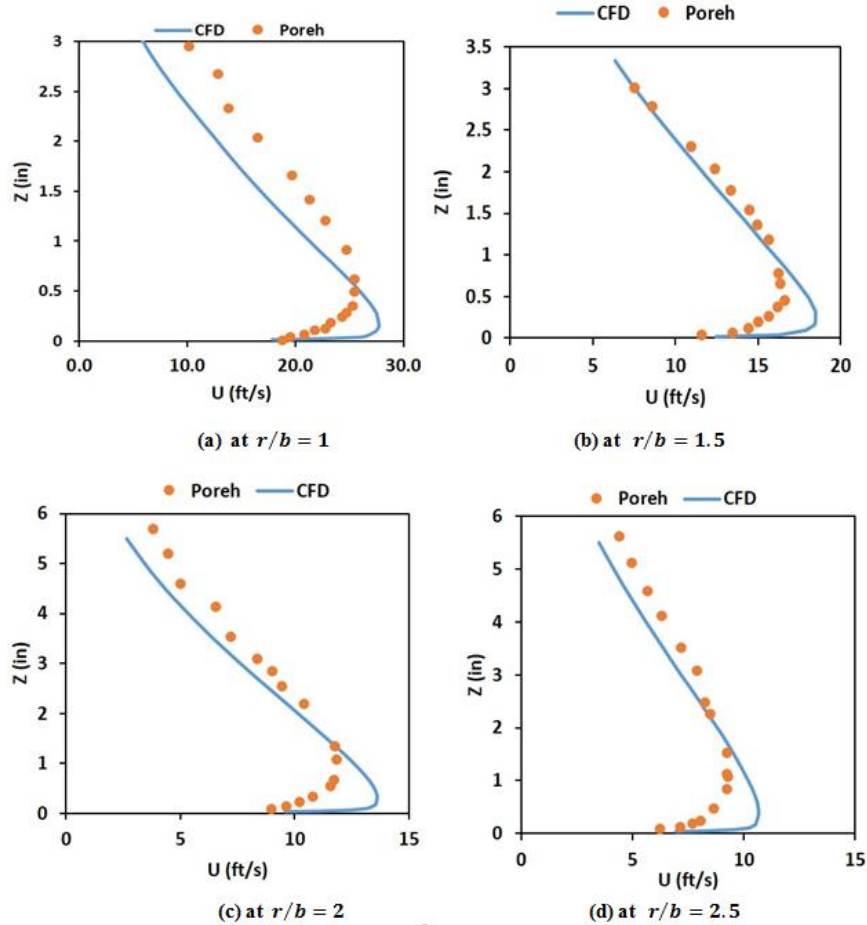


Figure 29. Comparison of wall-normal distribution of radial wall jet velocity profiles at radial locations; (absolute scale) (a) $r/b = 1$ (b) $r/b = 1.5$ (c) $r/b = 2$ (d) $r/b = 2.5$.

In the figures, both the distance and velocity values are in absolute scale. As seen from the plot (Figure 29), the present mean radial jet velocity profiles at all four radial locations achieve their peak values (U_m) at a close distance from the wall and the maximum values at successive radial locations are progressively decreasing due to mixing of the wall jet with the quiescent ambient fluid. The location of peak velocity values steadily move upward from the bottom wall along the downstream radial locations, indicating the increase in jet thickness. However, the present radial velocity curves in the proximity of the bottom surface show relatively sticky and thinner profiles yielding a steeper velocity gradient. The corresponding maximum values of local radial wall velocity (U_m) at all four locations slightly over-predict, with the location of the of peak values slightly closer than that observed by Poreh (1967). In the outer-region, the velocity profile at $r/b = 1$ slightly falls below, but further downstream at $r/b = 1.5, 2, 2.5$, the CFD profiles attains fairly close agreement with the experimental curves showing a similar slope of velocity profiles. Although, quantitative agreement between the numerical and experimental data near the bottom wall is slightly less satisfactory, qualitatively, the radial velocity profiles demonstrate similar trends near the wall as observed in experimental study. Further, the radial wall jet profiles at the outer layer away from the wall are in reasonable agreement with the experimental values. At very high Reynolds numbers, it is expected to see the development of an inner shear layer within the wall jet due to viscous interactions with the solid surface producing a very thin

boundary layer in the proximity of the wall. This near wall phenomenon poses a high degree of uncertainty in the experimental measurement of near wall velocity and similarly, the CFD turbulence model often experiences difficulties capturing near wall features as well. Note that the experimental data by Poreh et al. (1967) was gathered by single hot-wire anemometers which sometimes are unable to differentiate properly between the vertical and radial velocity components as reported by M. Fairweather & G. Hargrave (2002). Their studies had similar impinging jets at a small jet impingement ratio ($b/d = 2$) and at low Reynolds numbers and the authors noticed slight disagreement with the Poreh's experimental data. It will be shown later that the near wall discrepancies in the velocity data has little effect on the non-dimensional velocity profiles, as well as on Poreh's correlations.

As mentioned earlier, the radial wall jet achieves fully developed self-similar profiles at a radial distance $r/b = 0.22$ from the stagnation point. The self-similar wall jet velocity distribution can be expressed in a non-dimensional form and is shown in Figure 30. This illustrates the wall-normal (z/δ) variations of the normalized profiles of the local mean radial wall jet velocity (U/U_m) at different radial locations.

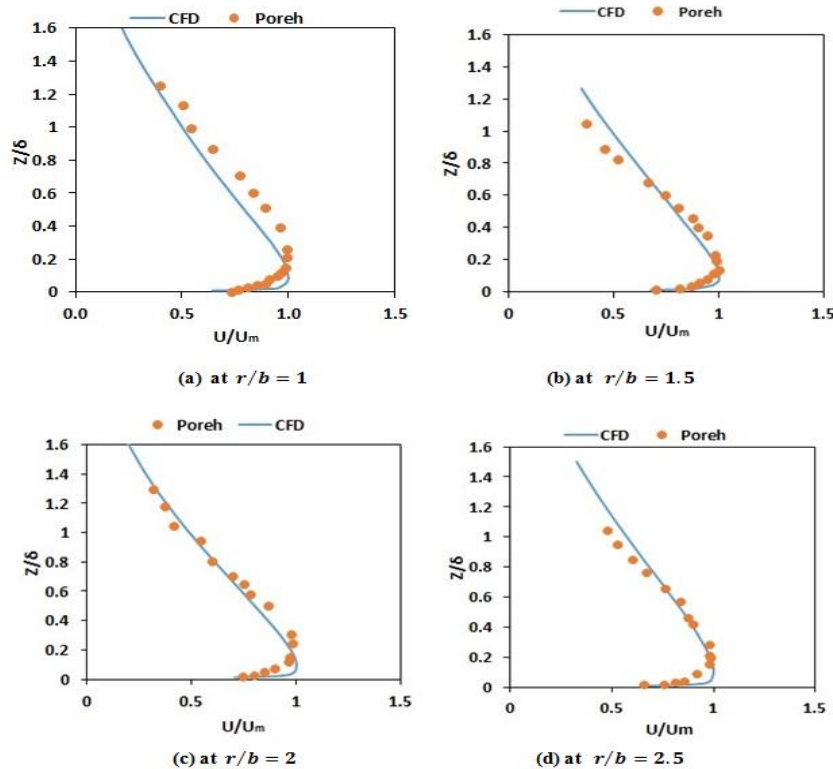


Figure 30. Comparison of wall-normal distribution of radial wall jet velocity profiles at radial locations; (normalized scale) (a) $r/b = 1$ (b) $r/b = 1.5$ (c) $r/b = 2$ (d) $r/b = 2.5$.

In this figure, the velocity scale, U_m refers to the maximum of local mean radial velocity at a particular radial locations, while, the length scale, δ is measured as the value of z where the radial wall jet velocity falls to $0.5U_m$. Interestingly, the normalized radial velocity profiles at all four radial locations from the current CFD study fit closely with the experimental curves, except a slight discrepancy in the near wall peak velocity location which is observed in Figure 30.

In order to examine the slight mismatch of radial velocity profiles in the proximity of the wall, FIU carried out another fine grid simulation by doubling the grid and also explored a low Reynolds number simulation at $Re = 23000$ (Cooper et al., 1993). Figure 31 shows a comparison of normalized radial jet velocity profile at only a single radial location of $r/b = 1$.

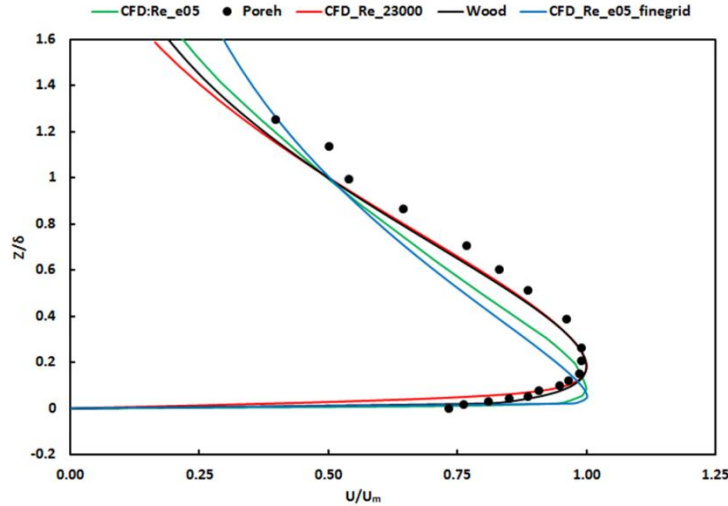


Figure 31. Comparison of wall-normal distribution of radial wall jet velocity profiles at radial location at $r/b = 1$; (normalized scale).

Figure 31 included the empirical self-similar velocity profiles by Wood et al. (2001), who proposed the correlation following their experimental observation of similar impinging jet flows over the same range of Reynolds number but at a smaller b/d ratio. The empirical relation given by Wood et al. (2001) is written in terms of the error function as:

$$U/U_m = 1.55(z/\delta)^{1/6}[1 - \text{erf}(0.70 z/\delta)] \quad [3]$$

Near the wall, the current radial velocity profile at low Reynolds number (shown in the red solid color) show excellent agreement with experimental curves of Poreh et al. (1967) and empirical velocity distribution of Wood et al. (2001), although the later profiles were obtained at higher Reynolds numbers. However, at high Reynolds numbers, comparison of current CFD radial velocity profiles between two grid resolutions, shown by green and blue solid lines, indicate no improvement in near wall jet velocity profiles with further grid refinement. Since, the current radial velocity profile at low Reynolds number matches very well the Poreh's experimental data and at high Reynolds numbers, the grid refinement became unable to eradicate the near wall velocity issues. The discrepancies in the near wall jet velocity profile, may be attributed either to the weakness of CFD turbulence model to capture near wall jet characteristics or the scatter and uncertainties involved in the near wall experimental data at high turbulent intensity at high Reynolds numbers. Note that, similar types of disagreement in the radial jet velocity profiles were reported by Shademan, Balachandar, Roussinova, & Barron (2016) in their highly resolved Large Eddy Simulation (LES) of impinging jets at a low Reynolds number range, while, Hargrave, Williams, Anandarajah, & Halliwell (2006) witnessed similar mismatches between their experimental data and Poreh's data, concluding lack of spatial resolution. However, shown

later, these mismatches do not affect the empirical correlations too much, and are considered within an acceptable range.

In the next section FIU will illustrate the development of maximum local mean radial velocity (U_m) and jet thickness (δ) at each station along the radial direction by comparing the current CFD data with Poreh's correlation described by Eq. (1) and Eq. (2). The velocity and length scale of impinging wall jets are particularly important for designing purposes in industrial applications involving impinging jets such as those in a PJM vessel and are often calculated from Poreh's correlation. In an impinging wall jet, an inner shear layer is created due to viscous interaction by the no-slip wall and the outer shear layer is developed when the peak wall jet velocity decay due to stagnant ambient fluid. These two shear layers control the maximum value U_m and δ . Thus accurate predictions of these two parameters are very sensitive on the associated scatter of measurements as well as CFD data.

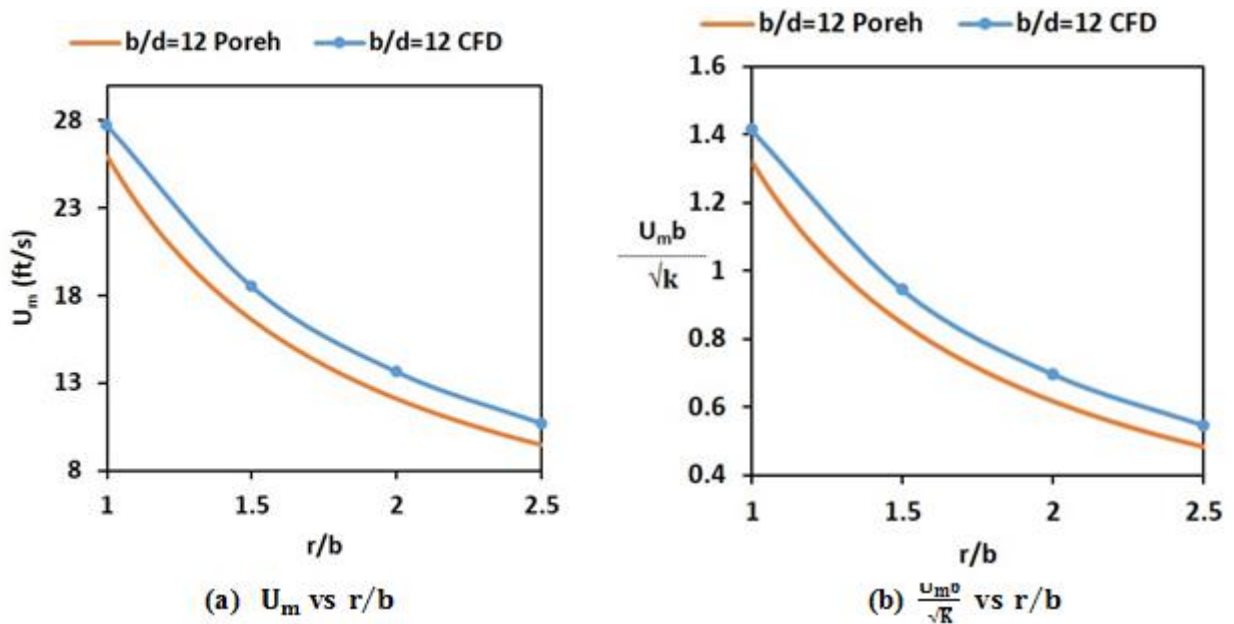


Figure 32. Comparison of radial variation (r/b) of maximum radial wall jet velocity for $12 \leq r/d \leq 30 \sim 1 \leq r/b \leq 2.5$; (a) maximum radial wall jet velocity (U_m) (b) non-dimensional maximum radial wall jet velocity ($\frac{U_m b}{\sqrt{K}}$).

The radial variations of maximum radial wall jet velocity in dimensional and non-dimensional ($U_m b / \sqrt{K}$) form are shown in Figure 32(a) and (b) respectively, displaying steady decay of peak radial velocity at each radial station with increasing radial distance. Comparison of the current CFD data with that of Poreh's correlation indicate reasonable agreement in the slope of decay of maximum jet velocities, while, the numerical values of current maximum radial jet velocity slightly over-predict, as noted earlier.

Another important scaling parameter of the radial wall jet is the length scale, δ , which measures the spreading rate of wall jet referred as jet half-width and the corresponding radial variations of dimensional and normalized δ is depicted in Figure 33 (a) and (b), respectively.

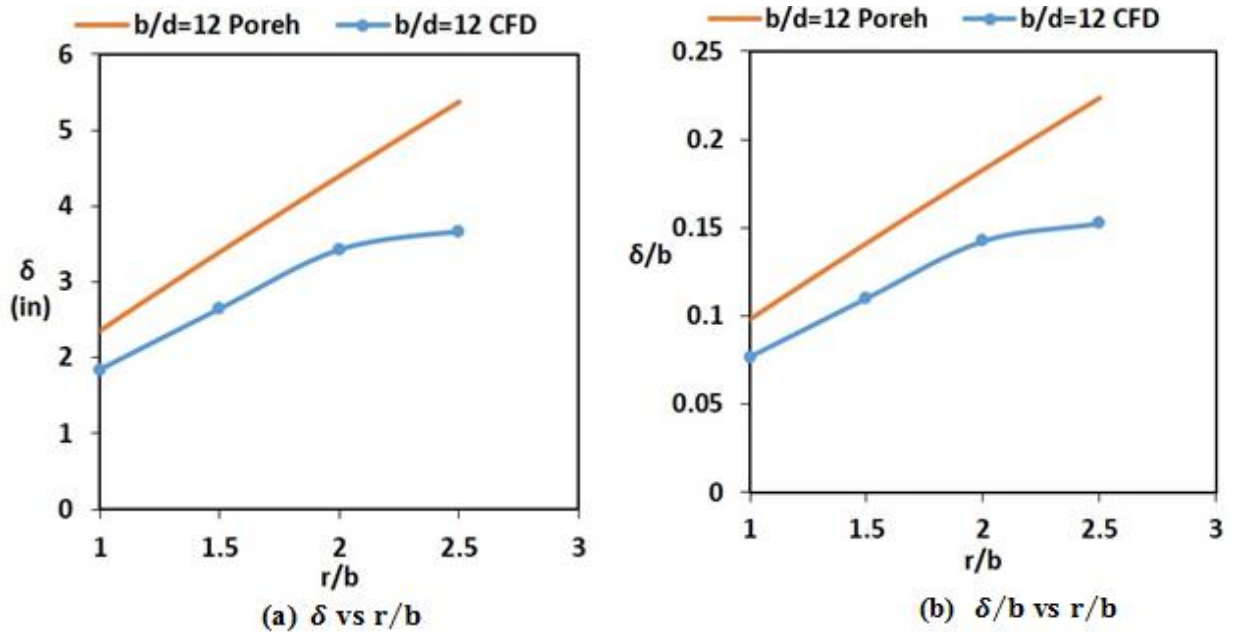


Figure 33. Comparison of radial variation (r/b) of radial wall jet thickness for $12 \leq r/d \leq 30 \sim 1 \leq r/b \leq 2.5$; (a) radial wall jet thickness δ (b) non-dimensional radial wall jet thickness δ/b .

The current spreading rate of the wall jet closely follows the Poreh's correlation and the overall trends are in reasonable agreement at all radial locations up to $r/b = 2$. Although the numerical value at $r/b = 2.5$ shows a slightly lower value, which is located far downstream at a large distance from the stagnation point and very close to pressure-outlet boundary. In addition, the current CFD data established a linear spreading rate over a larger range when compared to Poreh et al. (1967), although the present data predicts a slightly slower growth rate. Note that the growth rate, δ , reported by many earlier experimental and theoretical investigations ((Glauert, 1956), (Lauder & Rodi, 1983), (Dianat, Fairweather, & Jones, 1996), (Cooper et al., 1993), indicate varying over a small range. Thus the current δ trends are commensurate with the findings reported in literature.

In summary, the maximum local radial wall jet velocity and the spreading rate of wall jet from the present simulation are in good agreement with the Poreh's correlation and the relative discrepancies between the current data and experimental values spans over a small range. In similar high Reynolds number impinging wall jet studies with $b/d = 3$, Sengupta & Sarkar (2008) investigated U_m and δ characteristics employing a PIV experimental technique and CFD data using LES and RANS models. The authors also, compared their data with the experimental data of Cooper et al. (1993) and Poreh et al. (1967), in-which they found that, although their experimental U_m and δ fit well, the numerical values using various turbulence models were less satisfactory and varied over a small range. In an another recent study, Ghaneezad et al. (2015) obtained similar scatter in U_m and δ data over a radial location $r/b \leq 1$, in a low Reynolds number impinging jet with a larger $b/d = 24$. The above discussion suggests that the U_m and δ variation from current CFD data are well within the acceptable limit and the slight mismatch may be attributed to the intrusive nature of hot-wire probe or directional dependence arising in the probes at high turbulent intensity flows or the weakness of eddy-viscosity turbulence model.

Analysis of CFD data for flat surface geometry at jet to impingement distance $b/d = 1.5$

In the current section numerical data is presented for relatively shorter aspect ratios of jet-to-impingement with $b/d = 1.5$, keeping other geometrical parameters and the Reynolds number the same (as earlier case of $b/d = 12$). This was done to examine the applicability of Poreh's correlation for shorter aspect ratios. The aspect ratio of $b/d = 1.5$ is particularly important due to their frequent practical application in PJMs, environmental soil erosion, and in thunderstorm microbursts. Further, the radial jet velocities are evaluated at the same radial locations as with the earlier case ($b/d = 12$) at $r = 24, 36, 48, 60$ in. This is schematically shown by line diagrams in Figure 24(b), leading the same non-dimensional radial distance of $12 \leq r/d \leq 30$ for both the cases, when normalized by jet diameter, but yields a different non-dimensional value length scale as $8 \leq r/b \leq 20$, when normalized by impinging jet height.

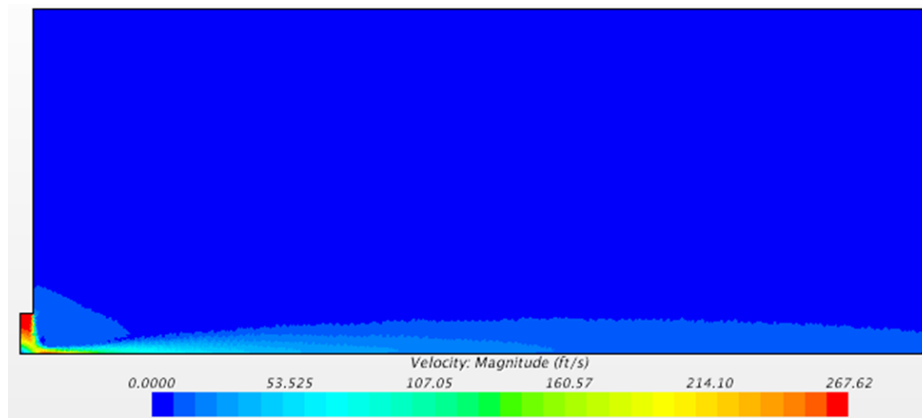


Figure 34. Contours of velocity magnitude illustrating various regimes of circular jet, impingement region and formation of radial wall jet for flat surface geometry at jet to impingement distance of $b/d = 1.5$.

Figure 34 displays the contour of the velocity map, showing the evolution of jet features such as transition of potential core, meandering of jet structures in impingement zone and subsequently the formation of radial wall jets after deflection. Due to the smaller aspect ratio (b/d), the potential core jet region overlaps the stagnation region yielding velocity fields that remain in the development stage before impinging on the bottom surface. The ring vortex near the deflection zone strongly interacts with the entrained ambient fluid leading to shifting of impingement zone to the right side of geometric center of the jet and subsequent formation of a high velocity region. However, the radial jet velocity profiles are extracted over the range $8 \leq r/b \leq 20$, confirming current jet profiles are all in the fully developed wall jet regions. Since, the main goal is to examine the Poreh's correlation, only distribution of U_m and δ is considered and the local radial jet velocity profiles are not shown.

The comparison of radial decay of local maximum radial wall jet velocity in dimensional and normalized scale display excellent agreement with corresponding Poreh's correlation as shown in Figure 35 (a) and (b). The results show a negligible over-prediction in numerical values consistent throughout all radial locations.

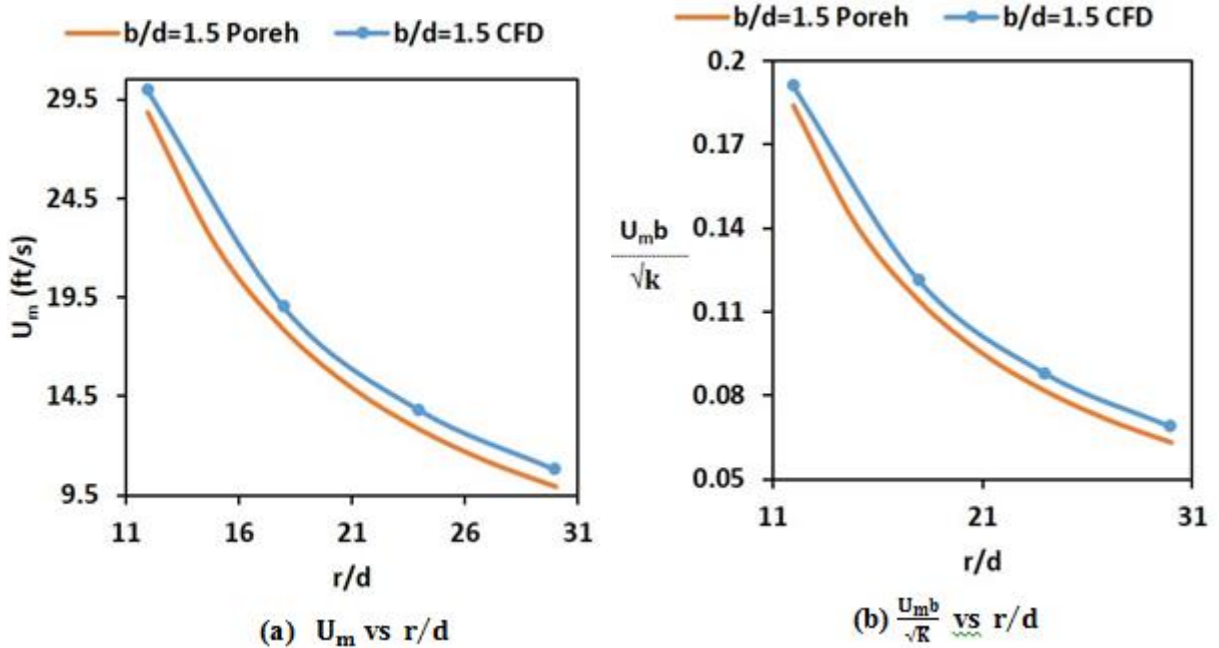


Figure 35. Comparison of radial variation (r/d) of maximum radial wall jet velocity for $12 \leq r/d \leq 30 \sim 8 \leq r/b \leq 20$; (a) maximum radial wall jet velocity (U_m) (b) non-dimensional maximum radial wall jet velocity ($\frac{U_m b}{\sqrt{K}}$).

Interestingly, U_m for both high and low nozzle height conditions, show the same range (Figure 32(a) & Figure 35(a)), indicating the independence of Poreh’s correlation on the geometric

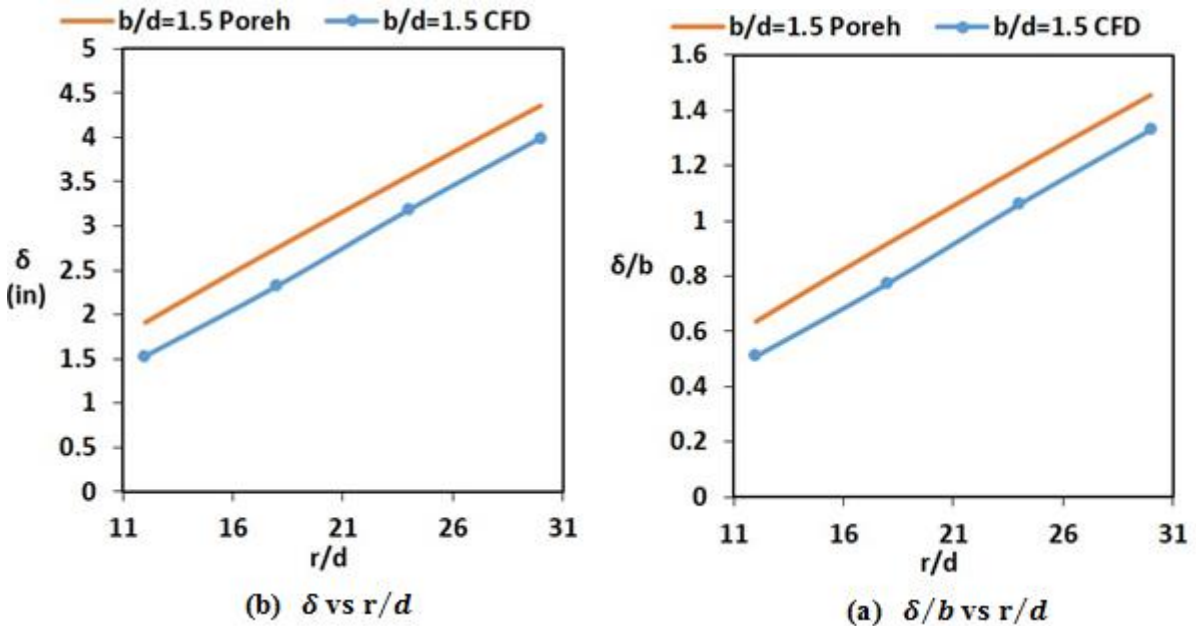


Figure 36. Comparison of radial variation (r/d) of radial wall jet thickness for $12 \leq r/d \leq 30 \sim 8 \leq r/b \leq 20$; (a) radial wall jet thickness δ (b) non-dimensional radial wall jet thickness δ/b .

scaling of nozzle height, at a large radial distance from the stagnation point. Similarly, the radial growth of the jet half-width is plotted in both dimensional and non-dimensional form as (δ) and (δ/b) respectively in Figure 36 (a) and (b). Results show a linear spreading rate and increases steadily at all radial locations, giving identical slope of the wall jet growth rate when compared with Poreh's correlation, although the numerical values of the jet half-width are slightly under-predicted at all radial stations. However, the current δ values at the farthest radial location at $r/b = 2.5$, does not fall short as was observed in the case of large nozzle height (Figure 33). Note that in an similar experimental study (but at a low Reynolds number), the wall impinging jet with $b/d = 2$ (M. Fairweather & G. Hargrave, 2002) had fairly similar agreement of δ decay rate with Poreh's correlation, but, their δ values fall slightly shorter at large radial distance. Thus, the current δ trends are consistent and within an acceptable range.

Although the current simulation was conducted at a smaller nozzle-to-impingement gap ratio ($b/d = 1.5$) which was not considered by Poreh et al. (1967) during their experimental study, the present numerical data for the maximum local radial wall jet velocity (U_m) and the spreading rate of wall jet (δ), agrees satisfactorily with the Poreh's correlation and the relative discrepancies between the current data and correlated values are considered within the acceptable limit. The excellent agreement also suggests that Poreh's correlation is valid for low aspect ratio of nozzle-to-impingement gap (b/d), at a larger radial distance from the impingement zone.

Analysis of CFD data for curved surface geometry of PJM vessels $b/d = 1.5$

The current section presents the results for actual PJM geometry at a shorter aspect ratio of ($b/d = 1.5$) operated at the same Reynolds number ($\approx 2 \times 10^5$). In the PJM application, the impingement surface employs a curved geometry instead of conventional flat surface. As seen from Figure 25(b), the geometry allows the flow of radial wall jet inside a divergent area passage and the jet flow characteristics experience additional confinement effects due to the presence of the curved bottom wall and nozzle surface, at a small radial distance. To examine the radial wall jet velocity profiles, at the identical length scale range as of Poreh's study, the radial jet velocity (U) are investigated over the range at $1 \leq r/b \leq 5$, as shown in Figure 25(b), which gives $1.5 \leq r/d \leq 7.5$, when normalized by jet diameter. The contour of velocity magnitude at a 2D-symmetric plane passing through the middle of the 3D PJM computational domain is depicted in Figure 37. This illustrates the evolution of the jet behavior, indicating again, the overlapping of the core jet region with the stagnation zone, formation of a large size vortex in the vicinity of nozzle exit and offsetting of the impingement region slightly away from the geometric center of jet. A region with high accelerating flow is seen near the stagnation point, where the jet redirects to flow in the radial direction due to meandering. This is a feature which was seen earlier for small nozzle impingement heights with a flat impinging surface.

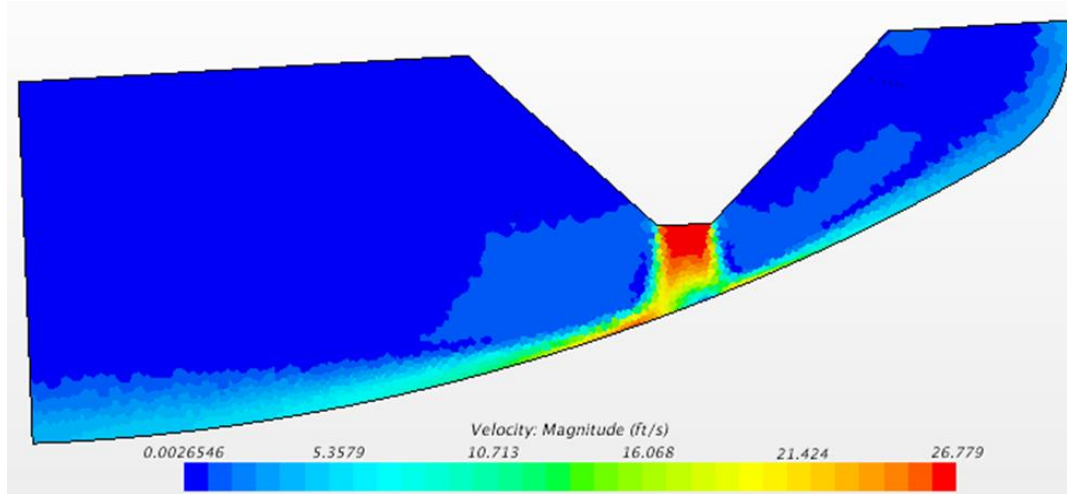


Figure 37. Contours of velocity magnitude at 2D-symmetric plane illustrating various regimes of circular jet, impingement region and formation of radial wall jet for 3D quarter scale PJM vessel with curved impinging surface at a jet to impingement distance of $b/d = 1.5$.

It is evident from Figure 37, the nozzle outer surface and the bottom curved geometry creates a diffuser area leading to thickening of the jet as compared to flat impinging surfaces. The jet after impingement forms two asymmetric radial jets about the stagnation point with a major contribution of the momentum flux being redirected towards the left side of the jet.

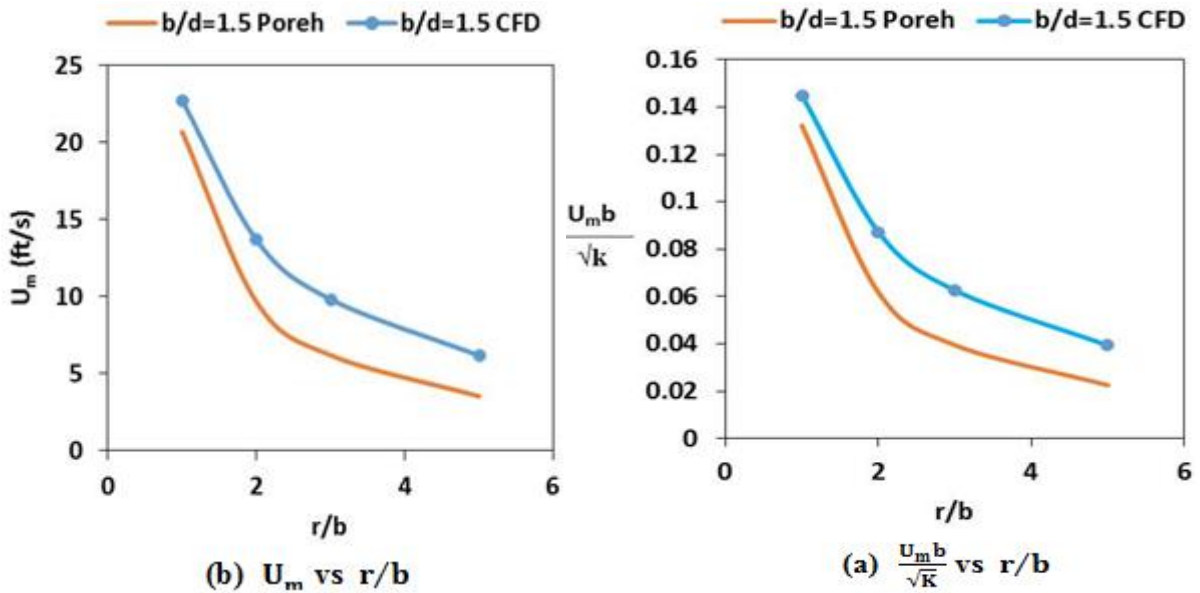


Figure 38. Comparison of radial variation (r/b) of maximum radial wall jet velocity for $1.5 \leq r/d \leq 7.5 \sim 1 \leq r/b \leq 5$; (a) maximum radial wall jet velocity (U_m) (b) non-dimensional maximum radial wall jet velocity ($\frac{U_m b}{\sqrt{K}}$).

The radial variations of U_m and non-dimensional ($U_m b / \sqrt{K}$) form are displayed in Figure 38(a) and (b) which shows steady decay of peak velocity with increasing radial distance. Interestingly, the decay of peak velocity is steeper initially up to $r/b = 2$, due to strong diffuser effects and then the rate of decay drastically reduces in the remaining large radial distance, since the flow

passage again becomes nearly uniform. Overall agreement of radial distribution of maximum radial wall jet velocity with Poreh's correlation is quite satisfactory.

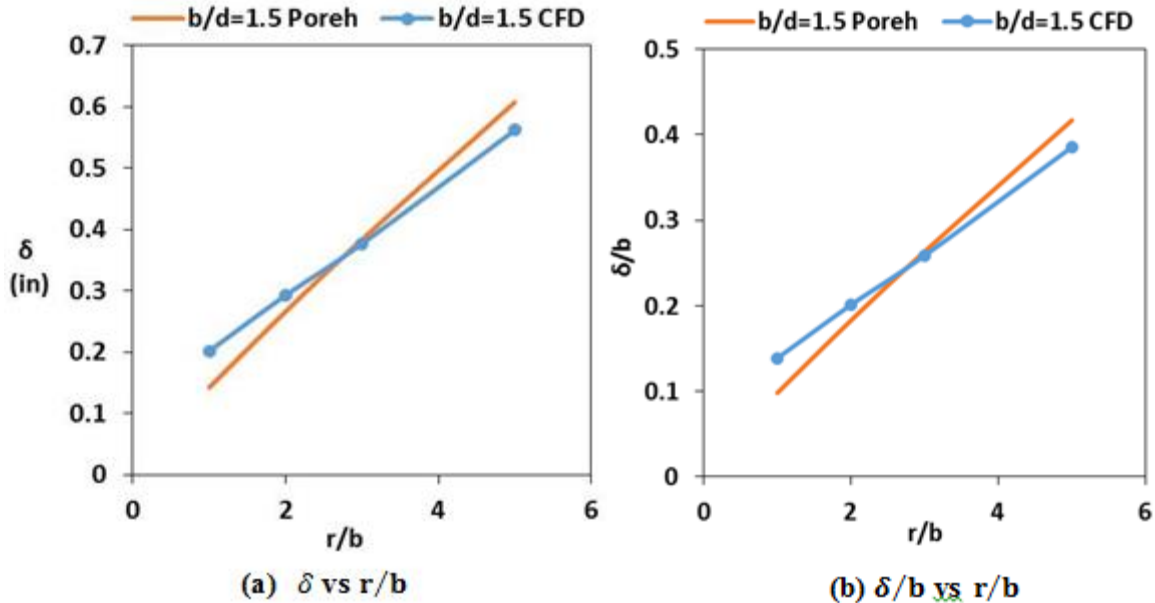


Figure 39. Comparison of radial variation (r/b) of radial wall jet thickness for $1.5 \leq r/d \leq 7.5 \sim 1 \leq r/b \leq 5$; (a) radial wall jet thickness δ (b) non-dimensional radial wall jet thickness δ/b .

The spreading rate of the wall jet (δ) at various radial stations (r/b) as plotted in Figure 39, is steadily increasing with increasing radial distances. This shows the overall trend to fairly agree with Poreh's correlation giving similar linear spreading rate. It was observed that the growth rates are different, predicting higher values of lateral spreading at small radial distance and smaller lateral spreading at larger radial locations. At small radial distances ($r/b \leq 3$), the strong diffusing action, delays the decay of radial velocity profiles at the free turbulent outer region resulting in thickening of the jets. This leads to higher δ , compared to jet flows in constant area passages described by Poreh. At large radial locations ($r/b \geq 3$), the decay of velocity at the outer region become faster due to lesser diffusing effects in the relatively uniform flow passage. Based on the fact that the prediction of δ values are often scattered over a smaller range and the confinement effect leads to slightly different values, the current δ trends can be considered to be consistent with the Poreh's correlation.

In summary, although the present PJM geometry has a curved bottom surface which introduces confinement effects as well as a diffuser action on the development of radial jet flows, the results demonstrate that the radial variation of the maximum local radial wall jet velocity (U_m) and the spreading rate of wall jet (δ) can be well described by the Poreh's correlation and the later can be recommended for calculation jet parameters in practical PJM vessel design.

CONCLUSIONS

The current investigation considers a numerical study of radial impinging jets on both flat and curved surfaces with intentions of reinvestigating the applicability the Poreh's correlations that describe the aforesaid parameter as a functional form. This study evaluates the effect of jet-to-impingement plate gap ratio (b/d) and curved impingement surface on the radial variation of maximum radial wall jet velocity (U_m) and jet-half width (δ). This investigation considers two separate computational domains: first an axisymmetric 2D geometry in which a circular jet from an orifice impinges on a flat surface to form a radial impinging jet in unconfined space, and second, a 3D cylindrical geometry with a curved bottom impingement surface is adopted to mimic the formation of radial impinging jet in an actual PJM vessel. Detailed comparison of the radial mean velocity profiles at various radial locations has been carried out with the experimental data. Further, the decay of local maximum radial wall jet velocity (U_m) and the jet half-width (δ) are compared with the data obtained from Poreh's correlation. Based on these comparisons, the following major conclusions are made:

- The wall normal distribution of the radial wall jet velocity curves show relatively sticky and thinner profiles in the proximity of bottom surface, yielding a steeper velocity gradient due to strong viscous interactions of the wall in the inner shear layer leading to slight over-prediction of local maximum velocity values.
- At a high jet-to-impingement gap ratio ($b/d = 12$), the current normalized radial velocity profiles at all radial locations agrees well with the experimental data, except for a slight discrepancy in the near wall peak velocity.
- The maximum local radial wall jet velocity and the spreading rate of wall jet from the present simulation are in good agreement with Poreh's correlation and the relative discrepancies between the current data and experimental values span over a small range, consistent with the earlier findings reported in literature.
- The comparisons also suggest that the U_m and δ variation from current CFD data are well within the acceptable limit and the slight mismatch may be attributed to the intrusive nature of hot-wire probe or directional dependency that arises in such probes at high turbulent intensity flows and the weakness in eddy-viscosity assumptions employed in RANS turbulence modeling.
- At a low jet-to-impingement gap ratio ($b/d = 1.5$), results demonstrate that the maximum local radial wall jet velocity (U_m) and the spreading rate of wall jet (δ), fairly agrees well with Poreh's correlation and the discrepancies between the current data and correlated values are considered within the acceptable limit, suggesting Poreh's correlation as valid in the low aspect ratio range.
- In PJM geometry, although the development of radial wall jet experiences strong diffuser effects and confinement effects due to presence of curved bottom surface, the radial variation of the maximum local radial wall jet velocity and the spreading rate of wall jet closely follows Poreh's correlation.

- Based on the comparison, it is recommended that Poreh's correlation is valid also for curved geometry and the functional relationship can be used to calculate the jet parameters in practical PJM vessel design.

REFERENCES

B. Rosendall, C. B., F. Wen and K. Knight (2006). *Validating CFD models of multiphase mixing in the waste treatment plant at the Hanford site*. Paper presented at the 14th International Conference on Nuclear Engineering Miami Florida, USA.

Fairweather, M., & Hargrave, G. (2002). Experimental investigation of an axisymmetric, impinging turbulent jet. 1. Velocity field. *Experiments in Fluids*, 33(3), 464-471. doi: 10.1007/s00348-002-0479-7

Fairweather, M., & Hargrave, G. (2002). Experimental investigation of an axisymmetric, impinging turbulent jet. 2. scalar field. *Experiments in Fluids*, 33(4), 539-544.

Poreh, M., Tsuei, Y. G., & Cermak, J. E. (1967). Investigation of a Turbulent Radial Wall Jet. *Journal of Applied Mechanics*, 34(2), 457-463. doi: 10.1115/1.3607705

TASK 18.1

EVALUATION OF FIU'S SOLID-LIQUID INTERFACE MONITOR FOR ESTIMATING THE ONSET OF DEEP SLUDGE GAS RELEASE EVENTS (FIU YEAR 6)

EXECUTIVE SUMMARY

Over the past several years, FIU has developed and tested four full-scale prototypes for its Solid Liquid Interface Monitor (SLIM) for deployment into Hanford high-level radioactive waste (HLW) tanks. SLIM is comprised of a commercial, 3-D profiling sonar combined with a tank deployment system. The sonar's split head design and titanium and polyurethane external surfaces make SLIM resistant to nuclear radiation and highly alkaline solutions (pH>14).

The rapid release of gas generated deep in HLW is called a deep sludge gas release event (DSGRE). This postulated deep sludge gas release event was not described in the Documented Safety Analysis and was the subject of an Unreviewed Safety Question (USQ) for Hanford. This resulted in the high priority given to planning and executing the Deep Sludge Gas Release Event Project and for FIU's effort this past year.

This past year, FIU completed the following:

1. Review of DSGRE reports and bubble imaging articles to develop a test plan.
2. Preliminary proof of principle testing. FIU tested the sonar to demonstrate proof of concept as well as to measure the sonar imaging resolution in order to better define the test plan.
3. Execution of the "Experimental Test Plan to Assess the Utility of 3D Sonars for Monitoring High-Level Radioactive Waste Settled Solids Surfaces for Indicators of Developing Deep Sludge Gas Release Events."
4. Final testing of 3D sonar and image analysis algorithms. FIU's development and testing of FIU imaging software.

Results and conclusions from the research performed for this task this year include:

1. The 3D sonar has a height and lateral resolution of +/- 3 mm for a settled solids surface located ~ 12 inches from the sonar head.
2. FIU can measure the height of settled solids in tanks even with ongoing mixing of solids in the tank by looking at 2D image from a commercial sonar and by post-processing the sonar data to remove sonar signals from extensive scattering off suspended particles and leaving the solids layer on the tank floor.

INTRODUCTION

The retention of flammable and explosive hydrogen gas within deep sludge layers is of great concern for operational safety and for high-level radioactive waste (HLW) transport and storage systems. Hydrogen gas is generated in HLW by radiolysis of chemicals and the concentration of soluble sodium nitrate and nitrite salts and organic compounds that were introduced into the radioactive and chemical waste and over time reacted with the chemical waste. Through operational experience and theory, these flammable gases were shown to escape through cracks created in the HLW. The gases generated are continuously released into tank vapor spaces where air is used to sweep out and remove it.

In recent years, several studies have suggested that there was a limited depth in which these fissures would allow gas to escape. This prompted the concern that gas could build up at certain depths deeper than previously stated inside the Documented Safety Analysis. Gases accumulated at depth can cause a deeper level to become lighter than the layer of waste above it. Based on a phenomenon called buoyant displacement, pockets of gas can be stored in a deep layer of the supernatant where a portion of the settled solids accumulates enough gas to become buoyant. A Raleigh Taylor instability² could very rapidly release the trapped hydrogen, releasing it much quicker than considered in the safety design basis. This rapid release of gas is called a deep sludge gas release event (DSGRE). This postulated deep sludge gas release event was not described in the Documented Safety Analysis and was the subject of an Unreviewed Safety Question (USQ). This resulted in the high priority given to planning and executing the Deep Sludge Gas Release Event Project and subsequently a sub-project called the DSGRE Tall Column Project.

While the DSGRE Tall Column Project executed by WRPS in 2015 was able to quantify upper limits for gas trapping in deep sludge layers, it could not eliminate the possibility of small DSGREs altogether at Hanford. Hanford scientists and engineers identified a technical need to monitor the settled solid surface of HLW in DSTs with deep sludge beds. Specifically this need is for a monitor for settled solids surfaces in tanks to identify increases in the height and volume of these surfaces as indicators of trapped gas and of the potential for evolving deep sludge gas release events (DSGREs). The monitor would allow for prediction of DSGRE onset as well as to ensure that the HLW is not retaining sufficient gas to evolve into a DSGRE.

The purpose of a monitor for DSGREs is to image the settled solids surface layer in deep sludge, DSTs and quantify the change in volume of the waste over time. Hanford personnel would correlate any increase in volume of the waste tank with a mass of trapped gas in the sludge. The monitor could serve two purposes: (1) if the volume of the waste in the tank does not change over time, this can confirm that the mass of trapped gas is low and DSGREs are not of concern; and (2) if the volume of waste does increase over time, then Hanford personnel could estimate the increasing mass of trapped gas and be ready to take action to minimize any risk posed by a DSGRE (e.g., increase flow of sweep gas in the tank headspace).

Aware of FIU's past work in high resolution sonar imaging of settled solids layers and in estimating waste volumes, Hanford personnel recommended that FIU test its 3D sonar to address this technical need. During FIU Performance Year 6, FIU with support from Hanford engineers evaluated SLIM for its ability to precisely measure the change in the height of the settled solids

layer across an entire HLW tank in order to measure small increases in the volume of HLW solids over time as an indicator of trapped gas. This measurement would enable engineers to ensure that the quantity of trapped gases in the deep sludge remains low and that DSGREs will not occur. In addition, SLIM can measure when sufficient quantity of trapped gas has accumulated and raised the HLW volume sufficient to initiate the onset of DSGREs. The figures below show the 3D profiling sonar and its deployment platform for insertion into HLW tanks as large as the 1 million gallons at Hanford.

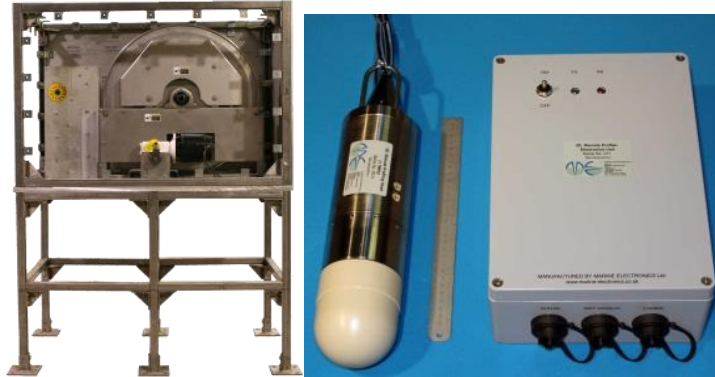


Figure 40. Commercial 3D Profiling Sonar and electronic control box (right) and the gooseneck reel deployment platform (left) which together comprise SLIM.

EXPERIMENTAL TESTING

The objective of this testing was to quantify the accuracy of FIU's 3D sonar in monitoring over time the volume of settled solids in a tank within a particular field of view and to do this for a range of fields of view.

Test Plan

A draft test plan for the SLIM sonar was developed and sent to WRPS and DOE EM on January 22, 2016. The plan was entitled, "Experimental Test Plan to Assess the Utility of 3D Sonars for Monitoring High-Level Radioactive Waste Settled Solids Surfaces for Indicators of Developing Deep Sludge Gas Release Events."

The goal of the test plan was to successfully measure and compare image resolution for a settled solids layer that was raised 9 mm in height in 1.5 mm increments to verify the sonar's ability to quantify the surface height and volume of solids. The procedural steps documented in the test plan include:

- Step 1: The flat plate will be added to create a flat floor in the 28-inch tall tank. The sonar will be hung from a structure component across the top of the tank. The sonar will be placed 12, 18 and 22 inches from the tank bottom plate.
- Step 2: A 3"-6" bladder will be mounted to a 16-inch diameter plastic lid. The lid will be filled with sand to allow it to sink when slowly lowered to the tank floor. The bladder will be equipped with an air tube and valve to allow air to inflate the bladder. Air will be added in very small increments to the bladder and sonar scans taken until the highest point over the air bladder image of the raised solids is 9 mm, with images taken in 1.5 mm increments.
- Step 3: The actual height of the solids surface will be measured for comparison to elevations found from the sonar data.
- Step 4: Sonar Image Resolution Test - Image a repetitive pattern to ascertain the resolution of the sonar for measuring height and lateral distances to determine the ultimate resolution of the sonar for measuring the volume of solids within its FOV.

Imaging systems are often tested with specific patterns with changes on the order of the imaging system's ability to resolve them. For a sonar with a 1% resolution (3 mm at 30 cm distance), FIU will develop an object with a pattern of rows and columns with height changes of 3 mm along the column and 5 mm from row to row. FIU envisions creating this test pattern object from plaster. Should the initial test pattern with 3 and 5 mm changes across adjacent cells prove to be unresolved with post processing of the sonar data, then the test pattern object for the 18 inch height test would be used. The ability to quantify the accuracy of the sonar to measure increases in volume in settled solids from entrapped gas is critical to allow site personnel to estimate the mass of this gas and its potential for becoming a DSGRE. In order to assess the ability of an imaging system to accurately image a surface and measure its volume, it is important to assess the imaging resolution across the field of view of the sonar and, therefore, images will be taken directly under and toward the edge of the field of view. Post-processing of these images will determine the ability of the sonar to accurately measure volume changes to the settled solids surface in the field of view. In these tests, as the changes in the height and width of the pattern

are decreased, the sonar loses its ability to see images at the edge of the field of view first and ultimately across the entire field of view. The human eye is able to discern a pattern in an image even if the pattern is “washed out” over 90% of the area of the image. FIU will directly image this patterned form on the tank floor. Should the object’s varying surface height changes not be resolvable, then another similar object with larger variations in the range between high and low points within each row will be used. Based upon accuracy of the imaging, a calculation will be made for the smallest volume change that can be imaged.

Experimental Setup

The experimental setup included the 3-D sonar mounted inside a plastic tank that is 28 inches in height and 23.5 inches in diameter (ID) with a floor that slopes downward in the center to allow liquid to be drained from the bottom. FIU obtained a circular aluminum plate that is 23 inches in diameter and created a flat floor surface in the tank. The tank with the plate inside and the sonar inserted and with sand covering a bladder was used. Sand to 3 mm thickness was extended beyond the 15.5 inch diameter plastic lid in order to fill the field of view with sand (i.e., for the 18 and 22 inch sonar heights).

RESULTS

The focus of research on this task this year was to address a new Hanford technical need for a technology that was able to image small increases in HLW volume across large tanks as an early indication of possible deep sludge gas release events. FIU investigated the ability of the commercial 3D profiling sonar to meet this need.

This past year, FIU completed the following:

1. Review of DSGRE reports and bubble imaging articles to develop a test plan.
2. Preliminary proof of principle testing. FIU tested the sonar to demonstrate proof of concept as well as to measure the sonar imaging resolution in order to better define the test plan.
3. Execution of the “Experimental Test Plan to Assess the Utility of 3D Sonars for Monitoring High-Level Radioactive Waste Settled Solids Surfaces for Indicators of Developing Deep Sludge Gas Release Events.”
4. Final testing of 3D sonar and image analysis algorithms. FIU’s development and testing of FIU imaging software.

Review of DSGRE and bubble imaging documentation

FIU reviewed reports and other documentation of deep sludge gas release events (DSGREs) as well as journal articles on acoustic imaging of gas bubbles and for monitoring gas buildup in solids in tanks. In addition, a successful preliminary proof-of-principle testing was completed, imaging pebbles and then the same pebbles with bubble wrap material underneath the pebbles.

The documentation reviewed included reports, data and other documents from Washington River Protection Solutions (WRPS) on the DSGRE Tall Column Project. The results of this project demonstrated that gas is not effectively retained in deep HLW sludge and this allowed waste retrievals that moved sludge to double-shelled tanks to safely continue.

Past research at Ames Lab and FIU has shown that the presence of over 1% gas entrained in the liquid phase can result in the complete attenuation of sonar signals (pings) traversing over 10 feet of liquid. This means that pulsed air mixing does not allow for sonar imaging. Other mixing processes that can entrain over 1% of air in the liquid continuously are likely to not allow for imaging also. It is envisioned that pulsed jet mixing would not entrain sufficient air to attenuate the sonar signal but this should be tested with an envelope of PJM conditions to ensure that this is the case. The concern identified by some Hanford personnel is the possibility that the continuous emission of gas from HLW might obscure or prevent imaging of the settled solids surface. The small size of bubbles and slow release rate make it likely but not assured that the sonar signal is not attenuated and that surfaces in HLW tanks can be imaged.

Bubbles have been imaged with other acoustic imaging systems. The acoustic signal undergoes a strong reflection when the media it traverses has a large spatial density gradient such as at a solid-liquid interface or a liquid-gas interface. It is not clear from results of others imaging bubbles that FIU’s sonar can or cannot image small bubbles.

Preliminary proof of principle testing

FIU used small pebbles and 6 mm thick sheet of bubble wrap to simply demonstrate the sonar's ability to image the increasing height of settled solids surfaces raised by gases. In the images below are the experimental configuration as well as some images from FIU's commercial sonar. Figure 41 (below left) is a photo of a 4.4 inch diameter dish holding small pebbles and a piece of bubble wrap. In the photo on the right, bubble wrap has been inserted under the pebbles, raising the surface 6 mm. Figure 42 is a photo of the dish-bubble wrap-pebbles inserted into the 3-ft diameter test tank with the 3D imaging sonar inserted 4 inches into the water.

Figure 43 is the commercial sonar image of the metal plate with the dish and pebbles on it. In this image, the field of view is 60 degrees which allows the entire plate and the bottom of the test tank to be imaged. The commercial sonar imaging software interpolates to fill in points not imaged which results in the loss of edges such as that of the metal plate. FIU's sonar data processing software provides a much improved image of sharp edges, steep rises and falls of the solids layer and has several filters to eliminate double scatters, reflections off entrained particles while mixing and more.

Figure 44 (left) is the sonar image of the dish with pebbles without the bubble wrap and on the right is the same setup but with the bubble wrap. Note that the field of view has been returned to 30 degrees.



Figure 41. Plate of pebbles for sonar imaging and bubble wrap (left) and bubble wrap inserted under pebbles (right).

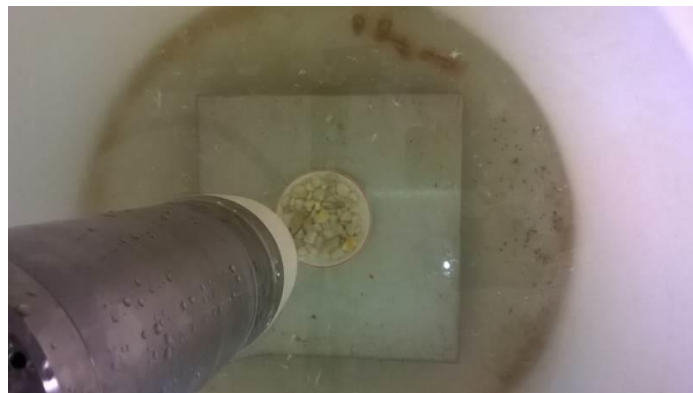


Figure 42. 3D Sonar in test tank directly above plate with pebbles.

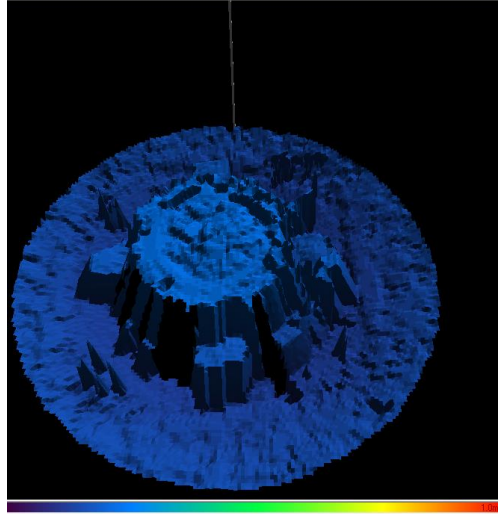


Figure 43. Sonar image of large metal plate with small dish of pebbles in the center.

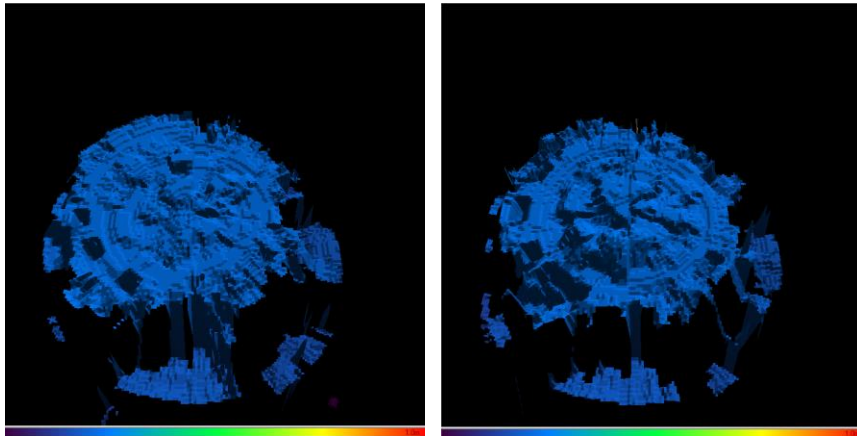


Figure 44. Sonar image of dish with pebbles on a large metal plate (left) and bubble wrap added to dish (right).

In Figure 44, both images show the flat metal plate and in the foreground is a drop off to the bottom of the tank. In the center of both images, the plate with the pebbles can be discerned although not with the resolution and symmetry possible with post processing. Note the major increase in the height of image of the plate and pebbles that results from adding 6 mm of height from the bubble wrap.

The preliminary testing did demonstrate that a solids surface (pebbles) could be raised by gas (bubble wrap) by a height as small as 6 mm and still be imaged by the sonar. The FIU post processing imaging provides better resolution than the commercial 3D sonar display software with ~ 1 cm height resolution.

Execution of the Experimental Test Plan

FIU next executed the test plan designed to test the 3D sonar's ability to measure small changes in the height of settled solids on a tank floor. The experimental setup included the 3-D sonar mounted inside a plastic tank that is 28 inches in height and 23.5 inches in diameter (ID) with a floor that slopes downward in the center to allow liquid to be drained from the bottom. A 23-inch

diameter circular aluminum plate was inserted in the bottom of the tank to create a flat floor surface in the tank.

An initial test was carried out with a lid filled with sand that was raised (closer to the sonar) in small 5 mm increments. The next test involved an air bladder with sand on it going from fully deflated to fully inflated. Finally, a test pattern object was imaged to provide the best measurement of the sonar's image spatial resolution. The sonar is limited to an ideal resolution of $\pm 1\%$ of the distance from the sonar to the object imaged according to its manufacturer.

In Figure 45 , a plastic lid filled with sand can be seen on the metal plate floor in the 28-inch high, 24-inch diameter test tank. Wires were connected equidistant along the outer circumference of the metal plate to allow for it to be lifted 1 cm at a time.



Figure 45. Photograph of plastic lid filled with sand on an aluminum plate on the tank bottom. The 3D sonar can be seen in the center top of the photograph.

In Figure 46, the 2D profile image of the 3D commercial sonar of the lid filled with sand is shown. Note that the distance to the sand in the center is 51 cm from the tip of the sonar.

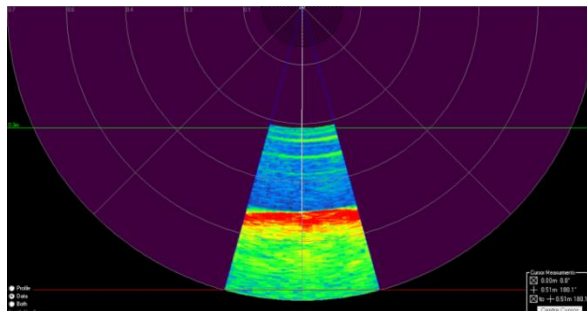


Figure 46. Baseline 3D sonar image of the lid filled with sand on the aluminum plate with 4 wires to raise the plate and the solids uniformly 1 mm at a time.

In Figure 47 the 2D profile image of the 3D commercial sonar of the lid filled with sand after it has been raised 1 cm is shown. Note that the distance to the sand in the center is 50 cm from the tip of the sonar. This matches exactly with the 1 cm that the entire lid of sand was raised. The accuracy of the cursor in this 2D image is ± 1 cm. Post-processing of the sonar's 3D data greatly improved the surface height measurements (mm resolution) and allowed for an estimation of the increase in height.

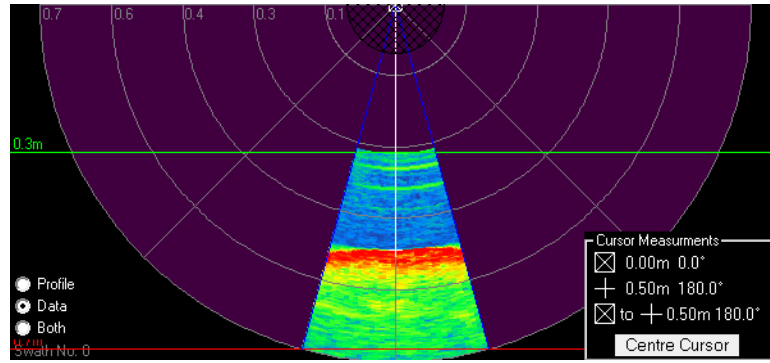


Figure 47. 3D sonar image of the lid filled with sand on the aluminum plate with 4 wires used to raise the plate and the solids uniformly 1 cm from the baseline position.

The next testing involved use of an air bladder with sand on top to see if the sonar could image small changes in the height of the sand as air was added or removed from the bladder. FIU directly imaged the sand layer as its height increased as air was inserted into the bladder. Preliminary testing inserted enough air into the bladder to raise the sand surface by 1, 1.5 and 2 centimeters.

FIU mounted an air bladder to a 40-cm diameter plastic lid with a 33-mm high lip and then loaded paving sand onto the lid to a depth of 33 mm at the edge of the lid and 57 mm in the center (fully deflated bladder). Figure 48 contains a photograph of the bladder mounted inside the lid (left) and the same bladder and lid with wet sand mounded over the bladder (right). The lid filled with sand sitting on a large metal plate at the bottom of the test tank is shown to the right.

FIU succeeded in completing a primary objective of this task by imaging a solids layer that is raised in 10 mm steps through insertion of air into a bladder under a solids (sand) layer. This directly mimics the rise in HLW solids from gas generation and retention in a deep sludge layer. The 10 mm resolution was not limited by the sonar but by coarse insertions of air in steps. The 10 mm resolution was achieved by putting sand over an empty bladder and adding increments of air to the bladder to raise the top sand layer center point by 10 mm and 20 mm and imaging the solids layer initially and after each increment of air.

The air bladder was taped to a plastic lid and weighted with flat metal pieces to keep it securely on the tank floor and not floating to the surface (Figure 48 left image). Paver sand was placed on the bladder and then smoothed over in order to ensure the sand would remain over the entire bladder even after addition of air while underwater. In Figure 48 (right image), the sand covers the bladder with a slight mounding.

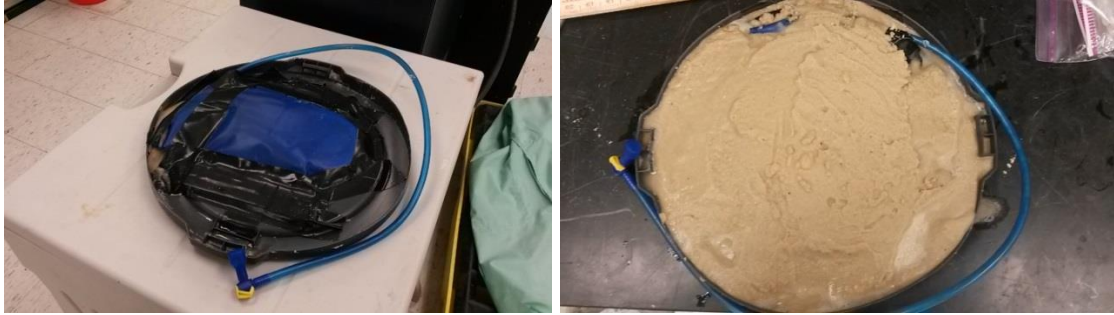


Figure 48. Air bladder with metal weights underneath taped to a plastic lid (left) and same object with paver sand on top (right).

In Figure 49, the 3D sonar images are shown with: no air in bladder (left); increment of air to raise center point of sand 10 mm (center); and 2nd increment of air to raise the center point of sand to 20 mm (right).

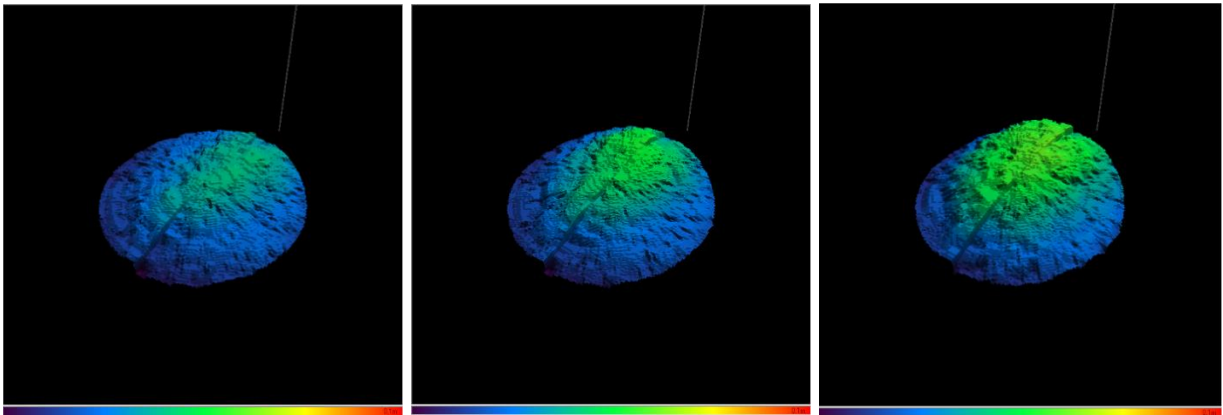


Figure 49. Three 3D sonar images are shown with: no air in bladder (left); with 1st increment of air to the bladder; and after 2nd increment of air to the bladder.

Once the sand with an empty bladder was imaged, air was added to the bladder in increments to simulate the rise in HLW solids with gas generation and retention in a deep sludge layer. Figure 49 clearly shows that changes as small as 10 mm can be easily imaged and measured by the 3D sonar. Measurements of the center sand point were taken with a yardstick with mm rulings to measure the 10 mm and 20 mm increases. Earlier tests adding 5 mm thick, flat metal objects into a stack one at a time, demonstrated that 5 mm changes in height can also be measured with the 3D sonar. Later testing finally identified the best resolution of the sonar for changes in the height of the solids layer was +/- 3 mm when the sonar was 12 inches from the surface.

Figure 49 (right image) shows the maximum amount of gas that was put into the bladder and the resultant height change was measured to be 20 mm. This proof-of principle test results were shared with WRPS scientists and engineers immediately after testing.

FIU processed images within MATLAB software to improve visualization of the settled solids layer on tank floors. FIU's goal on this visualization subtask was to improve the accuracy of the spatial dimensions of the wall locations, settled solids on the floor and any objects in the field of view. FIU discovered that by covering hard smooth objects with sand, the sonar signal has stronger reflections and that the sonar images were more precise, and that there was a reduced

need for filtering and processing the data from the sonar images. Actual high-level radioactive waste particles would be similar to the sand and not like the hard smooth objects imaged in earlier testing.

After a visit from WRPS personnel, the 3D sonar began giving anomalous results with excessive noise and imaging of the same objects results in very different images. Initial measurements were of lower quality than earlier this year and much worse than results for baseline cases taken in 2015. There was a major fraction of the sonar signal that appears to be scattered in the water around the sonar head where there should be no scattering. By using a delay before accepting a reflected sonar signal, we were able to filter out this anomalous scattering around the sonar. This anomalous scattering contributed to significant sonar signal strength being lost and, hence, to lowering the intensity of the scanning sonar.

The instrument manufacturer was contacted and troubleshooting was initiated. A loose connection in the main sonar cable was discovered and the quality of the data was greatly improved to that of earlier this year. In addition, the zero offset was optimized which resulted in much better matching of the sonar's image from swath 1 (first swath) and swath 200 (last swath, same swath but from the opposite direction). The manufacturer also recommended that the targets being imaged should be at least 33 cm (13 inches) away from the sonar. With the adjustments suggested by the manufacturer, the sonar was again in excellent running condition and FIU was able to resume execution of the test plan.

Having taken measurements with the air bladder in 1 cm steps with insertions of air, FIU then moved to measuring the deflated bladder and sand on top with much finer (1.84 mm) increments. Measurements were taken of sand over a deflated bladder for the initial measurements. This flat but slightly angled disc of sand was measured for 6 heights (45, 45.184, 45.368, 45.552, 45.736, and 45.92 cm). In Figure 50, the sonar in the tank and the disc of sand are clearly visible. In Figure 51, a 2D swath, a top view, and a 3D sonar image of this disc of sand are displayed.

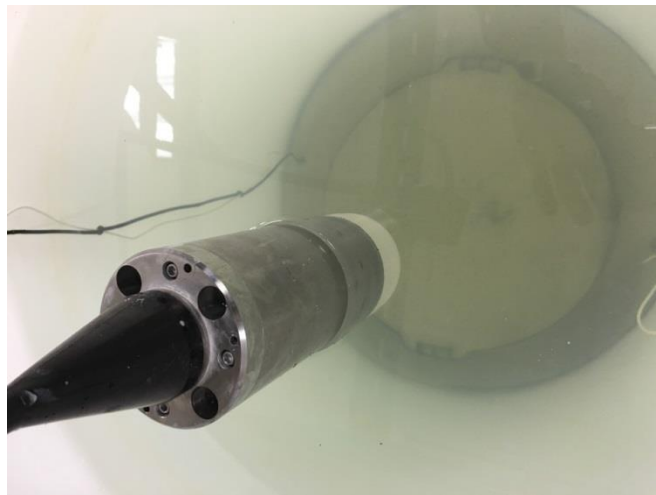


Figure 50. Photograph of sonar in the test tank and the target circular disc of sand.

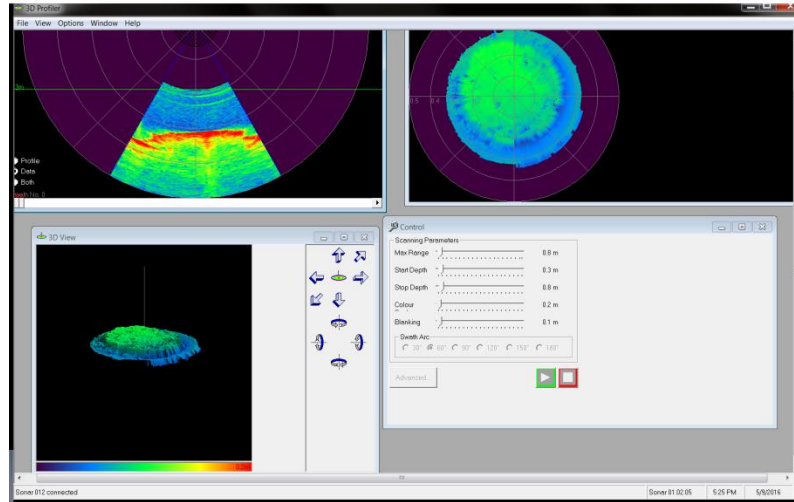


Figure 51. 2D, top view and 3D views of sonar imaging circular disc of sand at a distance of 45.92 cm.

It was important to measure the volume of the sand in the bottom of a tank from multiple heights. The accuracy of the sonar scales with the height from sonar head to the imaged target. While exact measurements of the highest sand surface over the bladder was measured with a measuring stick accurate to millimeters, the overall shape and volume of the sand for this experiment with the bladder was not well defined. In the initial test matrix it was planned to add 6 separate increments of air to the plastic bladder which proved to be too difficult to implement. In the final test matrix, the air bladder was either fully deflated, inflated 1 inch above fully deflated, or fully inflated (~1.5 inches higher than fully deflated). The original test plan called for measurements of 12 , 18 and 22 inches from tip of sonar head to solids surface directly below. It was determined that much better resolution (smaller steps) could be used in increasing the distance between the sonar and the solids layer. FIU changed from 4-inch step size to a 4-cm step size. The sonar height was modified by adding 1, 2 or 3 metal spacers (4 cm thick) under the sonar platform.

Table 6. Test Matrix

Height of highest point of sand over bladder	Initial Sonar height above base plate
57 mm (deflated)	31.0 cm
57 mm (deflated)	35.0 cm
57 mm (deflated)	39.0 cm
57 mm (deflated)	43.0 cm
82 mm (1 increment of air)	31.0 cm
82 mm (1 increment of air)	35.0 cm
82 mm (1 increment of air)	39.0 cm
82 mm (1 increment of air)	43.0 cm
94 mm (2 increments of air)	31.0 cm
94 mm (2 increments of air)	35.0 cm
94 mm (2 increments of air)	39.0 cm
94 mm (2 increments of air)	43.0 cm

Sonar images from the test matrix are shown below in Figure 52. Preliminary volume calculations have been done on the images. The sand in the plastic lid with a deflated air bladder is shown from 2 sonar heights differing by 4 cm.

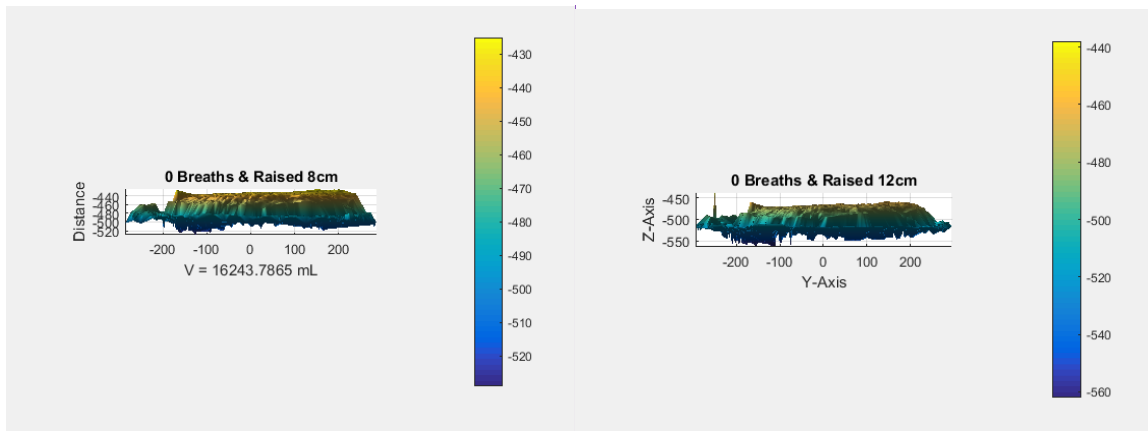


Figure 52. Images of same mound of sand with mounded sand atop but from 2 different sonar heights.

The sonar images below in Figure 53 were taken from the same sonar position in the tank but the sand above the bladder (highest point) differs by $\frac{1}{2}$ inch with the “2 breaths” being the fully inflated bladder.

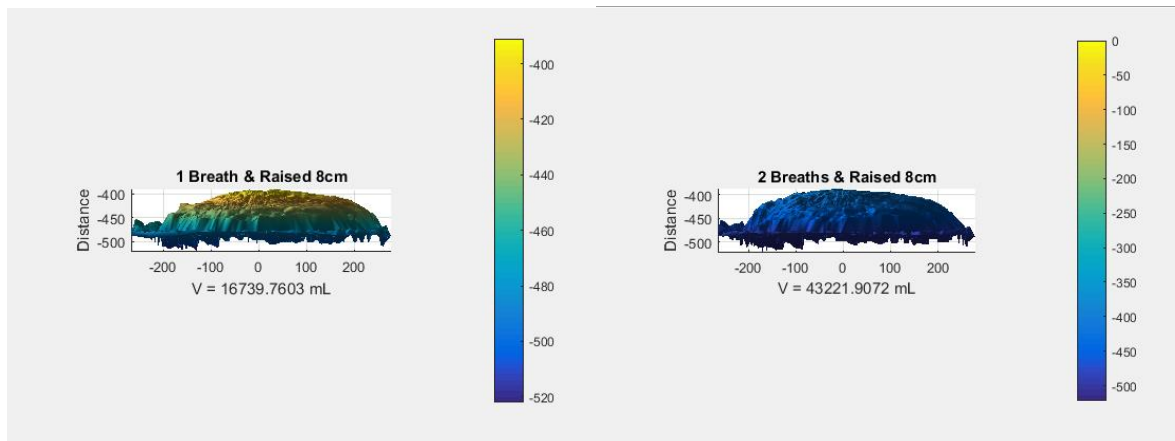


Figure 53. Images from same sonar height but with differing volumes in air bladder.

The volume estimation seen in the above Matlab images has been shown to be terribly incorrect and results from incorrect baselining of the $Z=0$ plane for the image. We will analyze this more below a special section devoted to volume estimation.

The final part of the test plan was to image a pattern in order to better determine the overall accuracy of the sonar for imaging settled solids volumes. The originally proposed linear test pattern was not effective and could not be imaged since the radial scans of the sonar failed to hit the features with enough pings. A test pattern involving concentric circles was used and was very effective since each sonar swath hit the various sand heights found in the test pattern shown in Figure 54. The height and diameter of each ring of sand was measured by ruler accurately to the millimeter. The sonar image of the object is shown in Figure 55.



Figure 54. Test object with circles of sand of varying heights and diameters measured to mm resolution.

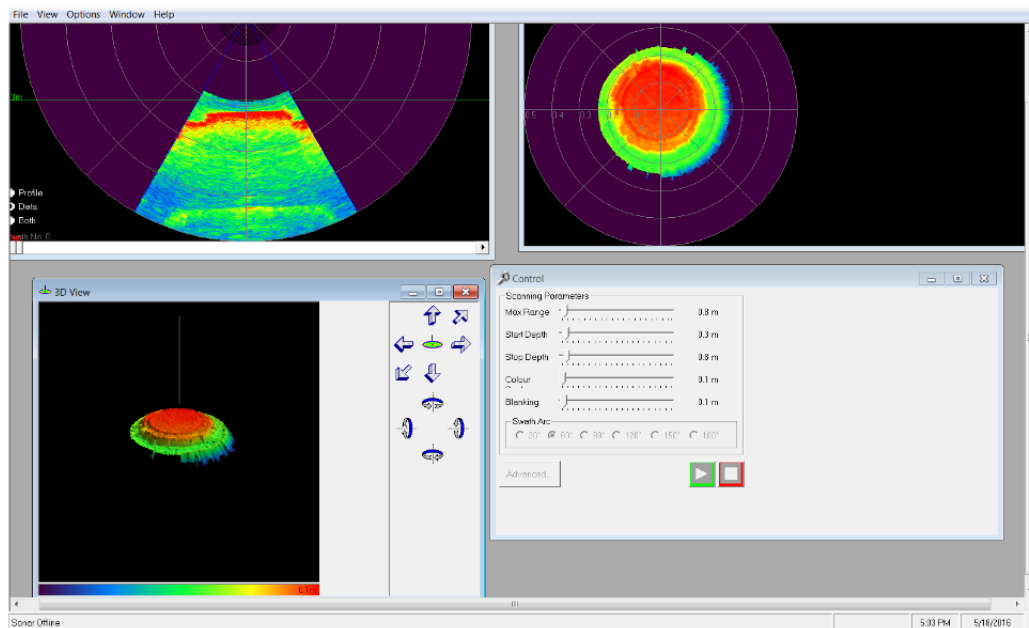


Figure 55. Sonar image of the circles of sand.

Note that there are 3 circular, metal rings of sand in the test object and only were able to be resolved (the green outer circle is the larger lid with sand). The lateral resolution of the sonar for an object directly below at a distance of 12 inches is less than an inch and greater than $\frac{1}{2}$ inch. Again the height resolution for this configuration is ± 3 mm.

In May 2016, the 3D sonar test plan was completed. This testing included sonar measurements on an air bladder under sand and a modified circular test pattern to determine the resolution and capability of the sonar for detecting small changes in the volume of settled solids in the field of view as a measure of possible gas retention in deep sludge layers.

Volume Estimation and Analysis of Volume Results

Development of software which approximates the volume of objects scanned has progressed to a point where a volume is very simply generated of the scanned surface. The algorithm in which the software processes the captured sonar data and displays it involves creating a triangular mesh between each and every point. Due to this meshing, a surface is created, in particular a convex hull, and, using the standard library functions provided by Matlab, the volume of the scanned surfaces is quantified and a differential volume is measured.

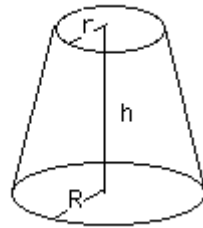
The accuracy of the volume calculation (Matlab Code) was shown to vary from below 5% to over 500%. Measuring the volume of objects with known volumes allowed FIU to diagnose that there was a problem with the baseline ($Z=0$ plane) being calculated automatically in the Matlab code. For measuring the volume of HLW in tanks and monitoring the solids surface for changes over time, a calibration will be needed to ensure proper baselining.

Analyzing the volumes shown in Figure 52 and Figure 53 for the image of the air bladder covered in sand in varying stages of inflation, very unreasonable values for the volumes are seen. The sonar images below show calculations of total volumes resulted in 14 to 50 liters of volume, which is much larger than the object being imaged. The differential volume between 0 and 1 breaths is 0.496 cm^3 or $\sim 1/2$ liter (Figures 52 and 53). This volume is within 10% of the 448 cm^3 that was roughly measured for the irregular surface.

The difference in volume of the system with 2 breaths of air in the bladder versus 1 breath was 26.5 liters versus the half liter between 0 and 1 breath. This very large value confirms that the volume measurement and its associated baseline are terribly incorrect and need correction.

In order to better understand and then correct the volume measurement, FIU has imaged several objects with specific volumes. The first object was a plaster mold created in a glass dish and was used to test the volume algorithm. The object has the shape of a frustum of a right circular cone, or sometimes labeled as a truncated cone.

The volume of a truncated cone is $V_{tc} = \pi \times h \times (R^2 + r^2 + R \times r) / 3$.



The dimensions measured are: $h=7\text{cm}$; $R=6.9 \text{ cm}$; $r=6.4 \text{ cm}$ yielding $V_{tc} = 973 \text{ cm}^3$. This compares well with the volume of the dish measured by liquid which yielded 946 cm^3 . See the photograph of the plaster object below in

Figure 56.



Figure 56. Plaster object used to test and correct volume calculation.

Figure 56 Photograph above shows the plaster object imaged. Figure 57 below is the sonar image of the object.

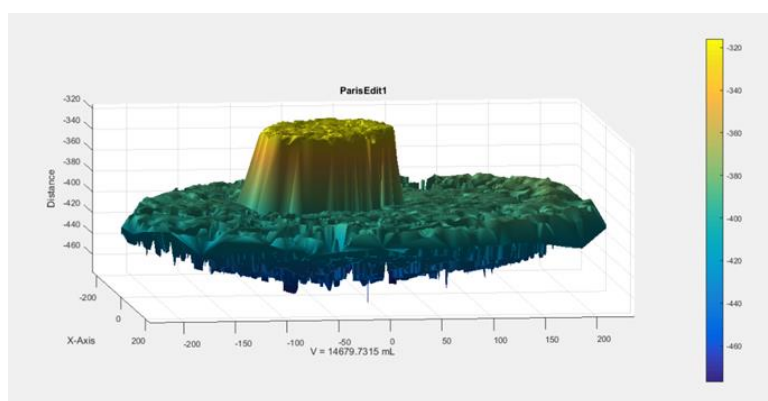


Figure 57. Sonar image of the plaster object used to help correct volume measurement.

The source of error in the volume calculation algorithm was further studied. Shown below in Figure 58 are 3 sonar images of objects (brick, plate and rings of sand) that we have imaged in the past. The volume of these objects were analyzed by the Matlab Code and shown to vary from below 5% to over 500%.

In the image below is a brick that was imaged in 2014 with the 3D sonar and shown in the commercial sonar image display software.

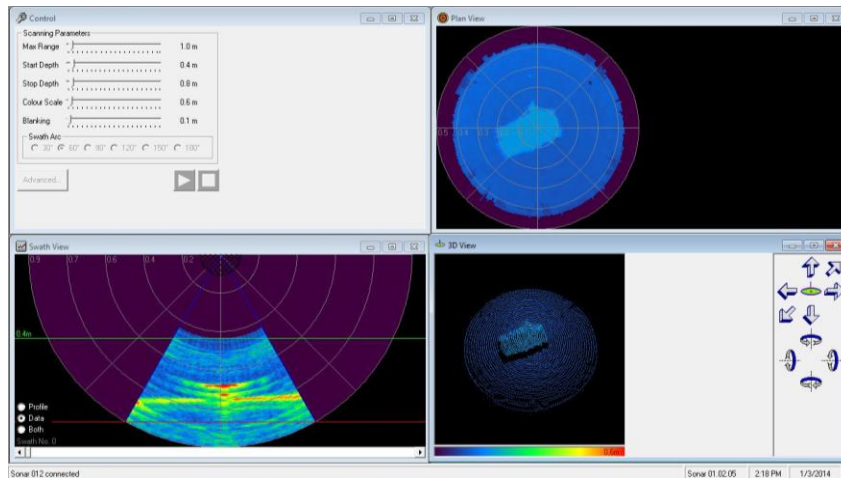


Figure 58. Sonar image of a brick in a test tank at FIU.

Finally, below in Figure 59 is an image of 3 metal rings filled with sand which showed great improvement in shape detection, height and volume measurements than with rectangular objects.

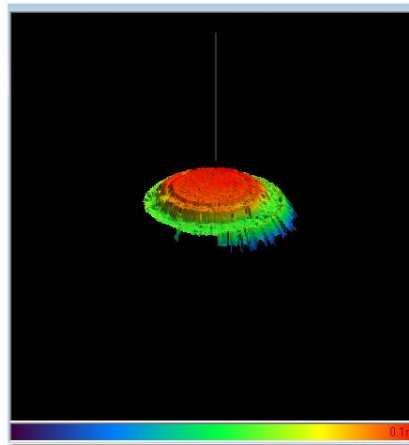


Figure 59. Sonar image of sand inside 3 concentric metal rings.

The rationale for developing the Matlab volume estimation algorithm was to decrease the error as measured by the 3D Mapper algorithm.

Below in Figure 60 is an image of a brick after filtering to remove sonar ping scatters off floating particles which result in false volume shown as tall, sharp peaks.

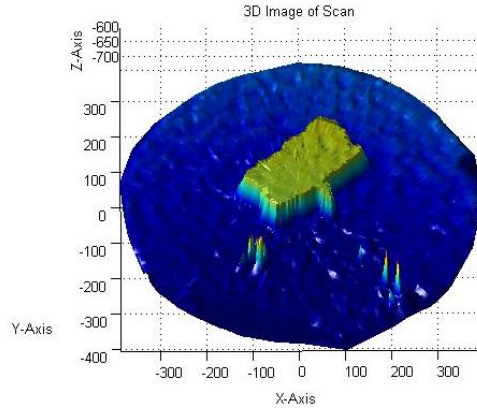


Figure 60. Filtered and post-processed sonar data of brick on a tank floor.

Imaging of this brick with the 3D Mapper is shown below in Figure 61.

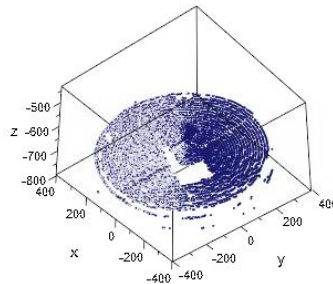


Figure 61. Sonar image of tank floor with a brick in 3D mapper.

In March 2014 we reported that the volume calculations of the 3D Mapper was often 4-6% for high resolution (e.g., 200 2-D swaths that take 40 seconds to collect) whereas the volume was 7-9% overestimated when rapid scanning was used with 6 to 20 swaths. This error arises due to the interpolation of the objects between swaths. Volume errors were larger with object with sharp corners and edges like bricks, and smaller (2-5%) for smooth, slowly varying shapes such as settled solids in tank bottoms.

The impetus for using the Matlab volume calculation algorithm was originally related to having more accuracy for rapid scanning of settled solids on mixing tank floors. This is a separate need from the Deep Sludge Gas Release Events (DSGREs) need currently being addressed. It is expected that the Matlab algorithm would yield more accurate volume calculations than the 3D Mapper when proper baselining of the $Z=0$ plane is implemented. For flat floors with an object and no sand, the Matlab algorithm calculates volume to better than 3%. In imaging real tank floors with settled solids, this baseline issue can result in large volume errors as described above (5-500%).

CONCLUSIONS AND FUTURE WORK

FIU's 3D commercial profiling sonar that is highly resistant to nuclear radiation and high pH (pH>14) was tested for its ability to accurately (± 1 cm) image settled solids layers on the floor in high-level radioactive waste (HLW) tanks to being able to accurately measure small changes in the height of settled solids which could be an indicator of gas accumulation in deep sludge layers in HLW tanks.

The 3D sonar was shown to have a height and lateral resolution of ± 3 mm for a settled solids surface located ~ 12 inches from the sonar head. The sonar can be deployed into HLW tanks via a 4-inch riser. FIU can successfully measure the height of settled solids in tanks even with ongoing mixing of solids in the tank by looking at 2D image from commercial sonar and by post-processing sonar data to remove sonar signals from extensive scattering off suspended particles and leaving the solids layer on the tank floor.

In addition, FIU has developed a post-processing sonar imaging algorithm that does an excellent job in image analysis. Similarly, FIU has excellent data filtering algorithms to eliminate sonar ping reflections off entrained solids or from double scattering from 2 surfaces. Finally, the 3D Mapper algorithm was shown to be effective and can be used for imaging tank settled waste for DSGREs at Hanford. When the correct baselining of the Matlab volume estimation is completed at some future date, it should be used instead of the 3D Mapper since it should be able to achieve $\pm 4\%$ volume accuracy.

This task is completed and will not continue into FIU Performance Year 7. Hanford Site engineers have stated that the SLIM technology is not needed until 2018 or 2019 and is not a high priority for 2017.

SLIM is ready to be tested in the Cold Test Facility at Hanford and then deployed in HLW tanks. It can be effective at the first 3 of the below 4 technology needs at Hanford:

1. Able to deploy into double shelled tanks via 4-inch risers to determine the height of the settled solids layer in the tank to ensure it remains below a maximum allowed height for safety.
2. Able to deploy into single or double shelled tanks via 4-inch risers to optimally position pumps used to empty the tank without allowing the pump to plug with sludge.
3. Able to deploy into conditioning or mixing tanks to rapidly image the tank floor to ensure pulsed jet mixers (PJMs) effectively suspend and transport all solids.
4. Able to deploy into HLW tanks to precisely (± 3 mm) monitor the height of the settled solids layer across the entire tank to ensure that gas is not being retained in the waste that might lead to Deep Sludge Gas Release Events (DSGREs).

The volume estimation algorithm would be needed along with in-tank maneuvering in order to meet need for real-time monitoring for DSGREs. Finally, the first 3 needs would require SLIM to be deployed for a limited time in the HLW tanks. Longer deployments in HLW will result ultimately in sonar failure due to radiation damage despite its split head design being somewhat radiation hardened.

REFERENCES

1. Understanding Gas Release Events in Hanford Double Shell Tanks, Perry Meyer & Beric Wells, Pacific Northwest National Laboratory, Waste Management 2000 Symposium, February 27 – March 2, 2000, Tucson, AZ.

TASK 18.2

DEVELOPMENT OF INSPECTION TOOLS FOR DST PRIMARY TANKS (FIU YEAR 6)

EXECUTIVE SUMMARY

In August of 2012, traces of waste were found in the annulus of the AY-102 double-shell tank (DST) storing radioactive waste at the Hanford DOE site, prompting the need for developing inspection tools that can identify the cause and location of the leak. To help in this effort, Florida International University (FIU) is investigating the development of inspection tools able to access the tank's secondary containment, while providing live visual feedback. This effort has led to the development of two inspection tools: a magnetic wheeled miniature motorized rover that will travel through the refractory cooling channels under the primary tank, and a pneumatic pipe crawler that will inspect the tank ventilation header piping. Both inspection routes lead to the central plenum under the primary tank.

The magnetic wheeled miniature tool is a remote controlled rover with four wheels directly driven by independent micro DC motors. The tool is being designed for highly radioactive environments, and does not house any embedded electronics other than the camera. The inspection path consists of approximately 38 feet of channels, as small as 1.5 inches by 1.5 inches, and it includes several 90° turns. To avoid debris, the device will travel upside down magnetically attached to the bottom of the primary tank.

The pneumatic pipe crawler is a worm type robot with a modular design, composed of interchangeable cylindrical modules connected with flexible links. The design is an evolution of previous peristaltic crawlers developed at FIU, and uses pneumatic actuators to emulate the contractions of the peristaltic movements, which is suitable for highly radioactive environments by not requiring embedded electronics. The inspection path consists of approximately 100 feet of piping from grade, down through one of the drop legs and then lateral to the center bottom of the tank secondary containment. The route consists of pipes with 3 and 4 inches in diameter, reducers and several elbows.

Functional prototypes for both inspection tools have been successfully designed and tested at FIU. The tools were tested in bench and full testbeds. FIU's staff is in routine communication with the site engineers, providing a valuable resource for necessary modifications.

INTRODUCTION

In August of 2012, traces of waste were found in the annulus of the AY-102 double-shell tank storing radioactive waste at the DOE Hanford site, prompting the need for developing inspection tools that can identify the cause and location of the leak.

Figure 62 shows three possible entry points for inspection in the AY-102 double-shell tank:

1. the refractory air slots through the annulus,
2. the leak detection piping, and
3. the ventilation header piping.

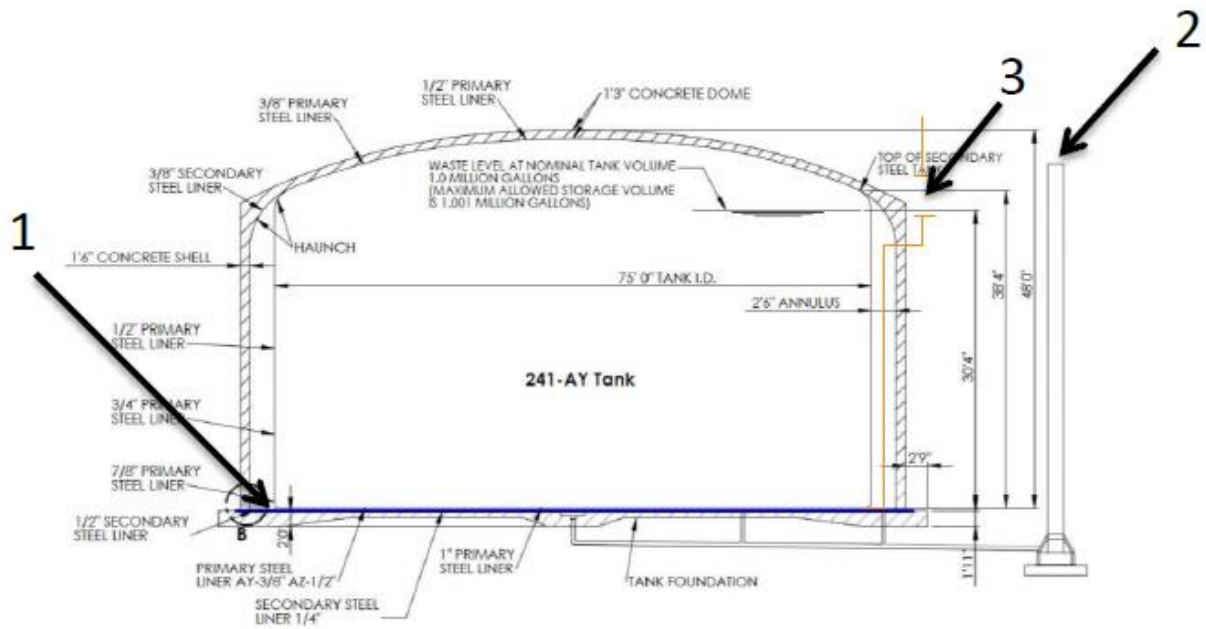


Figure 62. Inspection entry points of the AY-102 double-shell tank.

To assist in this effort, Florida International University is investigating the development of inspection tools able to access into the tank secondary containment, while providing live visual feedback. The effort led to the development of two inspection tools:

- a *magnetic miniature rover* that will travel through the refractory air slots, and
- a *pneumatic pipe crawler* that will inspect the ventilation header piping.

The objective of this task is to develop inspection tools that will assist site engineers at Hanford understanding the health of the DSTs and assisting in identifying the source of the material entering Tank AY-102 annulus space.

MAGNETIC MINIATURE ROVER

Background

FIU is developing a technology that will access the primary tank floor of DSTs at Hanford through the annulus and refractory air slots (Figure 63) and provide visual feedback of the condition within the air slots. The refractory air slots range from 1 inch to 3 inches in width and provide a complex maze to navigate through, including four 90° turns to reach the center of the tank (Figure 64). Pictured is documentation on AY-102, a tank possessing one of the more difficult inspection paths due to the layout of the refractory cooling channels; other double-shell tanks contain channels whose layouts resembles a web structure with much larger angles at the turns rather than the sharp 90° turns.

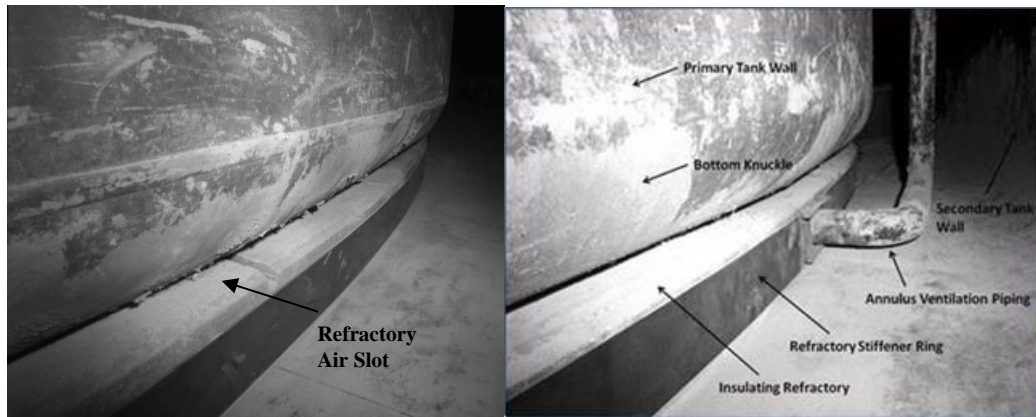


Figure 63. Side view of primary tank and refractory air slot.

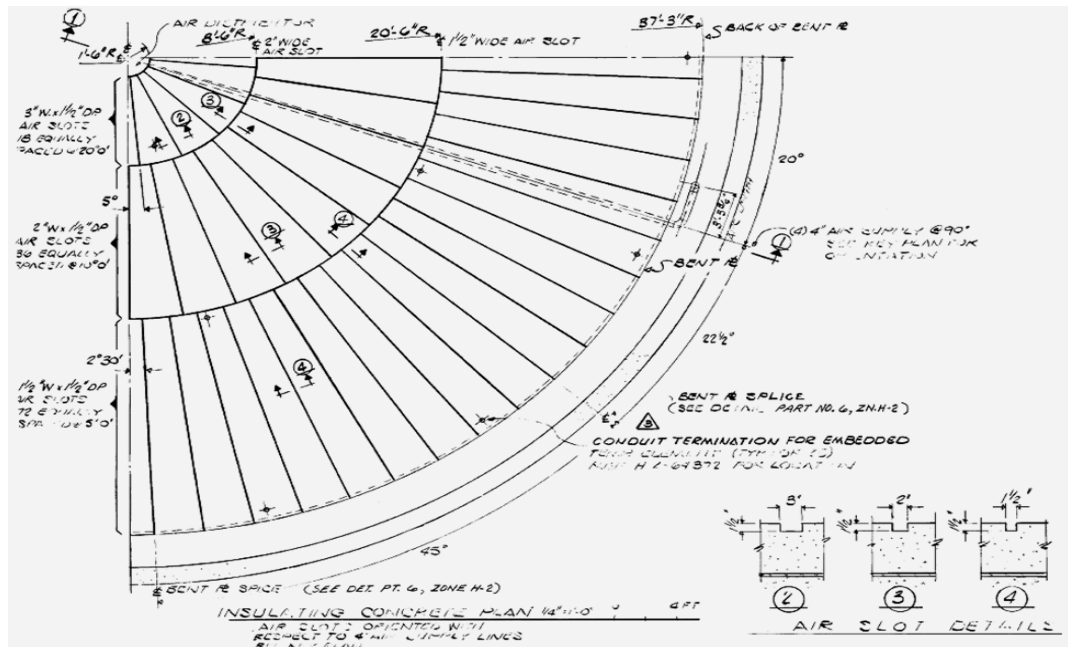


Figure 64. Refractory air slot layout and description for AY-102.

In conjunction with site engineers, FIU has gathered information that has been used to establish the design specifications for the inspection tool. This includes annulus and refractory air slot geometry and maximum temperature and radiation limits for the device. Discussions with the engineers on the condition of the carbon steel along the tank bottom led to the viewing of refractory air channel video inspections for tanks AW-101, AZ-102, and SY-103 that were performed ten years ago with an articulated robot inside the annulus. The video provided FIU with a general idea of the conditions that will be encountered in the air channels, as well as the primary tank bottom surface condition. The video also provided FIU with a better understanding of the refractory pad's low shear strength and how easy it is to create debris (Figure 65).

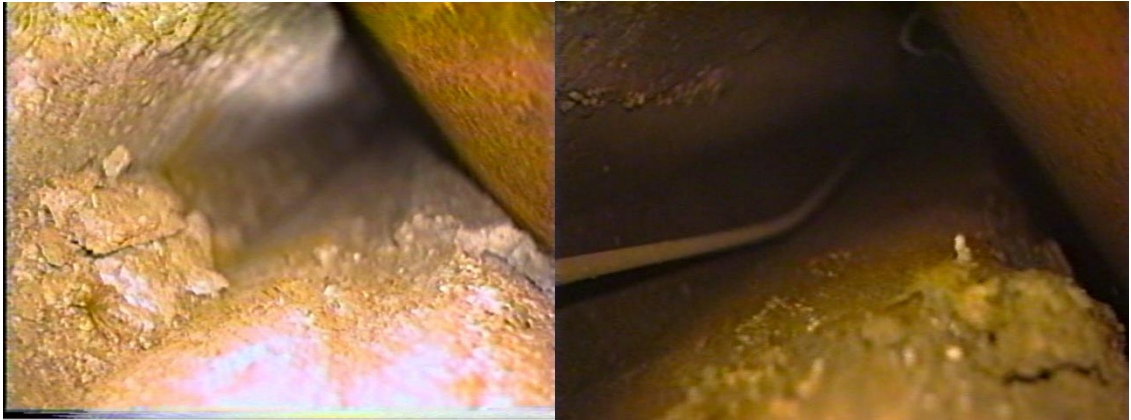


Figure 65. Debris seen in refractory air slots.

Design Concept

A prototype inspection tool was initially designed and the proof-of-concept was validated via bench scale testing. Various design modifications have been implemented after a number of bench scale tests. Efforts in improving the design have been focused on minimizing the complexity of the design while retaining efficiency.

The previous design iterations served as a platform upon which modifications were introduced after observations from its performance during the testing. Figure 66 shows the previous design iteration. Several changes were included in this design which provided notable improvements in operation of the inspection tool. Most notably, this design transitioned to a more modular fashion of component installation; this allowed for a much easier reassembly of the inspection tool. Additionally, the wheels were changed from off-the-shelf components to wheels that were 3D printed in-house. Transitioning to these wheels allowed for more flexibility in the wheel design, allowing for larger wheels providing more clearance, and thinner wheels allowing for a design with a reduced total width.

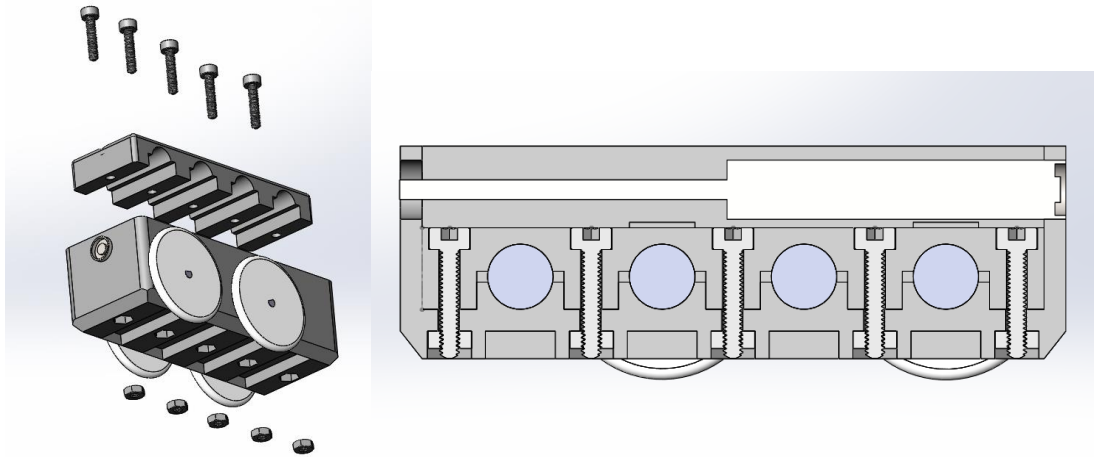


Figure 66. Exploded view of previous design iteration.

The previous design iteration was tweaked to maximize the design potential by including a cover to shield the internal components and enclosing the tether with an expandable braided sleeve. This sleeve both protects the internal cables from the environment and minimizes the size of the collective cables to reduce the tether drag force. Additionally, the material of the sleeve has a lower coefficient of friction compared to the rubber insulation of the bare cables, contributing to a lower overall tether drag force. The final state of this design iteration is shown in Figure 67.



Figure 67. Assembled model of the inspection tool.

With a final design iteration in the aforementioned configuration achieved, both valuable improvements and areas of needed improvement were observed. One of main areas for needed improvement was for the wheels that encuring notable damage under prolonged heavy use. This was due to the moment caused by the magnetic force, combined with the transverse loads experienced when turning the rover while the wheels remained straight at all times. These strenuous and cyclic loads took a toll on the narrow wheels and while the wheels were able to withstand the static loading, the cyclic loading experienced during stress testing induced damage that affected the inspection tool performance. This critical observation was addressed in the following design iteration shown in Figure 68. Previously, the inspection tool wheels were designed as narrow as possible to minimize the width of the tool but with these detrimental

cyclic loadings in mind, the width was increased, which also provided room to install a heat-set insert to allow for the wheels to be held to the shaft via a bolt. The wheels also relied on a press fit to attach to the motor shafts; however, the material was not able to sustain the cyclic loading and over time the press fit became less reliable. To allow for an increase in wheel width, any unnecessary space observed in the inspection tool was removed, and cavities in the body were created to allow for a more ergonomic wire management within the inspection tool.

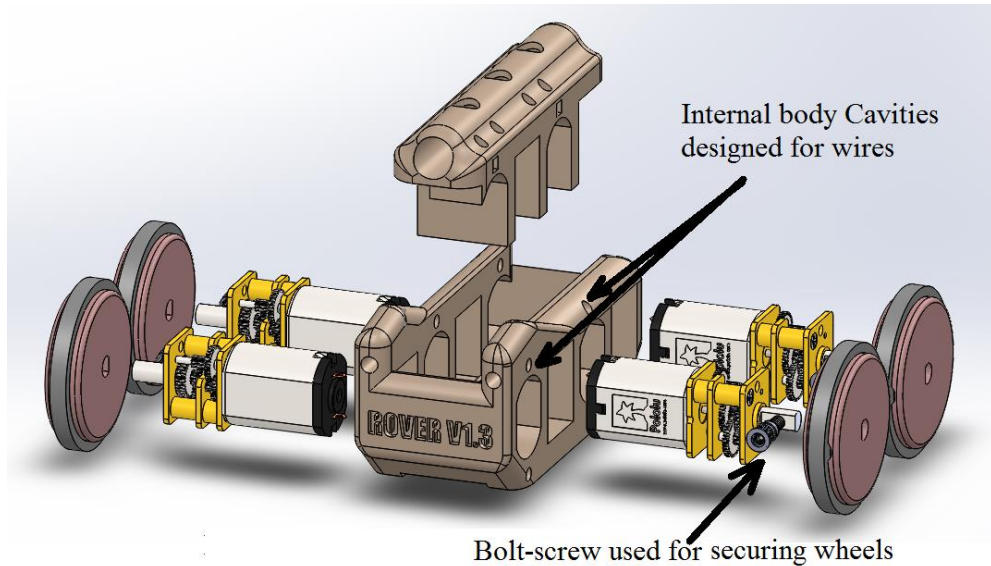


Figure 68. Exploded view of the current design of the inspection tool.

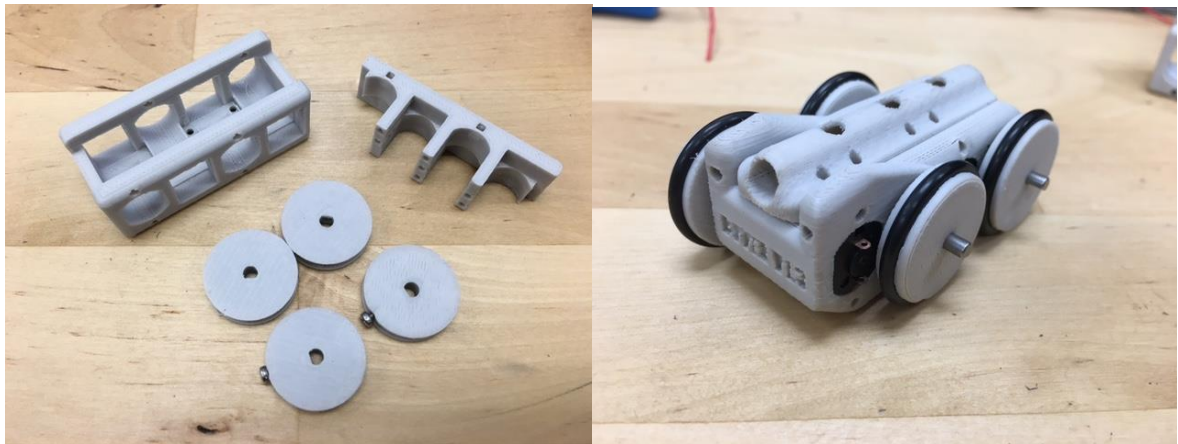


Figure 69. 3D printed components (left), assembled inspection tool (right).

A cable management system is necessary to provide a tangle free means of storing/supplying the tether for the inspection tool. A first prototype of the cable management system was developed with a stepper motor as the primary driving force. A timing belt is used to coil the tether around its base and can adjust the gear ratio of the system (Figure 70).

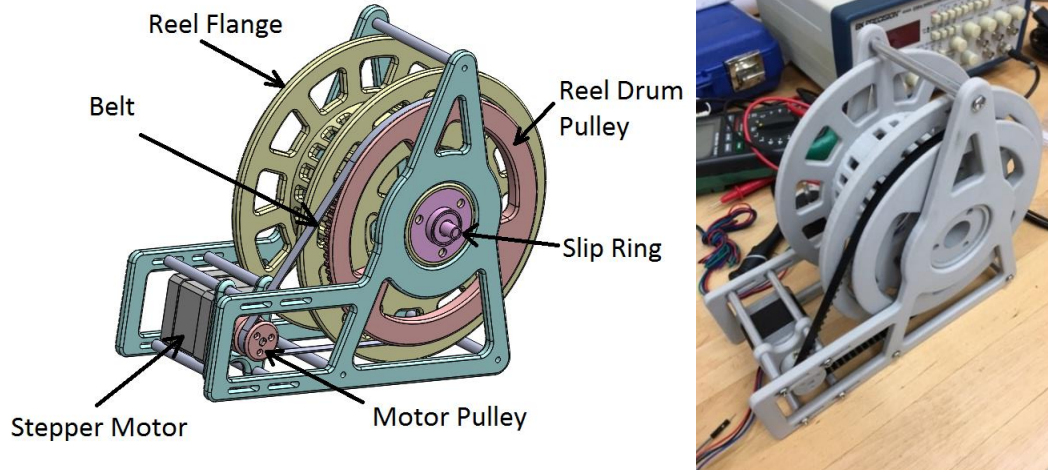


Figure 70. Cable management system for inspection tool.

Experimental Testing

The magnetic force provided by the magnets is of great interest due to its heavy influence in the inspection tools performance. The magnetic force must be balanced, as too strong of a magnetic force can negatively affect the inspection tools performance, as can too weak of a magnetic force. The current motors used in the inspection tool provide enough power such that the bottleneck is no longer the motors, but converting the power delivered from the motors into translational motion of the inspection tool; the characteristic which this depends upon is the traction force. As shown in the equation below, the traction force is directly proportional to the normal force at the contact point between the wheel and the surface.

$$F_{traction} = \mu_{friction} * N$$

However, the force due to rolling resistance is also directly proportional to the normal force, as shown in the equation below.

$$F_{rolling\ resistance} = \mu_{rolling\ resistance} * N$$

The influence of the rolling resistance is two-fold, as it is to be considered for both the added load on the motors when moving forward, as well as the resistance in the event that the inspection tool is pulled out of the channel via the tether. Manufacturer provided data includes the normal force provided by the magnets when there is no separation between the magnet and the surface; however, in this application, there will be a separation. Understanding how the magnetic force is related to the separation is crucial for magnet selection, as a balance must be struck between having sufficient traction and minimizing the force of the rolling resistance. Experimentation was performed on the magnets to determine the relation between the distance and the magnetic force. The test apparatus and results are shown in Figure 71.

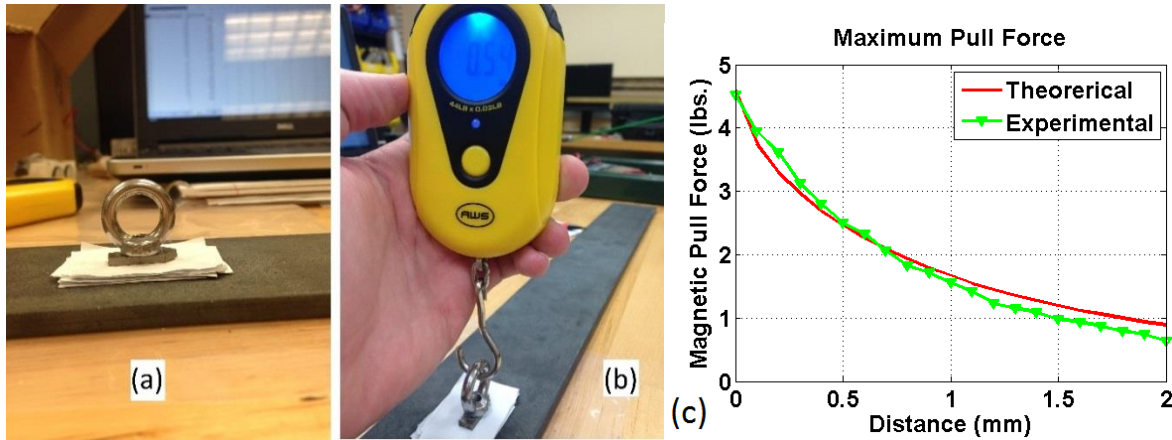


Figure 71. Magnetic force testing and results.

For the miniature rover, testing and validations were also conducted with the objective of verifying the navigation of the inspection tool on curved surfaces. To date, the navigation of the inspection tool has only been verified on flat surfaces. These tests demonstrate the potential of the rover to provide inspections in carbon steel pipes as well as refractory channels.

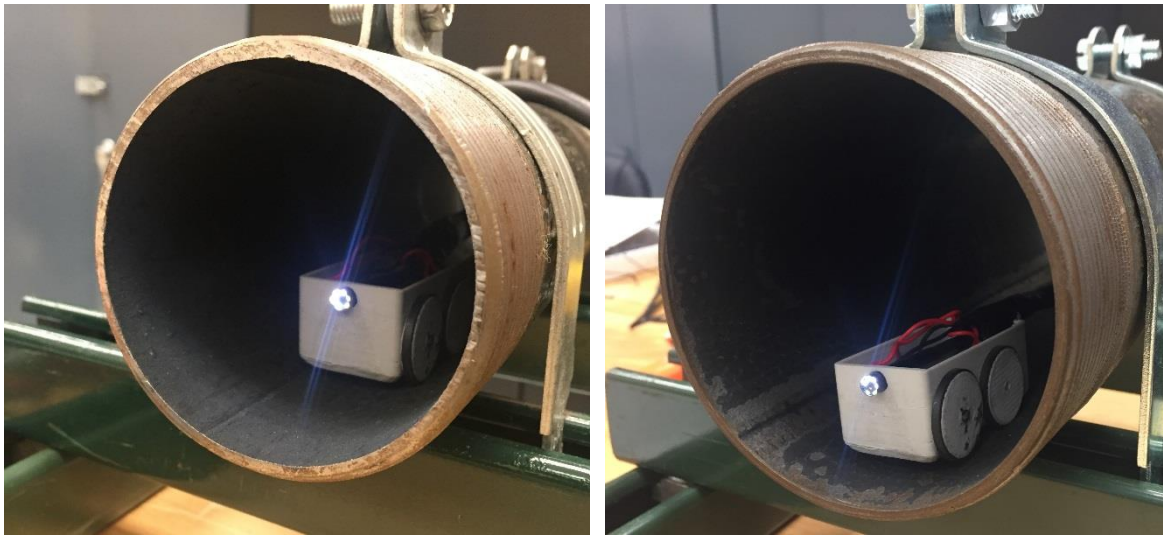


Figure 72. Inspection tool tested inside a (a) 3" and (b) 4" pipe bench scale.

While the main objective of this tool is to travel through the refractory cooling channels, versatility and robustness is a desirable trait. In an effort to test the inspection tool outside of its intended environment and test its versatility, it was tested within a 3" and 4" pipe. In this environment, the inspection tool will be subject to curved surfaces and increased distance from the magnet to the surface. Two tests were performed in this environment: a test of its ability to maneuver and a magnetic force pull test. The first test, simply maneuvering through the curved surfaces, proved to be successful in a limited scope; the reduction in magnetic force had a clear impact on the inspection tools ability to traverse the environment, but it was not significant enough to keep the unit from completely navigating through the pipe. As shown in Figure 73, the spacing between the magnet and the surface is 2 mm on a flat surface; however, that distance is nearly doubled in a 4-inch pipe, and more than doubled in a 3-inch pipe. The result of the pull

force test in the 4-inch pipe was 1.44 lb. This means that there was an individual pull force of 0.36 lb. for each of the four magnets. This value is equivalent to the pull force on the flat surface with an air gap of 3.75 mm. In the case of the 3-inch diameter pipe, an overall value of 1.06 lb. was measured. This correlates to 0.26 lb. equivalent to the pull force on the flat surface with an air gap of 4.45 mm. Navigating in the concave internal surface of the pipes increases the air gap and reduces the magnetic adhesion. For the 3-inch diameter pipe, 88% of the adhesion force is lost due to the increase in the gap compared to flat surfaces. For the 4-inch diameter pipe, 59% of the adhesion force is lost.

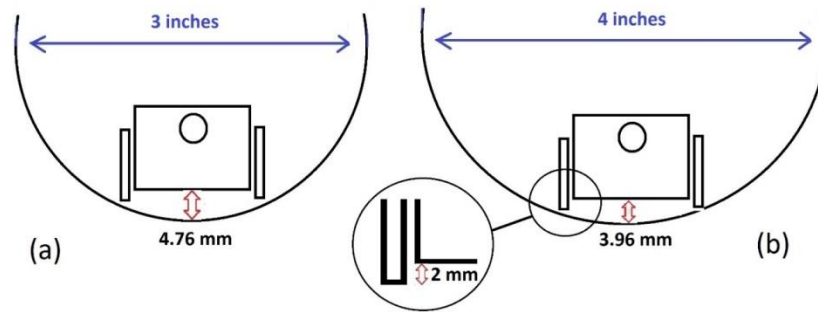


Figure 73. Magnet to surface spacing in various sized pipes.



Figure 74. Inspection tool testing in pipes.

Following the narrative of pipe navigation testing, the miniature rover's performance was also evaluated using pipes with internal corrosion. This test was conducted inside five steel pipes that were 20 feet in length and had 3 inch diameters. The 5 pipes that were used for the testing are shown in Figure 75. Similar to the initial bench scale tests, the magnetic force and pulling capability of the inspection tool was significantly decreased. However, the tool was able to navigate through the 20 ft. pipes. Significant debris did build up on the magnets (Figure 75) but this did not significantly affect the maneuverability of inspection tool. Another notable issue was the weight and drag from the tether which applied a moment on the body of the device and prevented the inspection tool from navigating in a straight path; this is an observation that may be addressed with a tether management system.

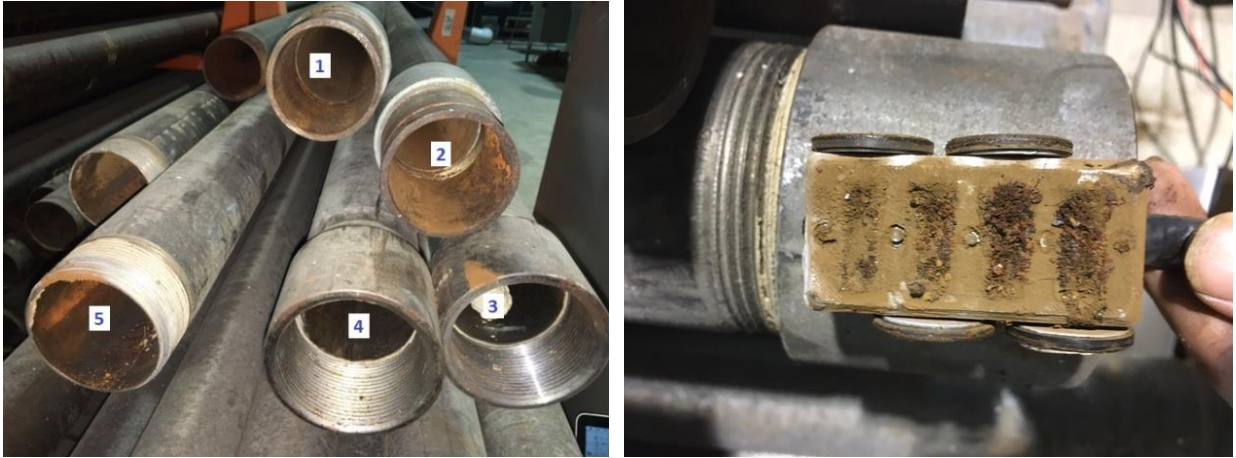


Figure 75. The corroded pipes used for navigation test b) debris build up on the magnets after 100 feet of navigation.

Another form of stress testing the inspection tool and placing it in imperfect environment was to attempt to navigate across large gaps; this serves as a simulation of the inspection tools maneuverability across a surface that may have cracks, inundations and any other surface imperfections. Testing was conducted over two separate pieces of steel plates aligned using a clamp. A gap was created by separating the steel plates from each other (Figure 76) with an initial gap of 1 mm. After each successful test, the gap was increased. The maximum gap the inspection tool was able to overcome was 28.02 mm, almost half of length of the inspection tool (62.98 mm).



Figure 76. Test set up for navigation over a gap.

For the miniature rover, FIU developed a new test set-up that can measure the pull force of the tether in with more realistic materials and coefficients of friction. The test bed included 17 feet of the 1.5 in. by 1.5 in. channels and two turns, one 90 degree turn at the end of channel and another turn 8 inches away. Figure 77 shows the test bed which was constructed using brick pavers to provide more realistic friction forces.



Figure 77. Laboratory scale test bed created for determining the pull force created by tether.

Measurements of the current tether pull force provided a range from 2.8 to 4.4 lbs. When a smoother cable, such as a standard 13 wire cable with an insulated jacket was utilized, the average pull force was about 1.2 lbs. Since the geometry of the current inspection tool does not allow for 90 degree turns, the tool was manually placed after the first turn and on average was able to navigate 4 inches after the first turn. Figure 78 displays the results of this testing.

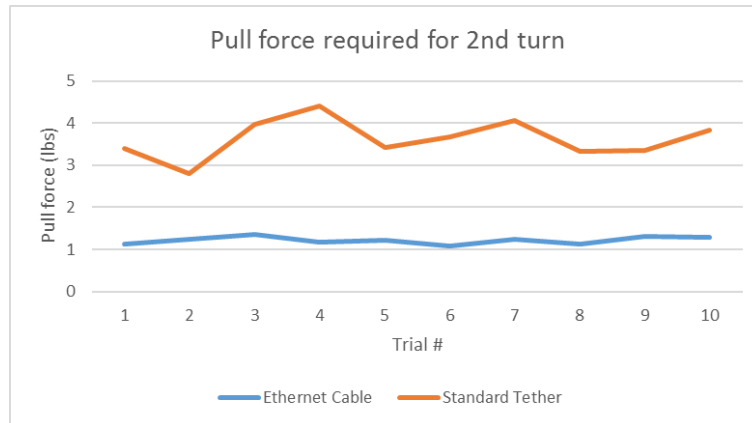


Figure 78. Comparison of the tether pull-force inside the test bed.

PNEUMATIC PIPE CRAWLER

Background

The pneumatic pipe crawler is an inspection tool designed to travel through the air supply line, leading to the central plenum of a typical DST at Hanford, and to provide live video feedback. For AY-102, the proposed inspection path is approximately 100 feet from grade, down through one of the drop legs, and then lateral to the center bottom of the tank secondary containment, as sketched in Figure 79 below. The route consists of all welded schedule 40 pipes (which are 3 and 4 inches in diameter), reducers and several elbows. The four drop legs branch from the “header ring” with a diameter of 3 inches, transitioning then to 4 inches.

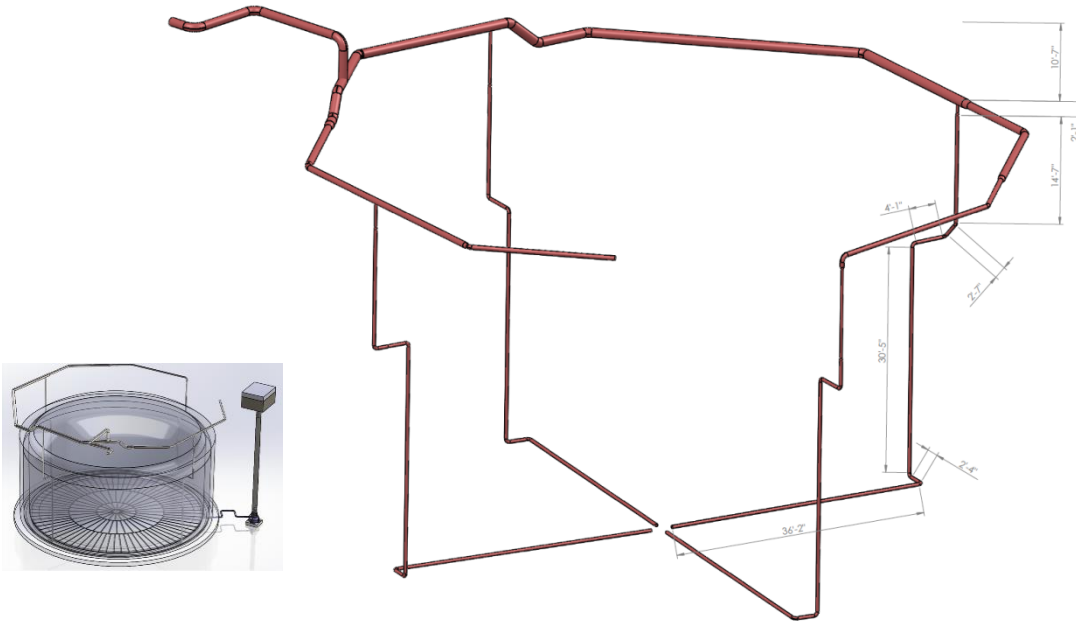


Figure 79. AY-102 air supply lines.

The inspection route to the central plenum through the air supply lines has the following requirements:

- Crawl through pipes and fittings (3" and 4" diameter)
- Climb vertical runs
- Tolerate elevated temperatures (170 °F)
- Tolerate moderate radiation levels (85 rad/hr)
- Provide a means for removal in the event of a malfunction

Additionally, the crawler will need to provide live video feedback as required; however, plans for carrying additional instrumentation are being investigated.

The current design for the pipe crawler is a worm type robot with a modular design, composed of interchangeable cylindrical modules connected with flexible links. Figure 80 shows a rendering of one of the more recent designs of the system.

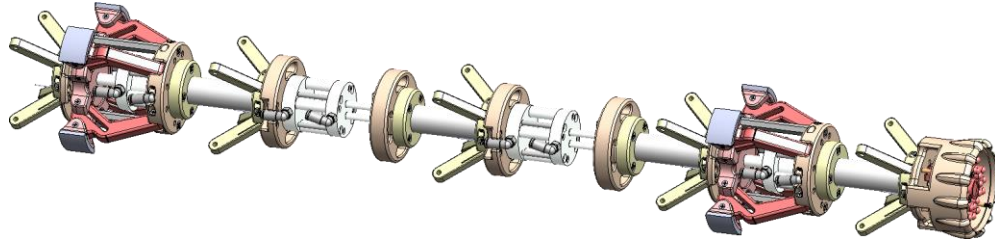


Figure 80. FIU's pneumatic pipe crawler.

Design Concept

The design is an evolution of previous pipe crawlers developed at FIU (Pribanic, 2013). The tool inherits the idea of using peristaltic propulsion, powered by pneumatics, and includes an innovative design with a modular approach that utilizes off-the-shelf pneumatic actuators to produce the contractions of the peristaltic motion.

A pneumatic powered crawler is suitable for highly radioactive environments with potential exposure to flammable gases. The locomotion system does not require embedded radiation hardened electronics and electric actuators. The design is also inherently ignition proof, since pneumatic actuators are not likely to produce electric sparks common in some electric motors and actuators.

In addition, a peristaltic propelled crawler offers an appropriate design for decontamination. As illustrated in Figure 81 below, the device can navigate inside a pipeline without using any external moving parts, such as wheels and continuous tracks, which could be designed to be fully encapsulated in a disposable elastic skin. In extreme cases, the crawler itself can be considered disposable, due to its affordable design.

Another design advantage is associated with its modular design, which has the potential to be customizable. Other specific tasks could be accomplished with the addition of extra modules, such as instrumentation, material sampling, and pipe repair.

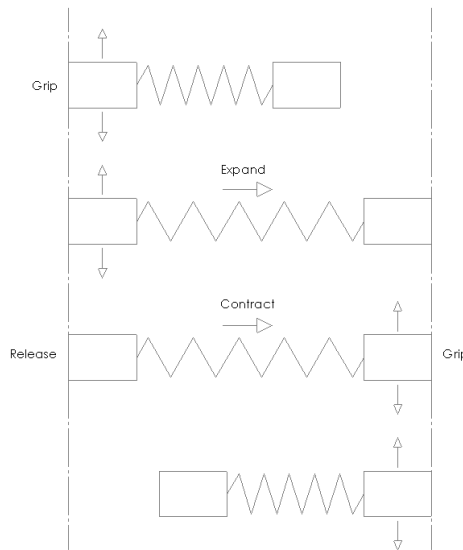


Figure 81. Peristaltic locomotion.

As shown in Figure 82, the crawler's basic design is composed of five modules linked by flexible connections:

- the front camera,
- the front and back grippers, and
- the two middle expansion modules.

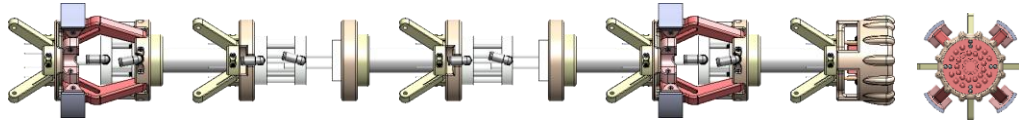


Figure 82. Pneumatic pipe crawler.

Figure 83 shows an overall schematic of the crawler, which also includes three additional components: a control box, a tether, and an instrumentation module which is currently being designed. The new module will use an embedded computer for instrument control and communication.

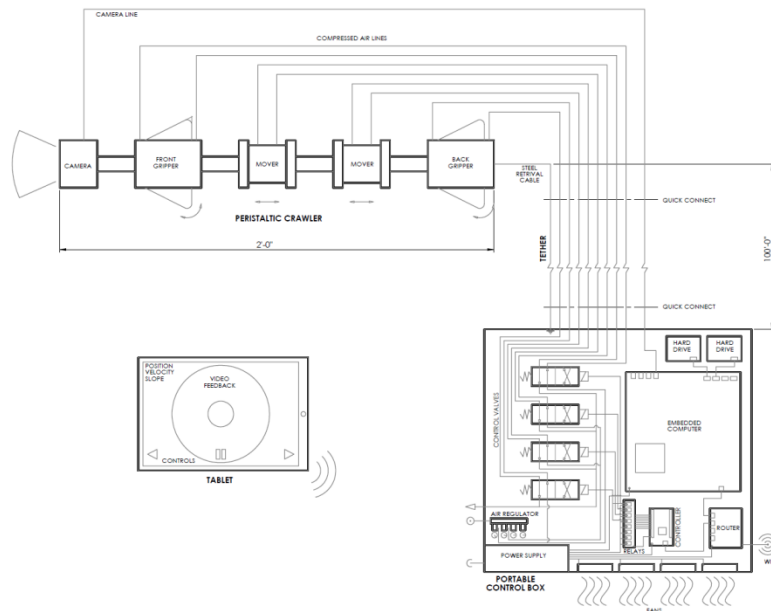


Figure 83. Overall schematic of pneumatic pipe crawler.

Expansion Module

The expansion module, shown in Figure 79, uses compact nonrotating tie rod air cylinders to propel the crawler forward during the peristaltic movements of contraction and expansion. These cylinders have two parallel piston rods that prevent the rotation of the front camera, and house actuators that have 3/4" stroke, 3/4" bore diameter and are capable of producing 40 lbs force at 100 psi.

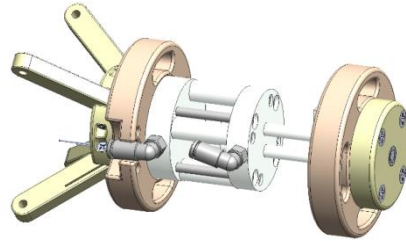


Figure 84. Expansion module.

Gripper Module

The gripper modules, shown in Figure 85, are designed to grip pipes and fittings with internal diameters varying from 3" to 4".

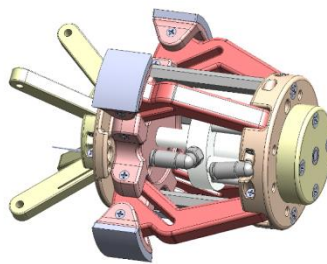


Figure 85. Gripper module.

Maximizing the grip strength of the module was a major factor in the development of the crawler. Increased grip strength will allow the device to carry additional instrumentation, and to inspect longer pipelines, which will be critical when considering the crawler for other types of applications and inspections. Figure 86 shows the evolution of the gripping mechanism over the last year and a half.

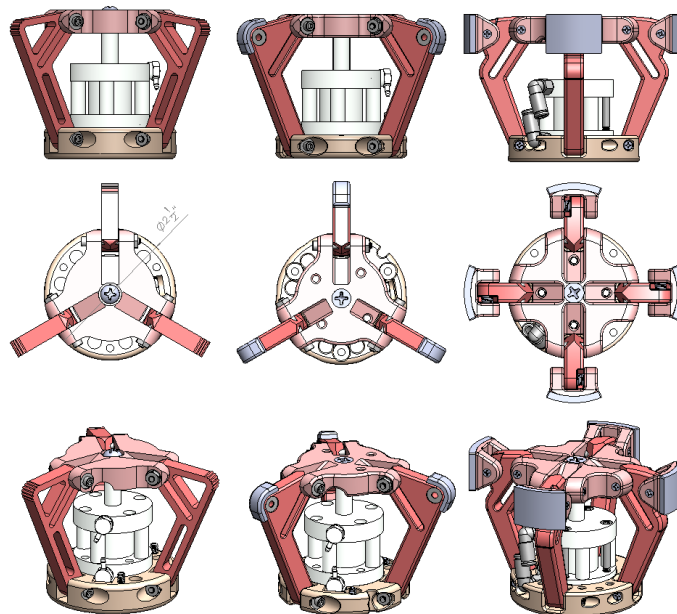


Figure 86. Design evolution of the gripper modules.

Strong grips were obtained by increasing the number of claws per gripper and by redesigning the claws using hinged tips with cylindrical pads. As shown in Figure 87, the redesigned claws also use extension springs to retrieve the pads when the mechanism closes, keeping a tight fit during crawling.

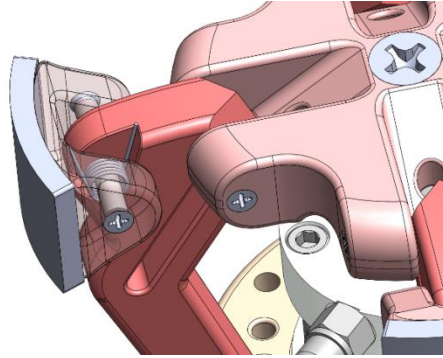


Figure 87. Gripper claws with hinged pads.

The initial design provided a gripping force of approximately 18 lbs which was increased to 40 lbs with the aforementioned design modifications. The achieved grip of 40 lbs is equivalent to the maximum force in which the expansion modules can propel the crawler. However this maximum force may vary with the internal conditions of the pipe surface. The issue will be addressed during the mockup testing.

Figure 88 shows a preliminary design of an electric version of the grippers. In this design, the gripping mechanism is actuated by a leadscrew driven by a micro DC gearmotor instead of using pneumatic actuators,

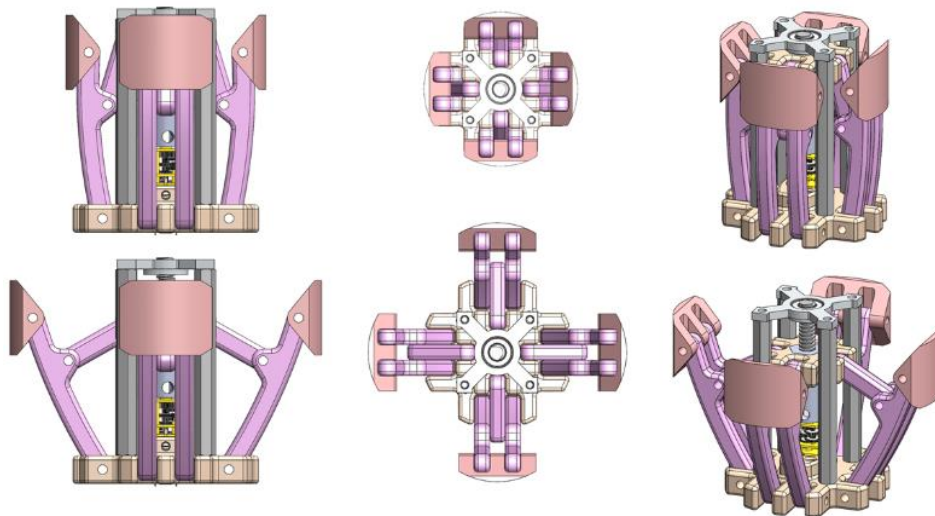


Figure 88. Electric gripper preliminary design.

An electric version of the crawler has the potential to develop stronger and smaller inspection tools. However, the output speed and force control are concerns that will need to be addressed.

Camera Module

The front camera module, shown in Figure 89, carries a day-night 1.0 megapixel (720p) digital camera, with infrared cut-off filters and LEDs. The camera is an independent module, and can be easily replaced depending on the specific application.

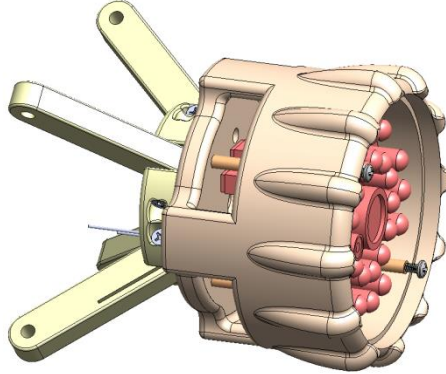


Figure 89. Camera module.

One of enhancements in the design of the front camera was the addition of external ribs to the case shown in Figure 90.

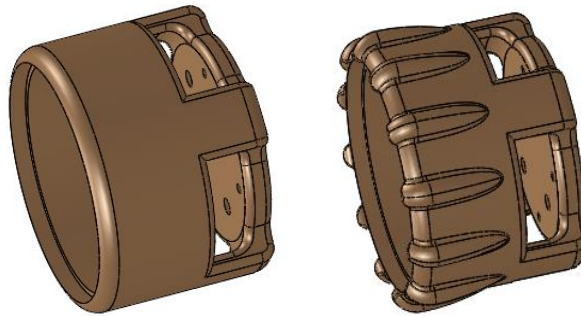


Figure 90. Original front camera case and redesign.

The ribs, as illustrated in Figure 91, assist the camera in overcoming slight fitting misalignments in the pipeline during a turning maneuver. However, a front guiding mechanism will need to be incorporated into the design if considerable misalignments are involved.

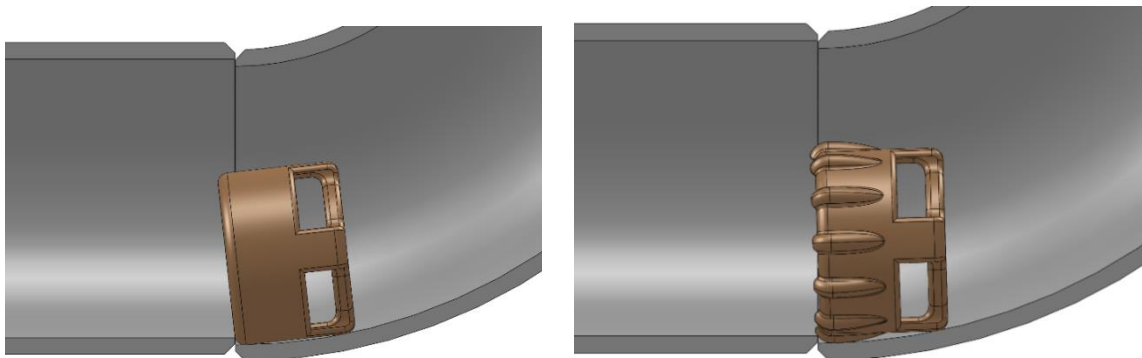


Figure 91. Piping misalignment and front camera overcoming misalignment.

Module Flexible Connection

All modules are linked by flexible connections shown in Figure 92. In the crawler design, the flexible connections have two crucial functions during maneuvers through pipes and fittings: 1) allow the unit to bend, and 2) keep the modules centered.

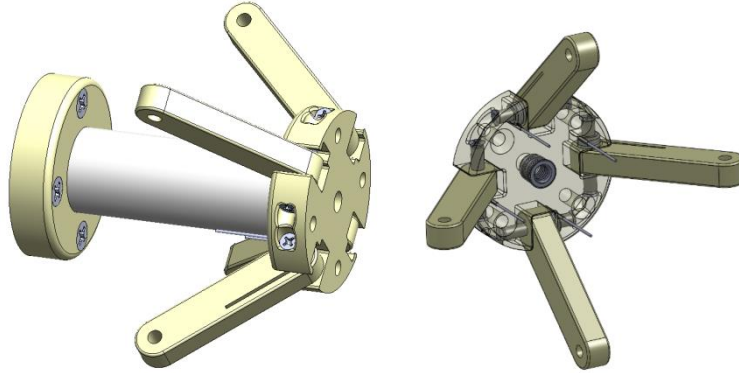


Figure 92. Module flexible connection (left), guide mechanism (right).

As illustrated in Figure 93, the original mechanism uses small arms and torsion springs to keep the modules near the center of pipes and fittings, which minimizes bouncing and dragging of the unit. The guides also prevent the bulldozer effect (collection of debris) in the front camera.

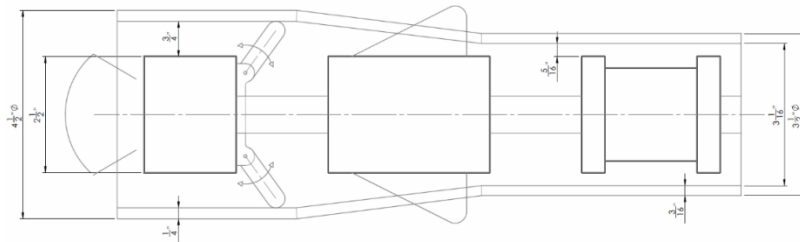


Figure 93. Guide mechanism illustration.

Figure 94 shows a rendering of the complete pneumatic crawler, where additional extension springs and wheels were added to the suspension guides.

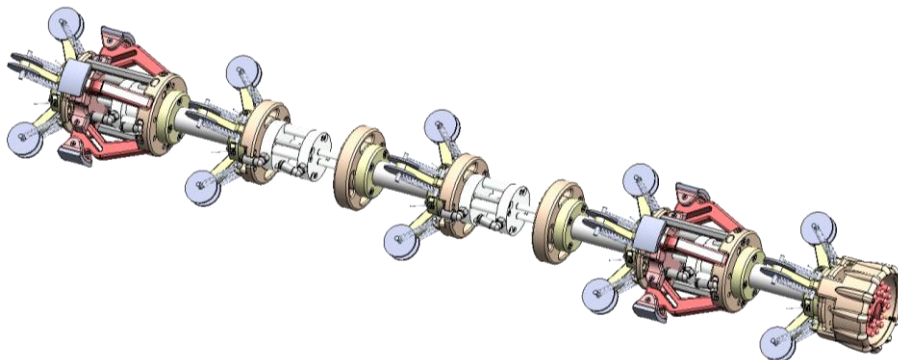


Figure 94. Schematic of crawler's recent design.

Figure 95 shows the strengthened suspension guides. The addition of extension springs was necessary to compensate for the weak torsional springs used in the original design. Off-the-shelf torsional springs with adequate size/strength ratio were not available. The additional wheels

reduce the dragging and assist in the removal of the crawler in the event of a failure. However they are not critical to the forward motion of the system.

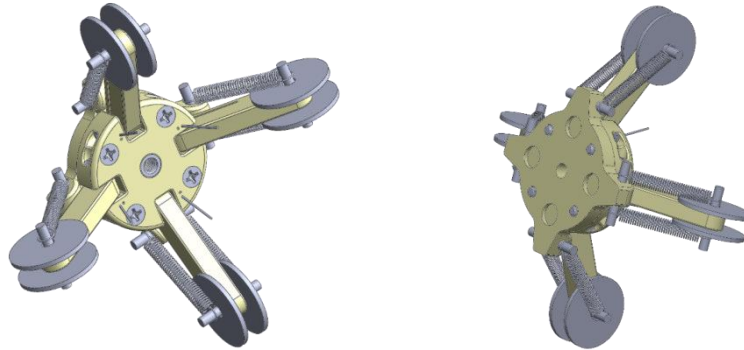


Figure 95. Strengthened suspension guides.

Control Box

Figure 96 shows a schematic of the portable control box. The box will be used for field deployment. The design, shown in Figure 97, is self-contained and includes panels which provide:

- quick disconnect for all pneumatic and electric lines,
- pressure regulator,
- pressure gauges,
- internet and USB access, and
- touch screen interface.

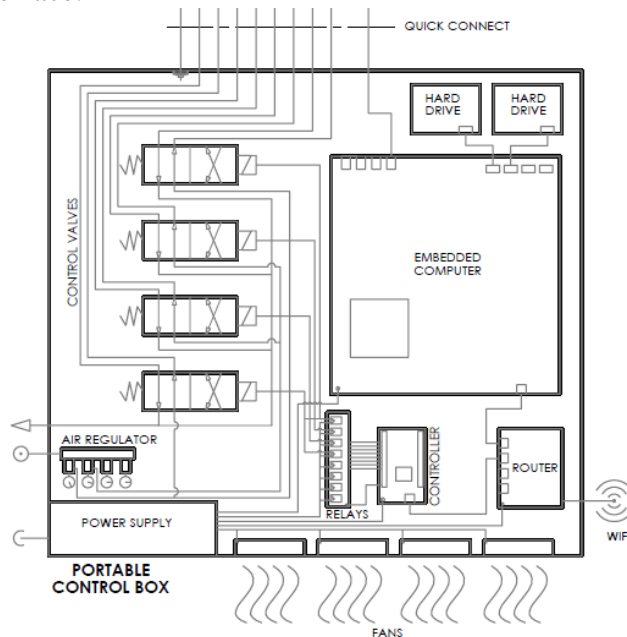


Figure 96. Control box schematic.

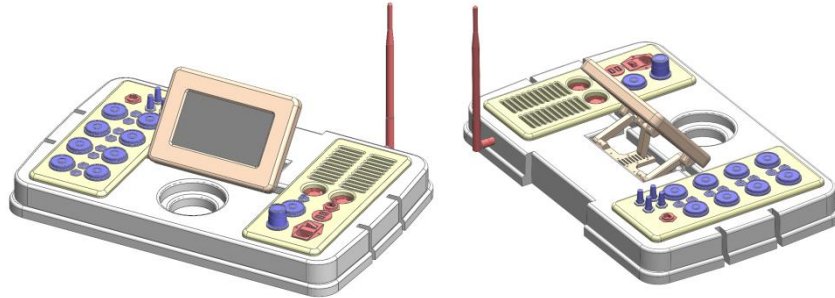


Figure 97. Control box cover.

With the control box, the crawler movement is fully automated and can be controlled remotely using any handheld device connected to the private wireless network of the box. The controlling software is customizable, which increases the versatility of the tool. Figure 98 shows the assembled control box including the cables, wires and controllers.



Figure 98. Control box.

The speed of the crawler is determined by the peristaltic cycle. The cycle distance is defined by the displacement of expansion modules. The cycle time and the device speed is programmable; however, the maximum working frequency is influenced the pressurization of the pneumatic lines and the tether length.

Tether

The tether required for the proposed inspection will be approximately 100 feet in length. Show in Figure 99, the tether includes 8 pneumatic lines, 1 camera line, and 1 retrieval steel cable.

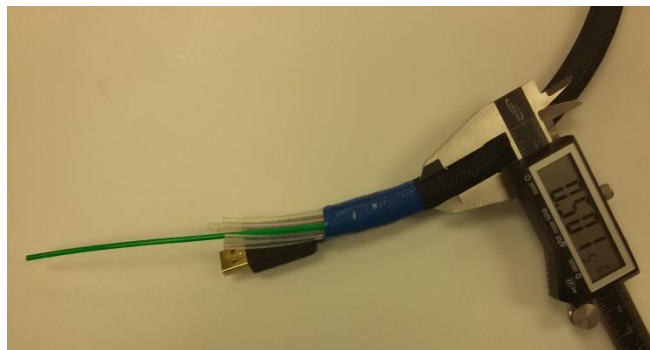


Figure 99. Tether line.

The tether diameter is approximately 1/2". The retrieval cable is responsible for carrying the pulling load, which relieves tension in the other lines of the tether. The bundle is also enclosed by an abrasion-resistant sleeve, which reduces friction and protects the cables from wear and tear.

In the recent design of the crawler, an Ethernet cable has replaced the USB cable which provided live video feedback from the device. The network cable not only allows communication with the module, but also supplies electric power. With this change, additional smart sensors can be incorporated to the current design without the addition of extra cables and future modifications to the tether.

Instrumentation Module

a new instrumentation module is currently being designed to provide sensor feedback from the crawler during inspections. As illustrated in Figure 100, the module will carry an embedded computer, a tether load cell, and additional sensors.

The module uses the embedded computer for instrument control and communication, which also allows video streaming from the front camera. At the current stage of the design, the sensors being considered may provide feedback on orientation, altitude, pressure, temperature, humidity and radiation. In addition, there are plans to include nondestructive testing and inspection sensors, such as ultrasound for pipeline life assessment.

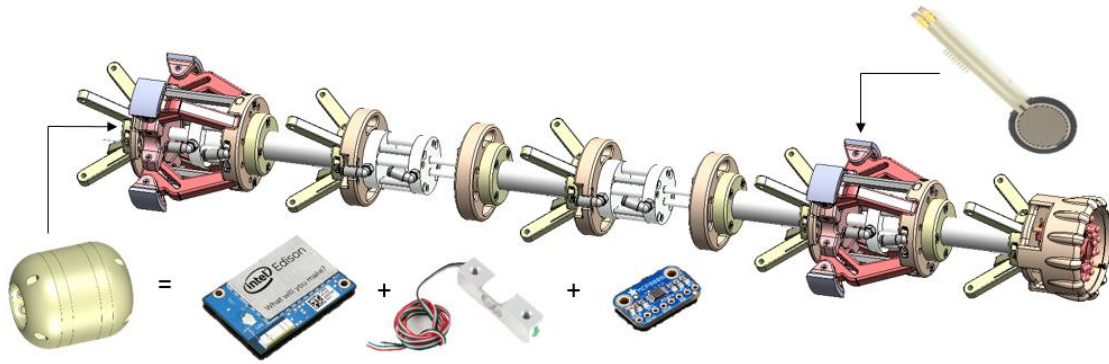


Figure 100. Instrumentation module.

The design of the instrumentation module is currently in its final stages. Issues related to the component miniaturization of the instrumentation module have been addressed; however cable management is still a design challenge.

The miniaturization issues were resolved with the use of a micro USB hub. Shown in Figure 101, the micro hub does not have the typical connectors for slave USB devices. The wires are soldered directly to it, which allows for the connection of several USB devices, such as cameras and sensors in a tiny space (1.4" x 0.8"). The hub also supports an external power supply which overcomes other issues associated with the low power available directly from the embedded computer used in the module.



Figure 101. Micro USB hub.

In addition, the use of force sensitive resistors (FSR) were investigated. The sensors can be planted in the claw pads of the gripping mechanism, which would provide a means to measure the grip force. The FSR varies its resistance depending on how much pressure is being applied to the sensing area. The harder the force, the lower the resistance. Figure 128 shows an FSR with a round, 0.5" diameter sensing area that senses applied forces anywhere in the range of 0.2 to 22 lbs. The addition of the FSR to the design could provide gripping and sliding feedback during the mockup tests and future inspections, which will enhance the robustness of the inspection tool.



Figure 102. Force sensitive resistor.

In addition, the controlling software was successfully implemented and tested. The software infrastructure allows for the the simultaneous communication, sensor feedback, and video streaming from the inspection tool to the main control box. The multi-client/server application was developed in C++ and uses native capabilities of the embedded computer, such as the standard sockets library, and multithreading.

With the objective of integrating additional instrumentation to the crawler, ways to implement a network of smart sensors were also investigated. Among several technologies, the Inter-integrated Circuit (I²C) protocol was selected. I²C is a protocol intended to allow a “master-slaves” network of multiple digital integrated circuits. It requires two wires only, and the basic version can communication up to 1008 devices at 100 or 400 kHz. The protocol was successfully tested using the MCP9808 temperature sensor shown in Figure 103.

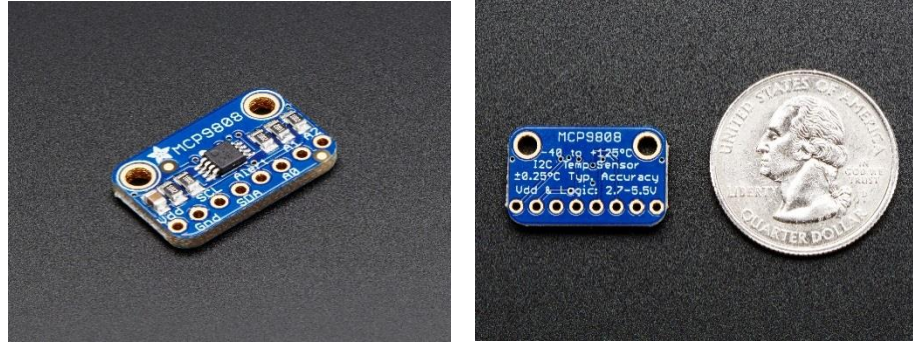


Figure 103. MCP9808 precision I2C temperature sensor.

Bench Scale Testing

To validate the design concept and demonstrate the potential of the crawler, two bench scale testbeds were manufactured to evaluate various parameters of the crawler; this included the maximum pull force, and the system's maneuverability. Figure 106 shows testbed used for conducting the maximum pull force and grip tests. These tests are important since the distance the crawler can navigate by overcoming the tether drag is directly proportional to its maximum pull force. With the design improvement of the grippers, a maximum grip of 40 lbs was achieved.

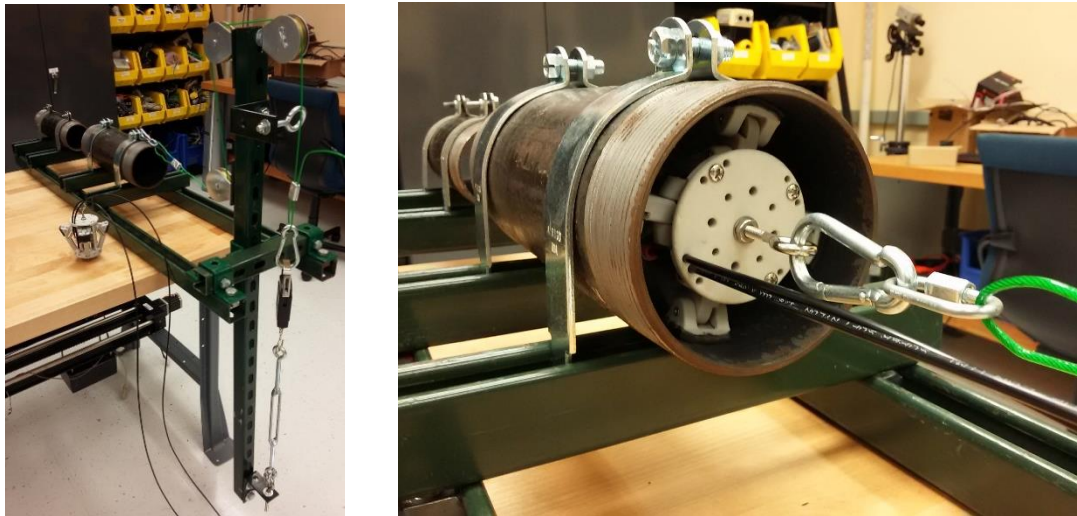


Figure 104. Bench scale pull tests.

Figure 105, below, shows the modular bench scale testbed used in the crawler design process to evaluate the system's maneuverability. The testbed consists of 3" and 4" clear PVC pipe, including steel elbows and reducers.

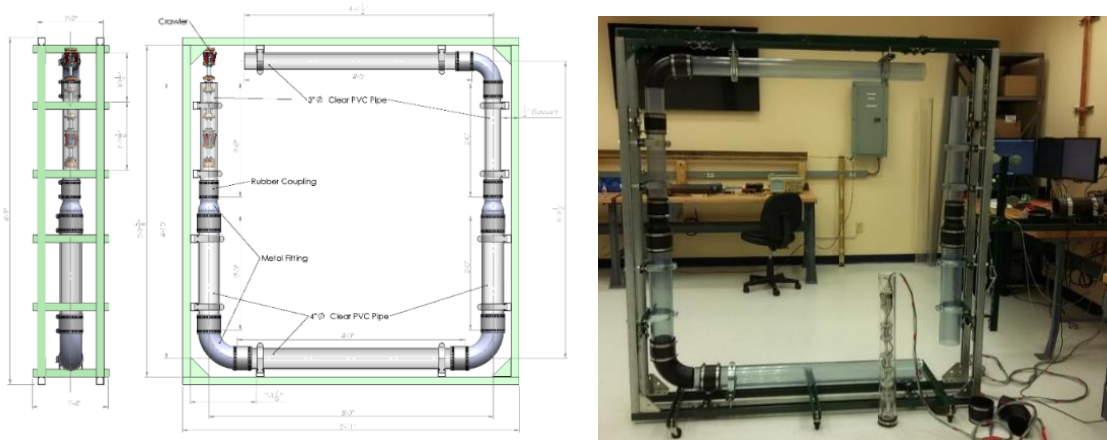


Figure 105. Modular bench scale tested.

Figure 106 shows the crawler successfully navigated through the 3" elbow in the pipe loop, where several levels of misalignments were tested.

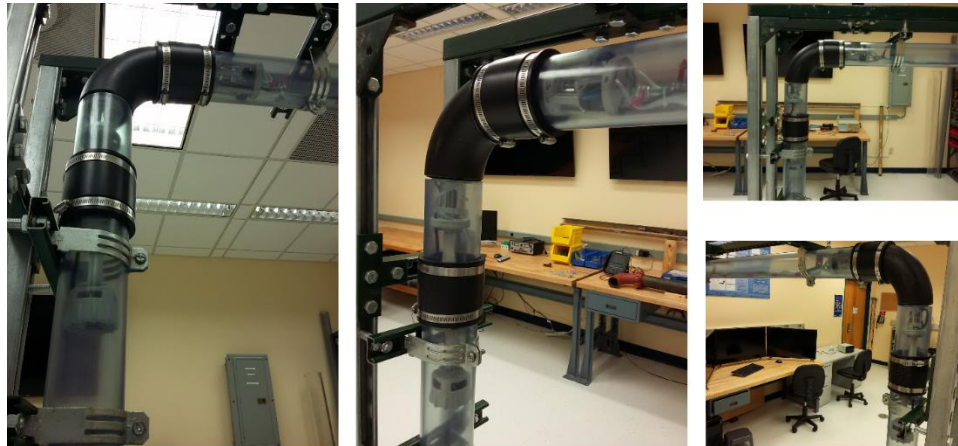


Figure 106. Crawler navigating through a 3" elbow.

Engineering Scale Testing

To evaluate the performance of the pneumatic crawler, a full scale mockup of the ventilation system for AY-102 was manufactured. For full scale tests, the primary concern is the crawler's ability to manage the tether and to overcome the increasing drag force during the inspection. The path dimensions of the proposed inspection are shown in Figure 107.

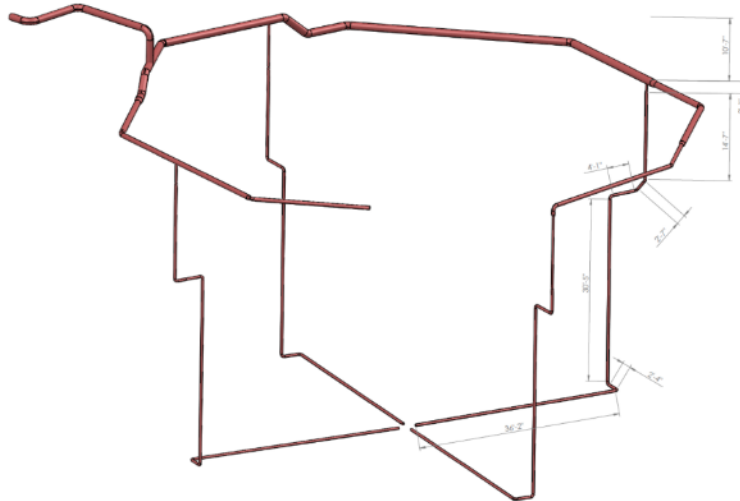


Figure 107. AY-102 ventilation riser.

The testbed, shown in Figure 108 below, has a layout equivalent to one of the AY-102 ventilation risers. In the configuration, however, the initial vertical section runs horizontally, which is structurally cost effective, considering that approximately 60 ft of piping would need to be vertically supported. In addition, the horizontal configuration will be more challenging, considering that during the vertical section, the crawler would be primarily gravity fed. Figure 109 details the layout of the mockup. Figure 110 shows the full scale mockup constructed at FIU.

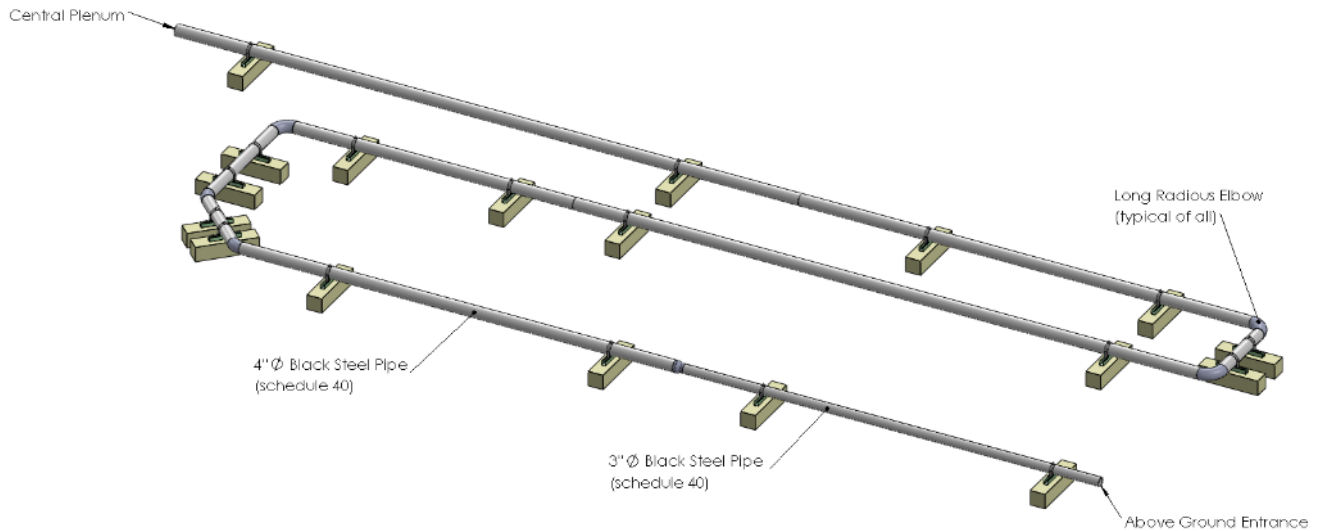


Figure 108. Ventilation riser mockup.

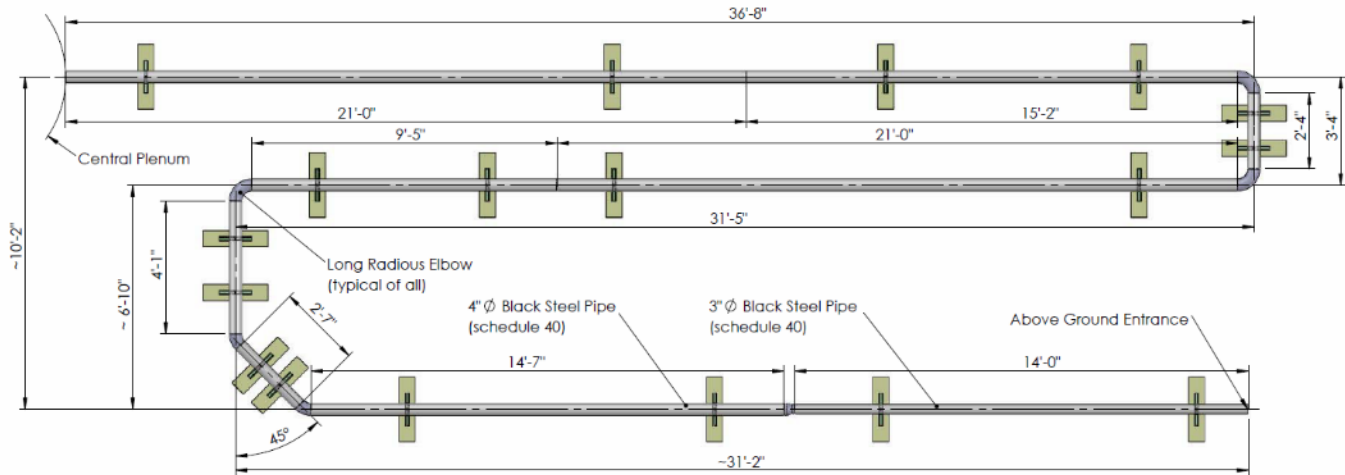


Figure 109. Layout of the ventilation riser mockup.



Figure 110. Ventilation riser mockup.

Figure 111 shows preliminary pull force tests being conducted with the full scale mockup. The tether was dragged through the pipeline, while the dragging force was measured with a hand scale. During these tests, the average recorded drag force was approximately 5 pounds. The levels eventually peaked around 8 lbs, which is well below the pull force of the crawler (40 lbs). However, pipe surface conditions, such as the presence of water, rust and residue material, might affect the overall performance of the device.



Figure 111. Preliminary tether pull and drag testing.

Figure 112 shows a full scale test, in which the crawler was able to navigate through the bends and crawl through approximately 100 ft of pipeline.



Figure 112. Full scale testing.

Due to the tether length, the speed of the crawler was significantly decreased. It took approximately 1 second to pressurize each pneumatic line, which led to a cycle time of approximately 5 seconds. The crawler moves 1.5” per cycle. Thus, the speed of the system was 0.3 in/s. The 100 ft inspection was completed in about 1 hour and 20 minutes. The speed could be improved, however, with better timing and/or the addition of expansion modules.

Another alternative is to use micro pneumatic control valves embedded in the crawler modules supplied by a tether with a single air manifold. This solution would solve the issue with the pressurization of the pneumatic lines, and would also reduce the tether diameter significantly. However, this modification was implemented in the first generation of peristaltic crawlers, and it was not originally considered in this project due to the high cost involved with micro pneumatic control valves. In addition, improving the crawlers speed is not considered a priority at this point in time.

CONCLUSIONS AND FUTURE WORK

A magnetic miniature inspection tool was designed, capable of traveling through the refractory cooling channels and provide live video feedback of the channels and tank floor of DSTs at Hanford.

Lab-scale mock up tests revealed various areas for improvement such as the need for redesigned wheels to withstand the cyclic loading, the magnetic force and transverse loads when turning. Another area for improvement that was addressed was reducing the width as much as possible, and implementing a tether management system. Testing of the inspection tool has provided valuable information such as its ability to traverse through non-ideal environments such as through concave surfaces, over gaps and over a surface with rust and weathering.

The path forward includes testing the inspection tool in the full-scale mockup to examine its performance in a more realistic environment. Testing in a full-scale mockup will provide an accurate indication of the inspection tools capabilities and any other necessary modifications. Other areas that will be explored include integration of sensors and a deployment mechanism. This tool has been designed to maneuver upside down over flat surfaces, though it has shown capability in traversing through other environments. A deployment mechanism will allow the tool to be deployed directly into the channel, as well as have a tether management system integrated. The inspection tool is currently fitted with a camera to provide live video feedback, though fitting it with other sensors will be explored. These sensors include (but are not limited to) ultrasonic transducers and radiation sensors.

A pneumatic pipe crawler that will carry out the robotic inspection of the ventilation header piping of the DSTs was also successfully designed. The device will provide realtime feedback from video and several other sensors during inspection. A functional prototype was successfully manufactured and tested in bench and full scale testbeds. Based on the results, the crawler has great potential to accomplish the proposed inspection at Hanford.

The path forward for the crawler includes (a) finalizing the instrumentation module design, (b) continuing validation of the device in full scale tests, (c) continuing the modification of the design as needed, (d) developing a cable management system, (e) integrating various sensors suitable for non-destructive inspection, and (f) scaling up the design for inspecting the 6" leak detection pipeline in the DSTs. Based on the availability of time and budget, the future plans may also include designing a full electric version and scaling down the design for inspecting 2" pipelines.

TASK 18.3

INVESTIGATION USING AN INFRARED TEMPERATURE SENSOR TO DETERMINE THE INSIDE WALL TEMPERATURE OF DSTs (FIU Year 6)

EXECUTIVE SUMMARY

Corrosion in DSTs is one of the primary concerns at Hanford and other sites. It is managed by stringent operating specifications as given in OSD-T-151-00007 “Operating Specifications for the Double-Shell Storage Tanks” (OSD) [1]. One of the important parameters specified by OSD is the temperature which plays an important role in corrosion. In general, the tank temperatures are determined by various processes such as: the physics behind the problem, taking samples at different locations, using some measurement devices and finally modeling. Most of these methods are approximations on the actual temperatures at various locations inside the DST’s. Hence, there is an immense need for measurement and calculations of actual temperatures inside the tanks. Of particular interest is at the interface of the tank waste and the inner walls since it accounts for the region highly prone to corrosion.

It is known that the actual temperatures in the tanks are measured more than 10 feet away from the wall due to technical and equipment constraints [2]. The tank-wall interface temperatures are then predicted using mathematical models. Most of these models have not been validated.

The present task investigates in the use of an infrared (IR) sensor to measure the outer wall temperatures of the primary shell in the DST. This process is practical since the sensor is expected to “piggy back” on the scheduled inspection tools passing through the annulus of the DSTs. The method checks whether the temperatures are within limits and may aid in obtaining accurate data for input to thermal models and in some cases, validate the models.

A test matrix was developed to conduct preliminary experiments on a bench scale. The DSTs were represented using rectangular tanks. The IR sensor, as recommended by the site engineers (WRPS), was the Raytek MI3 [4] sensor. The sensor was procured, calibrated and emissivity adjustment tests were conducted. The test matrix was defined based on various parameters such as the distance of the sensor from the test piece, length of the test piece and temperature. Also, the sensor results were compared to those obtained using thermocouple measurements. The experiments have been conducted and the results obtained were analyzed. In addition, heat transfer based models were generated and solved using commercially available software (Solidworks 2013) to study the temperature profiles in the primary tank walls.

INTRODUCTION

One of the important variables specified by the operating specifications of double shell tanks is temperature. It plays a vital role in the initiation and propagation of corrosion in metals. Since DST's are made of carbon steel and store nuclear waste in various forms (solid, liquid and supernatant), it is essential to know the exact temperatures in the tanks especially at the waste-wall interfaces.

Hence, the present task aims to check the validity of the use of a non-contact pyrometer to measure the outer temperatures of the primary tank wall in DST's. This method of measuring the wall temperature can be used with the current inspection equipment or the sensor can be attached to an annulus inspection camera. At FIU, two robotic inspection tools are being developed and the IR sensor can easily be attached to them as a built-in or as a separate module. "Piggy backing" of the sensor to pre-scheduled operations allows for the collection of temperature data with minimal impact on tank farm operations. The temperature results thus obtained will serve multiple purposes: (a) ensuring that the limits are met and, if not met, allow for immediate corrections; (b) physical properties can be empirically calculated, providing validation/evaluation of the current thermal modeling capabilities; (c) temperature gradients would help in the estimation of solid waste levels in the tanks; (d) the IR sensor can also be used to calibrate other equipment; and (e) expensive and time consuming thermal modeling can be minimized or avoided in certain conditions.

To be used in the DST's, the IR sensor needs to have certain requirements as given below:

- Must be a non-contact pyrometer
- Must be mounted and remote controlled
- Should be wired (long wire must be available 50' – 75')
- Must be able to get temperature from dull/rusty carbon steel
- Must be able to get accurate reading from a distance of 1-3 inches
- Must have software compatible with windows machine (Windows 7)
- Software must support data logging
- Temperature measurements will be 0°F to 250°F
- Able to operate in an environment of 40°F to 150°F
- Equipment must have adjustable emissivity

Further, the dimensions of the IR sensor should be suitable to fit within a 6 cubic inch volume. The preferable size would be 6" x 6" x 6" but an alternative size could be 8"x4"x4". The spectral range of the sensor should be 8 μm to 14 μm , response time should be less than 1 second and the aperture must be less than 1".

Based on the above requirements and discussions with site engineers, the Raytek MI3 infrared sensor has been selected for the purpose. In addition, a test procedure has been developed and implemented for bench scale testing. The details of the sensor along with the test procedure are provided in the next section.

SENSOR AND BENCH SCALE TESTS

Raytek Miniature Infrared sensor

The IR sensor chosen for the present tests is the Raytek MI3 [4]. It is a pyrometer (non-contact sensor) that includes a digital screen for temperature display (Figure 113). It primarily consists of two parts: the sensing head and the digital communication box. Based on the specifications of the present task, the product has variable (adjustable) emissivity. The spectral range of the MI3 series is 8-14 μm with a response time of 130 ms and an accuracy of 1°C. It is 0.55 inches in diameter and 1.1 inches in length and has a distance spot ratio of 22:1. Also, a 98-foot cable is available for the sensing head and will need to be integrated with the tether of the inspection tool on which the sensor will be placed.

IR sensor emissivity configuration

The sensor needs to be adjusted for emissivity to correlate with the test material since each material has its own emissivity. The procedure adopted for calibrating the emissivity includes a number of steps. Using literature values, an emissivity of the carbon steel material was chosen and used as a starting point for the IR sensor measurements. The tank wall temperatures are recorded using that emissivity value. The measured values are then compared to the actual temperatures on the wall obtained using a laser gun (non-contact pyrometer) or a thermocouple. In case of discrepancy, the emissivity is adjusted again and the process repeated until the exact emissivity of the material is obtained. This procedure ensures that the most accurate measurements are obtained by the Raytek MI3 sensor.



Figure 113. (a) Raytek Sensor [4] and (b) Sensor Head [4]

Experimental Approach

For the present task, the Raytek IR sensor is to be attached to an inspection device and deployed into the annulus to scan the entire tank height for temperature measurements. A typical sketch of the process is as shown in Figure 114(a).

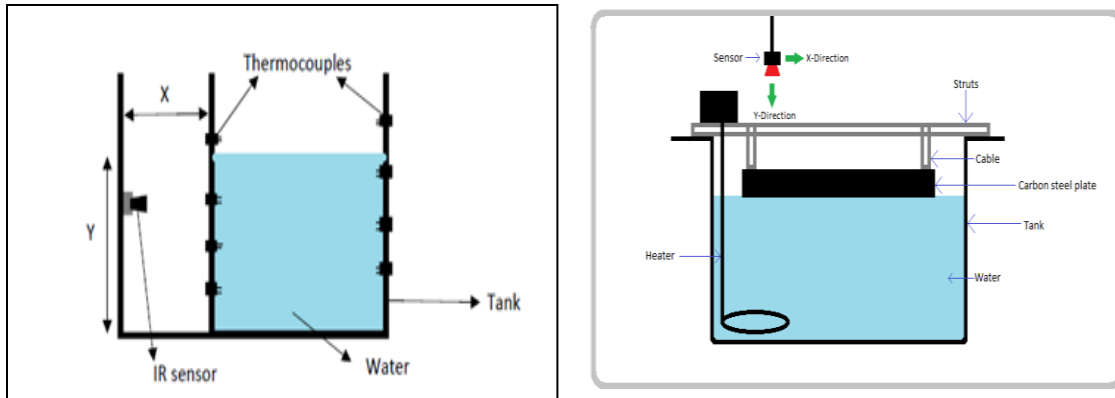


Figure 114. (a) IR sensor through the annulus and (b) Test set up (block diagram).

Since the objective is to understand the thermal gradients in the tank, a test setup is established (Figure 114(b)) for the present task that represents the configuration of the double shell tanks. The setup consists of a rectangular stainless steel tank of dimensions 2 ft. x 4 ft. x 3 ft. Fluid (water) is heated in the tank and a thick carbon steel plate of 7/8 inch thickness (replicating the maximum DST wall thickness) is suspended onto the fluid surface using strut channels and cables/rods. A side mount heater is used to increase the water temperature and measurements are recorded at various time intervals.

The Raytek IR sensor is used to measure temperatures on the outer surface (exposed to the atmosphere) of the plate while it transfers heat from the hot water to the ambient air outside. Heat transfer calculations provide a prediction of the temperatures on the inner surface (exposed to the fluid). Also, thermocouples are inserted at various set points to obtain accurate readings. To validate the use of the Raytek IR sensor, temperature measurements are also taken at the surface using thermocouples. Roller surface K-type thermocouples along with the universal thermocouple connectors (UTC-USB) were used to acquire the temperature data. The actual experimental set up including the Raytek IR sensor and the thermocouple is shown in Figure 115.



Figure 115. Experimental set up including sensors.

To conduct the experiments, a test matrix is defined based on the experimental set up and approximations, and includes the following parameters:

- Temperature of water inside the tank – the temperature of the water bath in the tank is varied from 90°F to 130°F in intervals of 10°F.

- Measurement along the length of the test piece (x-direction) – These set points for temperatures represent the vertical height of the tank are specified in intervals of 6 inches starting from one end to the other.
- Distance of the IR sensor from the test piece (y-direction) – The annulus of DSTs is approximately 3ft. wide, so the IR sensor is configured and physically placed to capture readings at distances of 2 in, 6 in, 12 in, 18 in and 24 in.

The matrix with the range of temperature values is given in Table 7, which represents the distances and temperature range.

Table 7. Test Matrix (Temperature in °F)

Distance	Y = 2	Y = 6	Y = 12	Y = 18	Y = 24
X = 0	[90 130]	[90 130]	[90 130]	[90 130]	[90 130]
X = 6	[90 130]	[90 130]	[90 130]	[90 130]	[90 130]
X = 12	[90 130]	[90 130]	[90 130]	[90 130]	[90 130]
X = 18	[90 130]	[90 130]	[90 130]	[90 130]	[90 130]
X = 24	[90 130]	[90 130]	[90 130]	[90 130]	[90 130]
X = 30	[90 130]	[90 130]	[90 130]	[90 130]	[90 130]
X = 36	[90 130]	[90 130]	[90 130]	[90 130]	[90 130]
X = 42	[90 130]	[90 130]	[90 130]	[90 130]	[90 130]

* Distance in inches

The experiments have been conducted according to the test matrix and the results obtained are discussed in the next section.

RESULTS AND DISCUSSION

Initial experiments were conducted as described in the test matrix by varying the heights from the test piece along the length intervals. Temperature measurements were obtained on the outer surface of the test piece at various time intervals. A sample set of test results obtained from the IR sensor and thermocouple at different time intervals is provided in Table 8 and 12. The temperature measurements using the thermocouple are taken as standard and are compared with those obtained by the Raytek MI3 IR sensor.

From the tables, it can be seen that the Raytek IR sensor has a maximum temperature variation of 10.2% from the thermocouple readings. This could be due to the sensitivity of the IR sensor which in turn is affected by the variation in the ambient temperatures during the experiments. In order to study the variations, an error analysis has been performed on different sets of sample data obtained from the both sensors. The average temperature measured at a particular height (y-distance) from the Raytek sensor is compared to that of the thermocouple measurement. The average error obtained is 4.5%. It shows that the IR sensor is capable of predicting the temperatures within limits.

Table 8. Temperature(°F) Results Test 1 (IR Sensor and Thermocouple)

Distance*	Y= 2	Y= 6	Y= 12	Y= 18	Y= 24	TC[@]
X= 0	102	102	102	102	102	102
X= 6	110	110	110	110	109	100
X= 12	108	108	108	107	107	100
X= 18	108	108	107	106	105	101
X= 24	104	102	102	102	102	100
X= 30	104	102	101	101	102	100
X= 36	103	103	102	102	101	100
X= 42	103	104	104	104	103	99

* Inches; @ Thermocouple

Table 9. Temperature(°F) Results Test 2 (IR Sensor and Thermocouple)

Distance*	Y= 2	Y= 6	Y= 12	Y= 18	Y= 24	TC®
X= 0	120	118	115	110	115	110
X= 6	121	120	118	119	118	109
X= 12	117	116	115	115	115	108
X= 18	115	111	115	112	113	109
X= 24	109	107	107	106	106	110
X= 30	110	109	109	108	106	110
X= 36	106	104	104	103	104	109
X= 42	105	103	103	102	102	105

Temperature as a function of sensor height and test piece length is plotted in Figure 116 for the sample tests 1 and 2, respectively. It is evident from the graphs that the temperature contours represent similarity with changes in height. This shows that height is not a very significant parameter for the sensor in the given range (2 in. to 24 in.). Also, in both of the graphs, there is a peak value for temperature at 6 in. length and then a gradual reduction. This is due to the maximum temperature near the heating coil underneath the test piece. The gradual reduction in temperature away from one end of the test piece is due to the heating effect occurring as a result of the side mount electric coil heater.

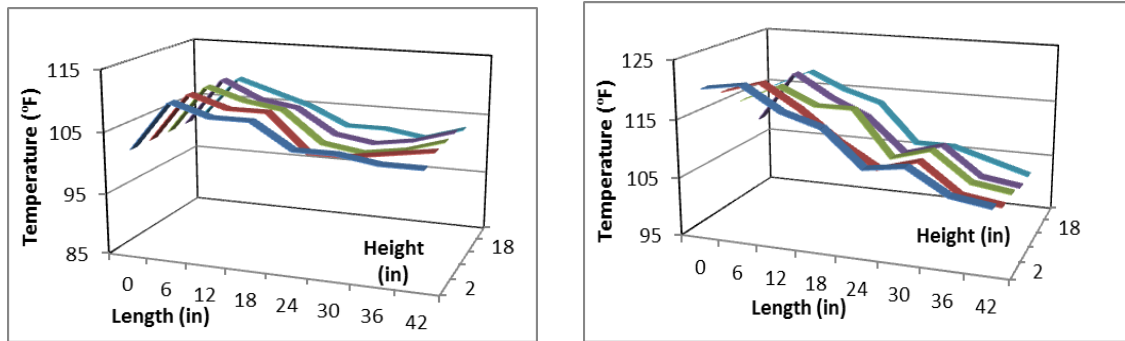


Figure 116. (a) Temperature contours (Test 1) and (b) Temperature contours (Test 2).

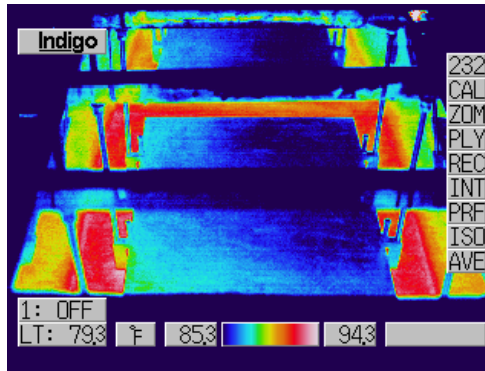


Figure 117. Temperature contours using thermal camera.

A thermal camera (TVS 700) is also used to record the temperature profiles as a visual indication of heat transfer between water and the plate. A sample thermal image as recorded is shown in Figure 117. It provides the temperature measurements in the range of 85-95°F. Red color indicates the maximum temperature while blue indicates the minimum. As expected, it can be seen that the water in the tank has the highest temperature (red) and the plate has the lowest.

In addition to the experimental tests, thermal modeling has also been conducted to verify and predict the temperature profiles for the test piece. Heat transfer based modelling and simulation has been conducted using Solidworks. The test piece is modeled for convective heat transfer on both sides assuming air and water as the convective fluids. Natural convection is assumed. Conduction heat transfer is considered inside the solid test piece. A sample set of simulation results are shown in Figure 118. The air side temperature is fixed at 100 °F and the heat transfer analysis is performed to obtain the bulk mean temperature of water on the other side. Figure 118 (a) represents the heat transfer through the plate/wall and Figure 118 (b) represents the detailed temperature profile along the cross section of the plate/wall.

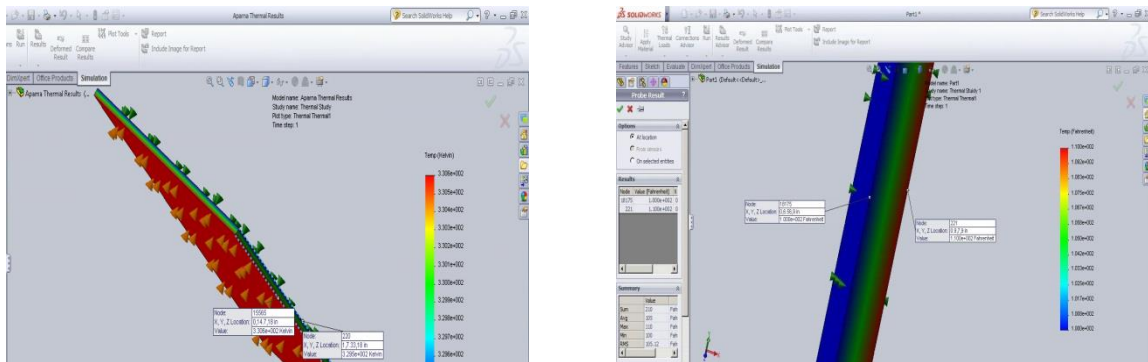


Figure 118. (a) Heat transfer through the plate/wall and (b) temperature profile (plate cross section).

The experimental and simulation results are based on baseline experiments. In the future, advanced DAQ systems will be used for real time measurements using multiple thermocouples to have accurate readings which will be compared to the IR sensor readings.

CONCLUSIONS AND FUTURE WORK

In the present task, the viability of the use of the IR sensor as a potential option for measuring tank wall temperatures has been investigated. The IR sensor has been obtained, calibrated and emissivity tests have been conducted. A test plan was developed and baseline experiments have been executed. Results obtained from the IR sensor have been compared to those obtained from thermocouples.

Data presented is based on initial experiments. In future tests, thermocouples will be added on the inner surface of the test piece for accurate thermal measurement and validation. Also, the temperature range currently being used for the tests is 90-130°F which is primarily due to the type of heater being used. For future tests, the actual temperature range as specified for the DST's (120-170°F) will be used with new heating options.

In addition, detailed investigation into the sensitivity of the Raytek sensors will be conducted. Finally, advanced thermal modeling and simulation will be conducted to verify and validate the IR sensor measurements and also to simulate the thermal gradient inside the tanks and in the annulus.

To summarize, the present work is based on bench scale testing and approximations and is being further extended to replicate the actual engineering scale testing and simulation which might result in future site deployment.

REFERENCES

1. OSD-T-151-00007, Operating specifications for the Double-Shell Storage Tanks, Rev 1, Washington River Protection Solutions, Richland, WA.
2. Holsmith, B. (2015). Double Shell Tank Primary Wall Temperature Measurements: Suggested New Technology White Paper, Washington River Protection Solutions, Richland, WA.
3. The Principles of Noncontact Temperature Measurement, produced by Raytek® available online at http://support.fluke.com/raytek-sales/Download/Asset/9250315_ENG_D_W.PDF
4. www.raytek.com

TASK 19.1 PIPELINE CORROSION AND EROSION EVALUATION (FIU YEAR 6)

EXECUTIVE SUMMARY

A fitness-for-service (FFS) program has been implemented by Washington River Protection Solutions (WRPS) to assess the structural integrity of pipelines, tanks and tank farm waste transfer system. The purpose of the program was to inspect primary piping, encasements, and jumpers for corrosion/erosion which has been accomplished in the previous year. As recommended, at least 5% of the buried carbon steel DSTs waste transfer line encasements were inspected. Data has been collected for a number of these system components and analyzed.

Efforts this year focused on evaluating ultrasonic transducers that can provide real-time thickness measurements for transfer system components. Previous work at WRPS utilized a pipe wrap system that had ultrasonic transducer (UT) sensors imbedded in a polymer wrap. Variations in installation procedures demonstrated that this system did not provide reliable data. In some cases, the installation of the system caused failure in the sensors. Thus, FIU has been tasked to investigate the current and commercially available UTs and their applicability to real time measurements.

Currently, different ultrasonic transducer systems are being investigated for thickness data measurement to determine the actual erosion/corrosion rates so that a reliable life expectancy of the pipe components can be obtained.

During this past year, a market study was conducted on various commercially available ultrasonic transducer systems according to the requirements listed by the WRPS/DOE personnel. Out of the many options, some of the sensors were procured and tested. Since, the data acquisition systems were expensive; two of the viable options are down selected. Recently, one of the sensor systems has been received and is ready for testing.

INTRODUCTION

The United States Department of Energy Hanford Site Tank Farm has implemented a Fitness-for-Service (FFS) program for the Waste Transfer System. The FFS program, based on API-579-1/ASME FFS-1, examines structural parameters of the waste transfer systems in order to develop erosion/corrosion rates for relevant system components. The FFS information is acquired from opportunistic evaluations of pipelines that have been removed from service. FIU-ARC engineers work closely with key Hanford high level waste (HLW) personnel and the contractor, Washington River Protection Solutions, LLC (WRPS), supporting the FFS program, delivering solutions for sensor evaluations, conducting bench-scale testing followed by data acquisition and analysis for corrosion and erosion assessment.

The objective is to assist DOE and WRPS in providing more realistic estimates of the remaining useful life of the components and to incorporate those estimates into future design plans. Previous efforts at Hanford included the installation of sensors on a number of the POR 104 components, to provide real time pipe wall thickness measurements. Due to various limitations, alternative approaches for remote permanently mounted pipe wall ultrasonic thickness measurement systems are being investigated.

Currently, FIU efforts supporting this scope include investigating key options available in the market for remote permanently-mounted ultrasonic transducer (UT) systems for HLW pipe wall thickness measurements. Specific applications include straight sections, elbows and other fittings used in jumper pits, evaporators, and valve boxes. FIU is assessing the use of various ultrasonic systems that are either commercially available or used previously at Hanford and selecting the most promising systems for further evaluation. This document provides the summary of the available options for obtaining thickness measurements for components similar to those in the POR 104 valve box. The options have been evaluated and a few were down selected for bench-scale testing.

The proposed method will provide information that will assist engineers with understanding the failure potential of HLW transfer components due to corrosion and erosion. This information can assist in determining if and when lines need to be removed, saving time and resources on the unneeded excavation of transfer lines. This information can also assist engineers with designing new transfer systems by establishing more detailed/accurate guidelines governing the life expectancy of the transfer system and its components.

SENSOR EVALUATION

After efforts by WRPS to obtain real time thickness measurements using a pipe wrap system were found to be difficult [1], FIU began investigating alternative approaches to obtain the thickness measurements. Some of the operating parameters for the sensors include their need to be able to take measurements via permanent mounting and be installed in confined spaces. To this end, FIU investigated a variety of ultrasonic sensors for measuring the thickness of 2- and 3-inch diameter pipes. A majority of the companies that carry relevant transducers did not have products that met the site needs. In particular, most sensors evaluated required the use of a liquid couplant. For this application of long-term real-time measurements, a dry couplant is more practical.

After initial discussions with WRPS engineers, FIU purchased an Olympus 45MG Digital Ultrasonic Thickness Gage [2]. The system is a dual crystal transducer that comes with a two-step reference block and a liquid couplant sample. Hence, a dry couplant was purchased and tested. The results showed that the dry couplant was unable to provide accurate readings. In addition, vacuum tests were also conducted to eliminate the air gap between the test piece and the sensor surface. These results were also found to be inaccurate to a higher degree.

Hence, other options without the use of a gel couplant were investigated. Four of the options considered were: Ultrason sensors, Permasense sensors, Acellent smart sensors, and Electromagnetic acoustic sensors (Innerspec EMAT). A brief description of the UT sensors and the experiments conducted is provided next.

Ultrasonic Transducers (UT)

An ultrasonic transducer is a device that converts electrical energy into high frequency sound energy and vice versa. The propagation of sound waves through solid materials has been used to detect hidden cracks, voids, porosity, and other internal discontinuities in metals, composites, plastics, and ceramics. High frequency sound waves reflect from flaws in predictable ways, producing distinctive echo patterns that can be displayed and recorded by portable instruments. Utilizing ultrasonic testing is completely nondestructive and safe, and it is a well-established test procedure in many basic manufacturing, processes, and service industries. The frequency range of ultrasonic testing is generally between 500 KHz and 10 MHz.

Typical transducers for ultrasonic flaw detection utilize an active element made of a piezoelectric ceramic, composite, or polymer material. When this element is excited by a high voltage electrical pulse, it vibrates across a specific spectrum of frequencies and generates a burst of sound waves. When it is vibrated by an incoming sound wave, it generates an electrical pulse. The front surface of the element is usually covered by a wear plate that protects it from damage, and the back surface is bonded to backing material that mechanically dampens vibrations once the sound generation process is complete. Because sound energy at ultrasonic frequencies does not travel efficiently through gasses, a thin layer of coupling liquid or gel is normally used between the transducer and the test piece. Figure 119 shows a typical ultrasonic transducer.

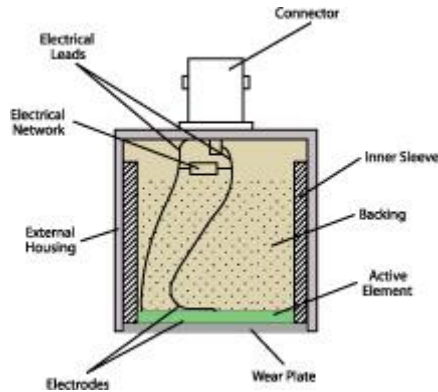


Figure 119. Cross section of a typical contact transducer 2.

There are five types of ultrasonic transducers commonly used in flaw detection applications:

Contact Transducers - As the name implies, contact transducers are used in direct contact with the test piece. They introduce sound energy perpendicular to the surface, and are typically used for locating voids, porosity, and cracks or delamination parallel to the outside surface of a part, as well as for measuring thickness.

Angle Beam Transducers - Angle beam transducers are used in conjunction with plastic or epoxy wedges (angle beams) to introduce shear waves or longitudinal waves into a test piece at a designated angle with respect to the surface. They are commonly used in weld inspection.

Delay Line Transducers - Delay line transducers incorporate a short plastic waveguide or delay line between the active element and the test piece. They are used to improve near surface resolution and also in high temperature testing, where the delay line protects the active element from thermal damage.

Immersion Transducers - Immersion transducers are designed to couple sound energy into the test piece through a water column or water bath. They are used in automated scanning applications and also in situations where a sharply focused beam is needed to improve flaw resolution.

Dual Element Transducers - Dual element transducers utilize separate transmitter and receiver elements in a single assembly. They are often used in applications involving rough surfaces, coarse grained materials, detection of pitting or porosity, and they offer good high temperature tolerance as well.

UT Systems Investigated

Many commercially available UT sensor systems were investigated based on the following performance criteria.

- Permanent mounting capability to 2-inch schedule 40 pipe (90⁰ elbow as well as straight).
- 100% duty cycle in a 200°F environment is ideal. The maximum temperature allowed for the waste transfer process is 200°F. Average transfer temperatures are closer to 130°F.
- Be able to measure accurately to 0.001 inches.
- Will potentially be operating in a 50 to 250 rad/hour environment.

- A dry couplant solution preferred.

Sensor systems investigated are listed below with details provided in the following section.

- Sigma Transducers - Pipe Wrap System
- Olympus Dual Element Sensors
- Acellent Technologies Smart Sensors
- Permasense Guided Wave Sensors
- Ultran Couplant-free Sensors
- Innerspec EMAT and DCUT Sensors

Previous Efforts

Previous efforts at Hanford for pipe wall thickness measurements included the use of a Pipe Wrap™ manufactured by Sigma transducers. Also, a conceptual solution had been modeled to demonstrate possible features of a custom made alternative. These are discussed in the next sections.

Sigma Transducers - Pipe Wrap System

The Pipe Wrap™ system consists of a linear flexible array of UT elements. Transducers are embedded in a silicon rubber substrate, which is then wrapped around the pipe and secured with a hose clamp. To manufacture the system, a mold of silicon band is created and UT sensors are simultaneously embedded at various locations. An extra layer of silicon acts as a couplant to remove the air gap between the sensors and the pipe. Figure 120 shows the basic layout of the pipe wrap system.

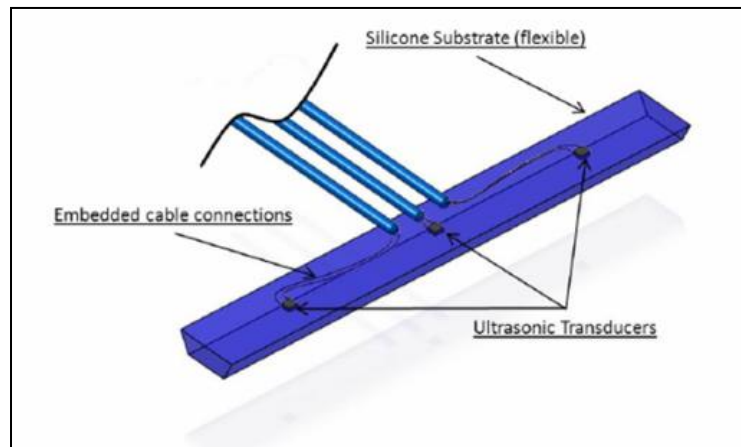


Figure 120. Typical layout of the Pipe Wrap system [1].

The Pipe Wrap™ system, although efficient, had a number of issues including: 1) excessive tightening of the pipe clamp causing damage to the UT array, 2) cabling issues, and 3) detachment due to excessive compressive force. Figure 121 shows the Pipe Wrap™ system installed on a 90° elbow of a 2" diameter pipe.



Figure 121. Installed Pipe Wrap™ system on a 2” diameter pipe [1].

Due to the limitations of the Pipe Wrap™ system, a conceptual solution has also been modeled to demonstrate possible features of a custom made alternative. A solid works drawing of the conceptual design, as shown in Figure 122, consists of a standalone framework to house the sensors. Although the concept has potential, it could be difficult to manufacture and implement.

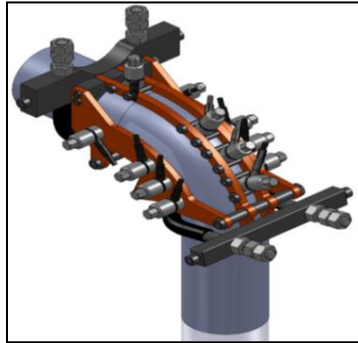


Figure 122. UT sensor system conceptual design [1].

Olympus UT Sensors

The first commercially available sensor investigated by FIU-ARC is the dual element UT sensor manufactured by Olympus 2. The model is D790 SM and includes a 45MG digital ultrasonic thickness gage. The system comes with a gel couplant (glycerin), has a frequency of 5MHz and is a dual crystal transducer with a tip diameter of 0.434”. FIU acquired the Olympus system and took some preliminary measurements on carbon steel elbows as shown in Figure 123 (a).



Figure 123. (a) Measurements using the Olympus UT system and (b) Vacuum tests.

Some of the advantages of the Olympus UT system include: 1) portable and easy to use (digital display of thickness), 2) provides accurate readings (accuracy of 0.001”), and 3) suitable for high temperatures. The system does, however, require a gel couplant and is quite large for 2” diameter pipes.

Initial bench-scale tests were conducted using the D790 SM system with the gel couplant and a dry elastomer couplant. Vacuum tests (Figure 123 (b)) were also conducted to determine if the system could be used without any couplant. The gel couplant provided accurate readings while the vacuum tests and the dry couplant were very inconsistent.

Current Efforts

Limitations in the previous year’s efforts have led to the current efforts this year, which focused on the evaluation of alternative UT systems for pipe wall thickness measurements that are commercially available. These systems are detailed in the following sections.

Accellent Smart Sensors

The Accellent smart layer sensor system [3] consists of mini piezo sensors embedded in a flexible Kapton tape. The circuits are embedded inside the tape and are available in single and multiple piezo options. The smart layer system is an integrated system which can be permanently mounted to the pipe and the readings/data can be recorded on a computer. A layout of the configuration for individual sensors is given in Figure 124. The figure also explains the features of each of the components.

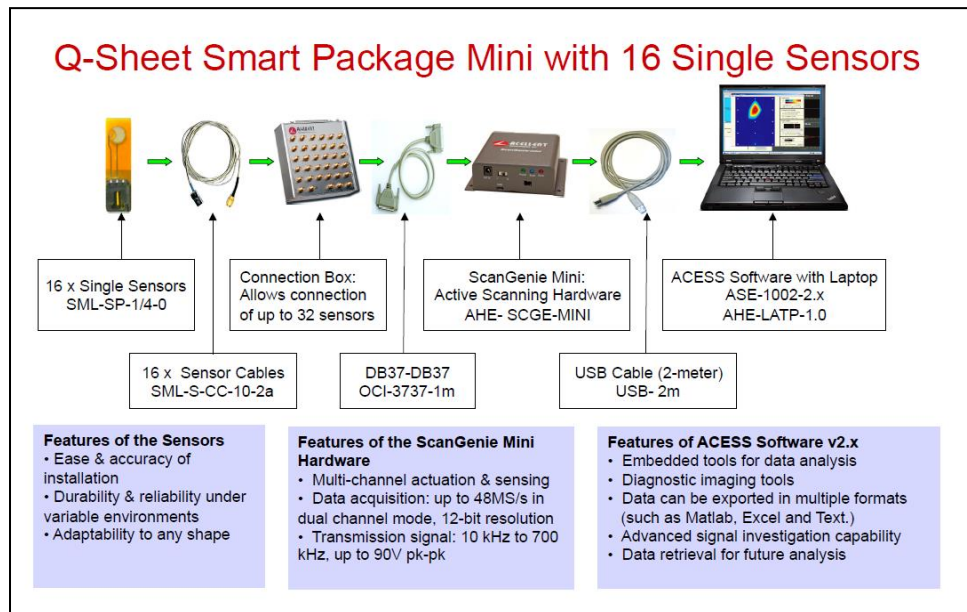


Figure 124. Accellent Smart sensor UT system 3.

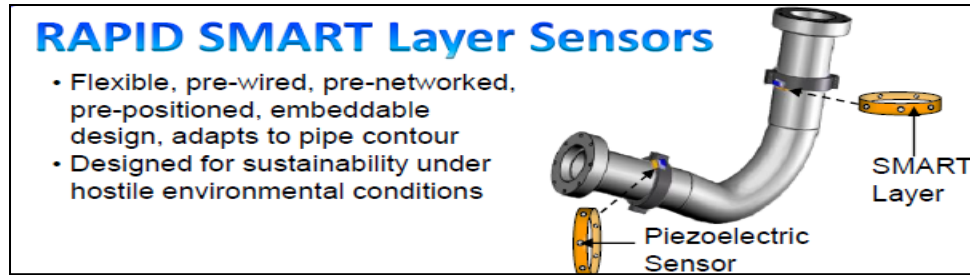


Figure 125. Smart Layer attached to a pipe 3.

The individual sensors can be integrated and embedded in a single layer called a smart layer strip which can be used in the pipeline (straight or elbow sections) as shown in Figure 125. One end of the sensor has a connector to attach it to an oscilloscope or signal generator. Initial oscilloscope tests were conducted using the single sensor. Although the smart layer technology “as-is” is a viable solution for the present task, certain limitations should be considered. The piezo-sensors (in the smart layer) are capable of providing the irregularities in the pipe line (i.e., the location and radius of a hole or anomaly due to pitting corrosion). An issue with these smart sensors is that the Smart layer is glued to the pipes using an aerospace grade epoxy. The elevated temperature and radiation levels could present problems for the adhesive.

A couple of Acellent smart sensors were procured by FIU and baseline experiments have been conducted using oscilloscopes and function generators. The sensor as shown in Figure 126 (a) consists of a single piezo-element and circuit embedded in the Kapton tape. On one end, it has a connector to connect a sensor cable for capturing the signal. Initial oscilloscope tests were conducted using the single sensor to ensure that the sensors were functioning. The setup is as shown in Figure 126 (b). The sensor was manually vibrated to see if the signal was being captured by the oscilloscope. Based on the experiments, it was concluded that the smart sensor was able to transmit the signals.



Figure 126. (a) Smart sensor placed on a pipe and (b) Oscilloscope tests using the smart sensor.

Efforts were also focused on performing time and frequency domain analysis for the smart sensors. The Acellent smart layer single sensor was used to conduct simple thickness measurements. An experimental set up to record pulse-echo sound waves from the smart sensor as shown in Figure 126 (b). Input was provided using a function generator, which was used to generate pulses to be transmitted into the pipe through the sensor. Burst mode operation was used to generate pulses since a default pulser-receiver system was unavailable. An echo sent

back by the sensor was captured by the oscilloscope (Tektronics THS 720A) as an output. A Fast Fourier Transforms (FFT) spectrum was obtained. By picking up the changes in electrical signal over time, the oscilloscope was able to continuously graph the echoes that were sent back by the UT sensor.

In order to calculate the thickness of the pipe wall, the time period of oscillations was recorded. The velocity of sound in the carbon steel test piece was obtained from literature, 5920 m/s. The distance traveled is simply determined by multiplying the velocity of sound in the pipe by the time of travel. Certain anomalies, however, were observed while recording the oscillograms (time-amplitude graphs). These could be due to the need for customized data acquisition systems for the sensors which are expensive. Further, the sensors were not radiation hardened and hence other options were investigated.

Innerspec EMAT

Electromagnetic Acoustic Transducers (EMATs) are available from Innerspec technologies [4] and are typically used on larger (> 8 inch) diameter pipes. Advantages of these systems include: 1) no couplant required, 2) can be customized for smaller diameter pipes, and 3) suitable for high temperatures. The EMAT Temate band includes an inbuilt mounting system for the pipes. The EMAT system is shown in Figure 127 and consists of the band in which sensors are embedded, a junction box and a power box. Although there are some advantages to EMAT sensors, they can only be used on carbon steel pipes. Additionally, the thickness measurements obtained are not as accurate as those obtained with UTs.



Figure 127. EMAT Temate band [4].

Ultran Couplant Free Sensors

These are metallic UT sensors similar to the traditional sensors but require no couplant. It is a dry contact sensor developed by Ultran Group [5] and works by applying a suitable torque to the sensor when mounting. It comes with a polystyrene base and is available in 2MHz and 5MHz frequencies. The typical Ultran sensors are shown in Figure 128 (a). The mini sensors (WD 25-2) have a 6.4 mm active diameter and up to 8 sensors can be mounted on a 2" diameter pipe. These are also suitable for high temperatures.



Figure 128. (a) Ultrason couplant free contact sensors [5] and (b) Experimental set up.

The WD-25 series Ultrason sensors were acquired by FIU and baseline experiments were conducted. Time and frequency domain tests were conducted on the couplant free ultrasonic transducers from Ultrason Group [5] and the thicknesses of a carbon steel pipe were obtained. The bench scale test set up is as shown in Figure 128 (b) which consists of an oscilloscope (Tektronics TDS3034) [6], a signal generator (BK precision 4040) [7] and the sensors placed on the test piece (carbon steel pipe). The UT sensors have a right angle connector for RG174/U 2M cable.

Initial tests included testing of the signal passage through the sensors. One of the sensors was excited (frequency-20kHz) using the signal generator and the other sensor was placed in contact with the first sensor as shown in Figure 129 (a). Both sensors were connected to the oscilloscopes to measure the excitation and the received signals. As expected, it is observed that both the signals overlapped indicating that bulk waves are produced by the sensor (Figure 129 b)).

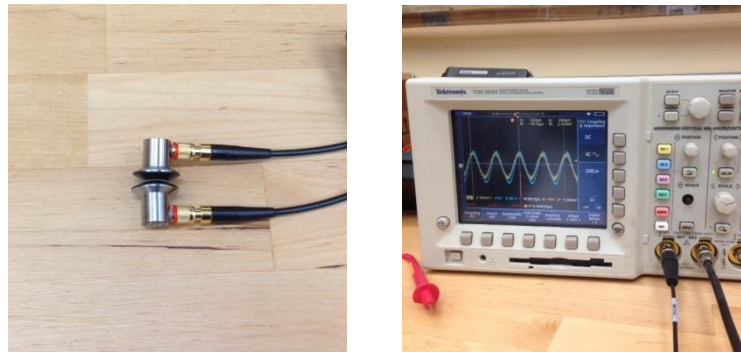


Figure 129. (a) Sensors in contact and (b) oscillogram.

The next test was to determine the time of flight of the signal to calculate the thickness of the pipe. Both sensors were placed next to each other. One was used to send the sound waves into the pipe (pulse) and the other was used to capture the reflected wave (echo). The arrangement is as shown in Figure 130 (a). From the oscillogram in Figure 130 (b), the lag time for the waves was found to be $1.2 \mu\text{s}$. Using this information and the velocity of sound in the material (carbon steel – $0.231 \text{ in}/\mu\text{s}$), the thickness of the pipe was found to be approximately 0.15 in.



Figure 130. (a) Adjacent sensors and (b) oscillogram.

Permasense Guided Wave Sensors

This system is developed by a UK based manufacturer, Permasense [8], and is as shown in Figure 131 (a). The Permasense UT system is an integrated wireless system (Figure 131 (b)) and uses a novel guided wave technology for acoustic wave propagation. This UT sensor system does provide actual thickness measurements in pipes and can be used on 2-inch pipes and elbows. It can also be customized for mounting with a mechanical clamping system (Figure 131 (c)). The limitations include an expensive data acquisition system and only 2 sensors can be installed on the circumference of a 2-inch diameter pipe. This is to avoid cross-talk between the sensors in the limited space.

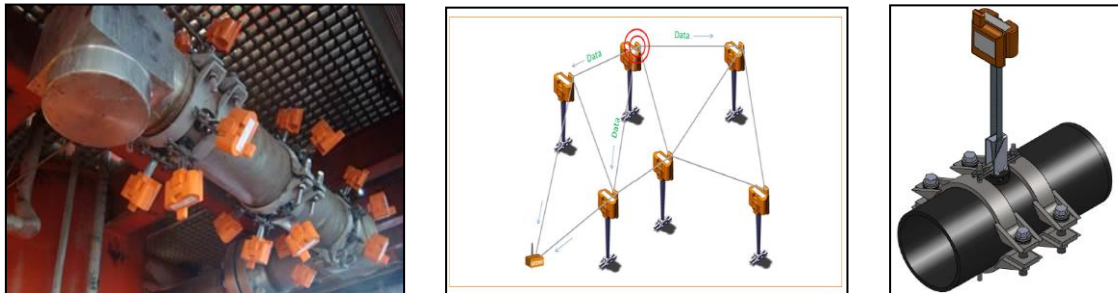


Figure 131. (a) UT sensors, (b) Wireless network, and (c) Mounting system [8].

These sensors have proven applications in oil and gas industries and similar areas. As a recent example, erosion/corrosion monitoring using the permanent mount Permasense system in European refineries has been successfully implemented [9]. Thinning of pipes was determined based on real-time continuous monitoring.

The sensors are capable of operating up to 600°C (1100°F). This is due to their patented waveguide technology that holds the sensor head (with ultrasonic transducers, electronics, and battery) away from the hot metal. The sensor's measurements are transmitted wirelessly back to a gateway (wireless access point) mounted near the main unit. A system schematic is shown in Figure 132(a).

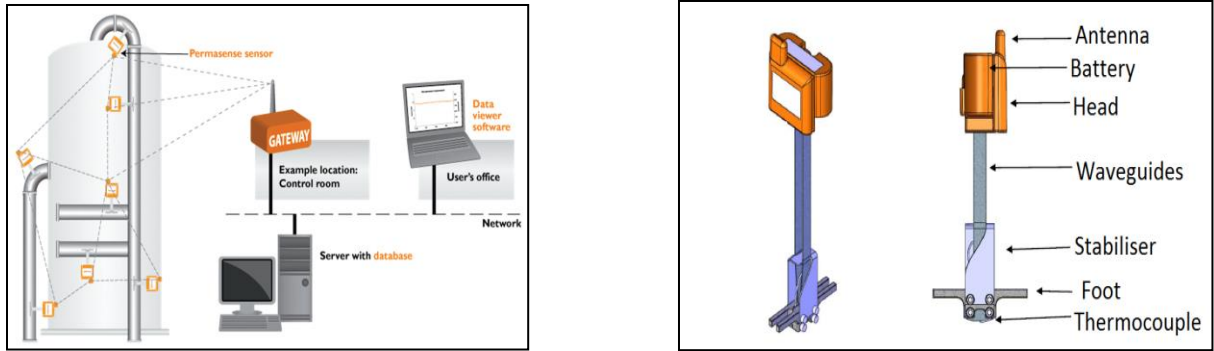


Figure 132. (a) Permasense corrosion monitoring system 9 and (b) Permasense WT 210 series UT sensor [8].

Since there is no cost associated with measurement acquisition or measurement retrieval, the frequency of measurement can be configured to be as frequent as every 15 minutes. Connection of the gateway to the operator's existing information technology infrastructure allows the data to be viewed from personnel desks. Sensor battery life of up to 10 years allows continuous data delivery between turnarounds without access to a sensor's physical location.

The WT-210 series sensor is as shown in Figure 132 (b). It consists of the 304 stainless steel wave guides, sensor head, antenna, battery and a stabilizer. In addition there is a built in thermocouple probe to monitor the pipe surface temperature which also allows the wall thickness measurement to be temperature compensated when required. The sensors communicate using the wirelessHART protocol, creating a self-forming and self-managing wireless mesh, which delivers continuous wall thickness measurements of the highest integrity and accuracy directly to the end user.

Based on the discussions with WRPS, the down selection of the UT sensors from all the investigated options was conducted. It was decided that the two viable options to be pursued are the Permasense guided wave sensors and the Ultran dry couplant sensors.

CONCLUSIONS

Each of the UT sensor systems mentioned in the previous section have certain advantages and limitations. Based on discussions with the site engineers, two of the options have been down selected for further investigation. These include the Permasense guided wave technology and the Ultrason couplant free sensors. Selections were based on applicability to various pipe sizes, ability to determine thicknesses accurately, and cost. One of the major challenges associated with a custom built remote permanently mounted UT system for pipe wall thickness measurements is the pricing of the systems.

Recently, FIU has acquired the Permasense sensors and is pursuing cost effective leasing options for the Ultrason sensor systems.

Future work will include: the validations of the sensors for accurate readings, installation on a custom built pipe layout and potential integration of the sensors with the inspection tools being developed at FIU-ARC. The pipe layout for installation and testing of the sensors will be designed and fabricated at FIU using 2-, 3- and 4-inch pipe sections, elbows and reducers to replicate typical waste transfer system pipe fittings.

In addition, the sensors will also be tested on a full-scale sectional mock-up of the DST's being assembled at FIU and further combined with the robotic inspection tools (peristaltic crawler and the mini-rover).

REFERENCES

1. B. J. Vasquez, RPP – RPT – 55812, Engineering Evaluation of Remote Permanently Mounted Pipe Wall Ultrasonic Thickness Measurement Devices, Rev 0, Washington River Protection Solutions, Richland, WA.
2. www.olympus-ims.com
3. <http://www.acellent.com>
4. <http://innerspec.com/applications/integrated-systems/monitoring-systems/corrosion-monitoring>
5. <http://www.ultrangroup.com/index.php/products/transducers/standard/dry-coupling-direct-contact/>
6. <http://www.tek.com/oscilloscope/tds3014b-manual/tds3000-tds3000b-tds3000c-series>
7. <http://people.ece.cornell.edu/land/courses/ece4760/equipment/BK4040a.pdf>
8. <http://www.permasense.com>
9. Philip T. and Jake D., “Monitoring and simulation resolves overhead corrosion – online corrosion monitoring in tandem with simulation modelling identified the root cause of corrosion in a crude unit overhead”, www.eptq.com – PTQ Q1 2016.

TASK 19.2

EVALUATION OF NONMETALLIC COMPONENTS IN THE WASTE TRANSFER SYSTEM (FIU YEAR 6)

EXECUTIVE SUMMARY

Nonmetallic materials are used in the United States Department of Energy's Hanford Site Tank Farm waste transfer system. These materials include the inner primary hoses in the hose-in-hose transfer lines (HIHTLs), Garlock[®] gaskets, ethylene propylene diene monomer (EPDM) O-rings, and other nonmetallic materials. These nonmetallic materials are exposed to β and γ irradiation, caustic solutions as well as high temperatures and pressure stressors. How the nonmetallic components react to each of these stressors individually has been well established. However, simultaneous exposure of these stressors has not been evaluated and is of great concern to Hanford Site engineers.

FIU engineers have worked closely with key Hanford HLW personnel to develop an experimental test plan to determine how these nonmetallic components react to various simultaneous stressor exposures. More specifically, the initial phase of testing includes exposure of Garlock[®] and EPDM components to caustic material at various temperatures for varying lengths of exposure time. After the tests have been conducted and the data analyzed, additional testing phases will be conducted that may include the effects of elevated pressure and the use of different materials (Teflon and Tefzel).

The materials being tested consist of EPDM and Garlock[®] coupons, EPDM HIHTL inner hoses and EPDM O-rings as well as Garlock[®] gaskets. Coupons are being used to obtain a fundamental understanding of the relationship of the stressor with the various materials. Components (inner hoses, O-rings and gaskets) will be used to determine the effect on the component being evaluated in an environment similar to its operational environment. An experimental test loop has been constructed and aging of the components and coupons has commenced. The system can accommodate eighteen component assemblies. Each assembly consists of one EPDM HIHTL, one EPDM O-ring and one Garlock[®] gasket. There are three assembly aging sets, one for each temperature. Each set has six assemblies in it; three for each of the two time periods.

Prior to aging of the components, a sample set was mechanically tested to obtain various baseline properties as per ASTM standards. The aging of the materials involves exposing each sample to a 25% NaOH solution at ambient (100°F), operating (130°F) and design temperatures (175°F) for durations of 180 and 365 days. After aging/conditioning, the mechanical and material properties of the aged samples will be measured and compared with the baseline results to obtain an understanding of degradation caused by the stressors.

INTRODUCTION

Nonmetallic materials are utilized in the waste transfer system at the Hanford tank farms; these include the inner hose of the hose-in-hose transfer lines (HIHTLs), Garlock[®] gaskets and ethylene propylene diene monomer (EPDM) O-rings. These materials are exposed to simultaneous stressors including β and γ radiation, elevated temperatures, caustic supernatant as well as high pressures during normal use. In 2011, the Defense Nuclear Facilities Safety Board recommended to the U.S. Department of Energy (DOE) to conduct post service examination of HIHTLs and Teflon gaskets to improve the existing technical basis for component service life. Suppliers of the nonmetallic components often provide information regarding the effects of some of the stressors, but information is not provided for simultaneous exposure. An extensive test plan was developed by Sandia National Laboratories to understand the simultaneous effects of the aforementioned stressors [1]; however, this test plan was never executed. Additional studies conducted by Lieberman provides information on HIHTLs at elevated temperature and pressure but little information is gained regarding the synergistic effects with the caustic supernatant [2]. Florida International University (FIU) has been tasked with supporting this effort by conducting multi stressor testing on typical nonmetallic materials used at the Hanford tank farms.

This report provides results from the initial mechanical property testing of EPDM and Garlock[®] material coupons as well as the initial blowout/leak testing for HIHTL, EPDM O-rings and Garlock[®] gaskets. In addition, the experimental test loop being used to age the test specimens is described.

EXPERIMENTAL TESTING

All material samples had their baseline mechanical performance and properties tested as per ASTM standards prior to any exposure. Once the baseline properties have been determined, each material sample will be aged, which will involve exposing each sample to a chemical simulant at ambient (100°F), operating (130°F) and design temperatures (175°F) for duration of 180 and 365 days. Tests were conducted on both material coupons as well as in-service configuration assemblies. After aging/conditioning, the mechanical properties of the samples will again be measured as per ASTM standards.

Baseline Material Testing

Baseline Coupon Hardness Testing

To assess the baseline material properties of EPDM and Garlock[®], sheets of the material were obtained and coupon specimens (Figure 133) were cut using a D412-C die. The specimens were used to determine hardness values obtained using a LECO LMV 50 Series hardness tester. To determine the material hardness, a load of 500 grams was used to create an indentation in the sample and hardness values according to the Rockwell scale and Vickers scale were obtained. Multiple measurements were taken from 3 different Garlock[®] specimens. These results and the corresponding averages are provided in Table 10. Since EPDM material is a soft material, hardness readings were unable to be obtained with existing equipment.



Figure 133. Coupon dumbbells.

Table 10. Baseline Coupon Hardness Test Results - Garlock® Data

Vickers	Rockwell HRB/HRC
4	54
3	54
4	54
4	54
4	54
4	54
4	54
4	54
4	54
4	54
5	54.1
5	54.1
AVERAGE VALUES	
4.09	54.02

Baseline Coupon Tensile Testing

Baseline coupon tensile testing was conducted for both un-aged EPDM coupons and un-aged Garlock coupons. All procedures used for testing were derived from the ASTM standards and were recorded to provide consistency throughout all tensile testing experiments, for both EPDM and Garlock® material coupons. Figure 134 shows the un-aged EPDM coupon in the tensile testing machine before testing (left) and before rupture (right).

**Figure 134. EPDM coupon testing.**

Sample experimental data received from the un-aged EPDM coupons is shown below. The graph shows a force load curve representing the magnitude of the load versus the extension of the material.

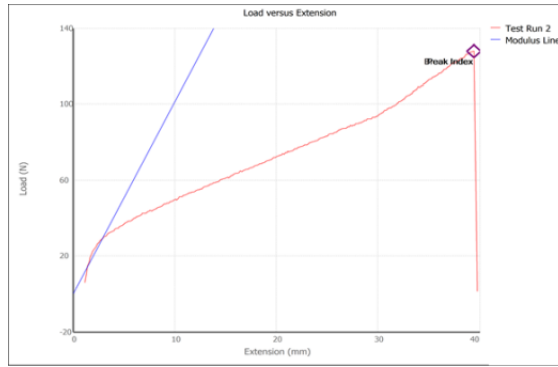


Figure 135. Load vs extension for EPDM.

Table 11 shows the average test results for peak stress, peak load, strain at break and modulus of elasticity for the un-aged EPDM coupons.

Table 11. Average Test Results from EPDM

Average Test Run Results - EPDM		
Display Name	Value	Unit
Peak Stress	0.002	kN/mm ²
Peak Load	0.13133	kN
Strain at Break	0.76367	mm/mm
Modulus	0.00833	kN/mm ²
Width	25	mm
Thickness	2.381	mm

Figure 136 shows the un-aged Garlock[®] coupon in the tensile testing machine before testing (left) and right after rupture (right).



Figure 136. Garlock coupon testing.

Typical experimental data obtained from the un-aged Garlock[®] coupons is shown below. The average test results for the un-aged Garlock[®] coupons are provided in Table 12.

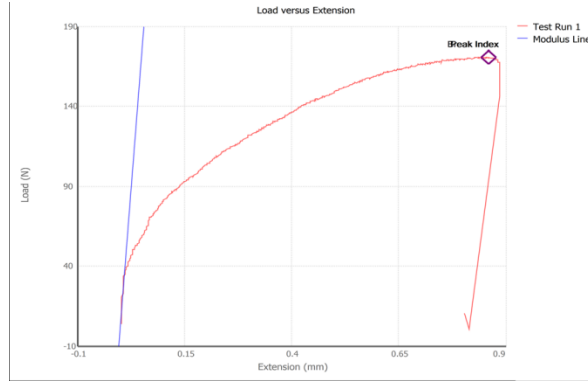


Figure 137. Load vs extension for Garlock®.

Table 12. Average Test Results from Garlok® Coupons

Average Test Run Results - Garlock		
Display Name	Value	Unit
Peak Stress	0.003	kN/mm ²
Peak Load	0.17367	kN
Strain at Break	0.0167	mm/mm
Modulus	3.03967	kN/mm ²
Width	25	mm
Thickness	2.381	mm

Baseline Pressure Testing

In order to quantify how each sample was affected by the exposure to the caustic stressor, pre-exposure mechanical testing was conducted. Mechanical testing included hose burst and O-ring/gasket leak tests as per ASTM D380-94 and ASTM F237-05, respectively. The tests were conducted on the 9 test samples (3 from each material). These results will be compared to post-exposure testing to be conducted on samples exposed 6-months and 12-months.

Baseline pressure tests were conducted on hose-in-hose transfer lines (HIHTL), ethylene propylene diene monomer (EPDM) O-rings and Garlock® gaskets. HIHTL pressure tests involved pressurizing each test section at a constant rate until the hose ruptured. Baseline hose pressure testing was conducted on three hose specimens. The results are shown in Table 13.

Table 13. Baseline HIHTL Pressure Test Results

	H-00-1	H-00-2	H-00-3	Average
Water Temperature (°F)	72.00	72.00	75.40	73.15
Ambient Temperature (°F)	67.00	66.00	81.00	75.00
Humidity %	37.00	36.00	67.00	50.00
Burst Pressure (psig)	2740.21	2925.95	2807.25	2805.33
Type of Failure	Rupture	Rupture	Rupture	N/A
Time Until Failure (s)	320.50	216.00	203.50	221.38
Start Length (in.)	29.75	30.25	30.25	30.0625
End Length (in.)	31.50	31.00	31.00	30.94
Deformation Length (in.)	1.75	0.75	0.75	0.875
Test Date	3/21/2016	3/21/2016	3/25/2016	N/A

Each specimen experienced a rupture type failure, with the average maximum pressure at 2805.33 psig. Each specimen also experienced a permanent deformation in their lengths, which averaged 0.875 inches. A photo of a typical failed hose specimen is shown in Figure 138.

**Figure 138. Ruptured HIHTL test specimen.**

The baseline O-ring pressure testing was conducted for three EPDM O-ring specimens. The test rig and the results of the testing are shown in Figure 139 and Table 14, respectively.



Figure 139. O-ring pressure test rig.

Table 14. Baseline O-ring Pressure Test Results

	O-00-1	O-00-2	O-00-3	Average
Water Temperature (°F)	73.20	77.50	76.20	75.63
Ambient Temperature (°F)	82.00	85.00	85.00	84.00
Humidity %	68.00	59.00	59.00	62.00
Holding Pressure (psig)	255.00	245.00	265.00	255.00
Pressure Maintained?	Yes	Yes	Yes	N/A
Time Until Failure (s)	N/A	N/A	N/A	N/A
Test Date	3/29/2016	3/29/2016	3/29/2016	N/A

Each specimen maintained the allotted pressure for the 5 minute time interval. The average pressure that the O-rings were maintained at was 255 psig, which was 20 psig over the original desired pressure. The change in the prescribed pressure was due to the large variations in the hand-pump.

The baseline Garlock® gasket pressure testing was conducted for three gasket specimens. The test rig and the results of the testing are shown in Figure 140 and Table 15.



Figure 140. Gasket baseline pressure test rig.

Table 15. Baseline Gasket Pressure Test Results

	G-00-1	G-00-2	G-00-3	Average
Water Temperature (°F)	75.00	75.00	75.00	75.00
Ambient Temperature (°F)	79.00	78.00	78.00	78.33
Humidity %	50.00	54.00	52.00	52.00
Holding Pressure (psig)	166.75	149.89	148.30	154.98
Pressure Maintained?	Yes	Yes	Yes	N/A
Time Until Failure (s)	N/A	N/A	N/A	N/A
Test Date	4/4/2016	4/4/2016	4/4/2016	N/A

Each specimen maintained the allotted pressure for the 5 minute time interval. The average pressure that the gaskets were held at was 154.98 psig, which was only 5 psig over the desired pressure.

Material Aging

In-Service Configuration Aging

The in-service configuration aging experimental consists of 3 independent pumping loops with two manifold sections on each loop (Figure 141). Each of the 3 loops is run at a different temperature (100°F, 130°F and 175°F). Each manifold section holds three test samples and will be used for a corresponding exposure time of 6 months and 1 year. Each test sample consists of a HIHTL hose section, an EPDM O-ring and a Garlock® gasket placed in a series configuration. Isolation valves on each manifold allow removal of samples without affecting the main loop and the rest of the samples. The temperature of the chemical solution circulating within each loop is maintained at a preset temperature by an electronically controlled heater (Figure 142). A 25% sodium hydroxide solution is used as a chemical stressor that circulates in each of the loops. The chemical stressor's pH is checked every 30 days to ensure that the concentration levels are remain constant.

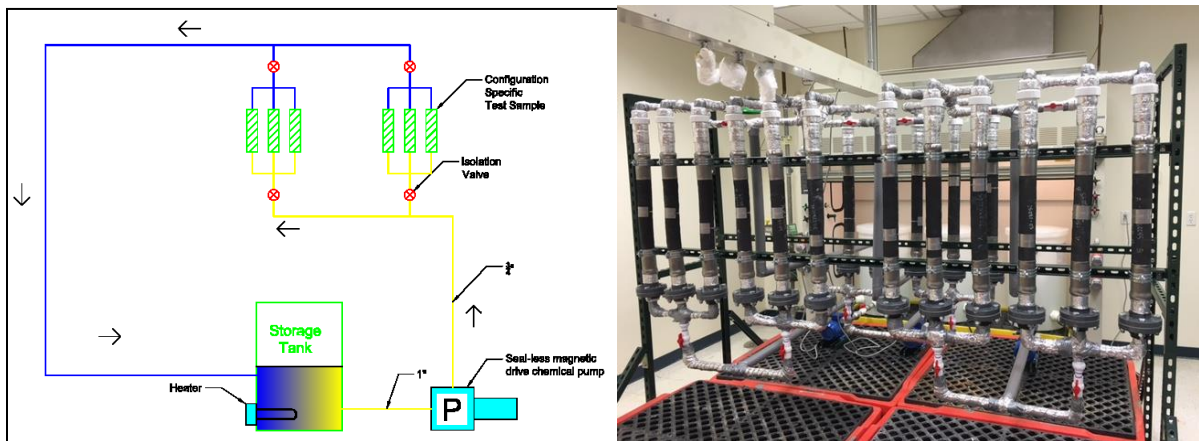


Figure 141. In-service component aging loop.



Figure 142. Thermostatically controlled tank heater.

Coupon Aging

The coupon aging experiment setup consists of one coupon aging vessel (Figure 143) submerged in each of the three test loop’s storage tanks. This will result in exposing the coupons to the same conditions as the in-service configuration tests; the circulating fluid is the same 25% sodium hydroxide solution. Each vessel contains 10 coupons (5 of each type of EPDM and Garlock® materials) and will be submerged in the bath for duration of 180 and 365 days. Table 16 shows the test coupon aging matrix.

Table 16. Coupon Aging Matrix

Days Exposure	Ambient Temperature (100°F)	Operating Temperature (130°F)	Design Temperature (180°F)	Baseline
0				10 coupon samples
180	10 coupon samples	10 coupon samples	10 coupon samples	
360	10 coupon samples	10 coupon samples	10 coupon samples	



Figure 143. Coupon Aging Vessel

CONCLUSIONS AND FUTURE WORK

After analyzing the experimental data from the baseline material testing, FIU engineers discussed their findings with the Hanford engineers and found out that their results were similar to the data obtained by the Hanford engineers during previous experiments. Aging of the specimens commenced at the beginning of June and is scheduled to continue for durations of six months and one year. After the tests have been conducted and the data analyzed, additional testing phases may be considered. This may include the effects of elevated pressure in addition to elevated temperature and exposure to caustic solutions. Additional material may also be evaluated including the use Teflon and Tefzel.

REFERENCES

1. H Brush, C. O. (2013). Test Plan for the Irradiation of Nonmetallic Materials. Albuquerque, New Mexico: Sandia National Laboratories.
2. Lieberman, P. (2004). Banded (Band-It) and Swaged Hose-In-Hose (HIHTL) Assembly Service Life Verification Program. Santa Clarita, California: National Technical Systems.

APPENDICES

The following reports are available at the DOE Research website for the Cooperative Agreement between the U.S. Department of Energy Office of Environmental Management and the Applied Research Center at Florida International University: <http://doeresearch.fiu.edu>

1. Florida International University, *Project Technical Plan*, Project 1: Chemical Process Alternatives for Radioactive Waste, October 2015.
2. Florida International University, *Inside Wall Temperature Measurements of DSTs using an Infrared Temperature Sensor*, Test Plan, December 2015.
3. Florida International University, *Experimental Test Plan to Assess the Utility of 3D Sonars for Monitoring High-Level Radioactive Waste Settled Solids Surfaces for Indicators of Developing Deep Sludge Gas Release Events*, January 2016.
4. Florida International University, *Development of Inspection Tools for DST Primary Tanks: Pneumatic Pipe Crawler*, February 2016.
5. Florida International University, *Investigation into Ultrasonic Transducer Systems for Wall Thickness Measurements*, March 2016.
6. Florida International University, *Baseline Testing Results of Nonmetallic Materials in Hanford's HLW Transfer System*, April 2016.
7. Florida International University, *Poreh's Radial Jet Correlations as Applied to a Pulse Jet Mixing Process*, May 2016.
8. Florida International University, *Determine the Inside Wall Temperature of DSTs using an Infrared Sensor*, Summary Document, July 2016.